Studies on processing additives introduced to increase the efficiency of organic solar cells: selection and mechanistic effects

by

Uyxing VONGSAYSY

A thesis
presented to the University of Waterloo
in fulfillment of the
thesis requirement for the degree of
Doctor of Philosophy

in

Electrical Computer Engineering

Waterloo, Ontario, Canada, 2015

Declaration of Authorship

'I hereby declare that I am the sole author of this thesis. This is a true copy of the thesis, including any required final revisions, as accepted by my examiners.
I understand that my thesis may be made electronically available to the public.'

Abstract

Polymeric bulk heterojunction (BHJ) organic solar cells (OSCs) have attracted significant interest as a low cost and renewable technology to harvest solar energy. Despite these advantages, their generally low power conversion efficiencies are a barrier for their movement into commercial applications. Controlling the BHJ morphology is a key step in the pursuit of higher OSC efficiencies.

Processing additives have emerged as effective components for controlling and optimizing the BHJ morphology. Despite their widespread use, their mechanistic roles are not yet fully understood, thus appropriate selection remains the result of trial and error experiments. This thesis provides a comprehensive study on the introduction of processing additives in OSC formulation. The semiconductor system under study is based on poly(3-hexylthiophene) (P3HT) and [6,6]-phenyl-C61-butyric acid methyl ester ($PC_{61}BM$).

First, a systematic method was developed to guide the selection of processing additives from a large range of solvents. This method employs the Hansen solubility parameters to define a set of numerical criteria based on the solubility properties of the semiconductors. The method was successfully applied to the P3HT/$PC_{61}BM$-system and resulted in the identification of three new efficient processing additives.

Next, the mechanistic role of additives in influencing the BHJ morphology is investigated by performing structural, electrical and optical characterizations. The results suggested that processing additives lead to the formation of a BHJ with more numerous but smaller polymer crystallites. Also, the effects of additive on OSC performance differed depending on whether the OSC was fabricated in an inverted or in a conventional architecture. Such differences can be explained in terms of variations in electron and hole mobilities caused by the additive.

Furthermore, photo-stability tests, performed on different types of OSCs, showed that processing additives can improve the photo-stability. The results showed that improvement was related to the formation of a more photo-stable interface with the top electrode.

Finally, the scope of this study is extended to two other donor polymers. The effects of processing additives differed from those seen in the P3HT/$PC_{61}BM$-system because of the different properties of these polymers.

Acknowledgements

At the end of my engineering school, I had the opportunity to perform this PhD in the field of organic photovoltaics as part of an international program between Canada and France. Back then, I was very excited because I pictured this as a major opportunity in my professional and personal life. Professional, because I was passionate about organic electronics and this PhD was the opportunity to strengthen my knowledge and to contribute scientifically to this innovative field. Personal, because the development of renewable energy is of major importance to me and I was also looking forward to live and work in Canada. Four years later, I am glad to observe that my expectations have been successfully fulfilled and that I gained valuable experiences that were beyond my expectations. I grew up and I learn a lot. This would not have been possible without the large body of people I was lucky and honored to work with and to be friend with. These are the people I want to thank here.

First of all, I would like to thank all my supervisors for giving me the great opportunity to perform this PhD and for their guidance throughout these years. I am highly grateful to **Bertrand Pavageau** for giving me the opportunity to perform this PhD at LOF and for his constant support and his never fading enthusiasm towards my research and my ideas. I would like to address my sincere gratitude to **Pr. Laurent Servant** for his contribution and his advice in my research but also when I had administrative issues. His availability and his concern for my PhD helped me to carry out my research in good conditions. I am truly grateful to **Pr. Hany Aziz** for welcoming me in his group. His guidance and his trust in me pushed me to take risks and to do my best. Particularly, during the writing of my thesis, his patience and his advices highly contributed to its quality. To him, I want to express my respect and my sincere gratitude. Sincere thanks go to **Dr. Dario Bassani** for his support and for fruitful discussions about my research and my manuscripts.

I would like to address my sincere gratitude to **Dr. Guillaume Wantz** and **Dr. Lionel Hirsch** for welcoming me in the Laboratoire d'intégration du matériau aux systèmes (IMS) which is a scientifically great and friendly environment. Special thanks to Guillaume for the discussions; for valuing my work and for always pushing me to be more ambitious.

I would like to address my sincere thanks to **Pr. Thomas Heiser** from the University of Strasbourg, **Pr. Alejandro Briseno** from the University of Massachusetts and **Pr.**

Siva Sivoththaman from the University of Waterloo for accepting to be part of my committee, for reviewing my thesis and for providing valuable comments.

I would like to acknowledge **Solvay**, the **Natural Sciences and Engineering Research Council of Canada** as well as the **Waterloo Institute for Nanotechnology** for funding my PhD research.

As my thesis was performed in a co-tutelle program, I had the pleasure of being part of four different laboratories. In France, I started my work at LOF Solvay. I thank the director at the time, **Patrick Maestro** for welcoming me at LOF. I thank **Simon Rousseau** and **Samantha Armisen** for sharing their valuable expertise and for their help in the determination of the Hansen Solubility Parameters. I would like to thank all the LOF team for welcoming me and more particularly few buddies for their supports and their friendships: **Vincent Mansard** (now lost somewhere in the west coast), **Julie Angly** (for her enthusiasm, her optimism and for the tea), **Cyril Vidaillac** (for all the valuable conversations), **Hongyu** (for always being smiley, strong and therefore inspiring), **Julien Jolly**, **Ana Maldonado**, **Marta Romano**, **Rawad Tadmouri** and many more.

In France, I worked in parallel in the Institut des Sciences Moléculaires (ISM). In the group of Nano-structures Organiques, I thank **Dr. Debdas Ray** and **Dr. Chih-Kai Liang** who helped with the synthesis of $PC_{61}BM$. In the group of Spectroscopie Moléculaire, I thank **Colette Belin** for helping me with the AFM imaging, **Thierry Buffeteau** and **Gwenaelle Lebourdon** for their valuable help in the PM-IRRAS experiments on active layer thin films.

Still in France, I had the chance to be part of IMS. I would like to thank **Dr. Mamatimin Abbas** for fruitful discussions and for helping me with transistor fabrication and measurement (despite my stubbornness). I also thank **Dr. Sylvain Chambon** for always being available for scientific discussions. I truly appreciated his help and his interest in my research. I also want to thank all the members or ELORGA: **Pr. Laurence Vignau** (for being the first one to trigger my interest in organic electronic), **Pr. Pascal Tardy** and all the students who brought a enjoyable atmosphere in the lab: **Dargie Daribew** (my friend), **Elodie Destouesse** (for her great help when I first arrived in IMS), **Maxime Lebail**, **Lionel Derue**, **Frédéric Guillain**, **Gildas Laurans** (pour les caramels au beurre salé et ta bonne humeur au bad entre autres), **Léo Peres** (malgré tes blagues malheureusement sans fin, merci pour ton soutien), **Yolande Murat** (la plus gentille en 2015 j'espère), **Geoffroy Houin** (mon

grand), **William Greenbank**, **Marcin**, **Damien Thuau**, **Pierre Henrie**, **Thérèse Gorisse**, **Georgio Mattana**, **Yu-Tang Tsai** and **Yan-Fang Chen**.

In Canada, I was part of the Nanotechnology program of the University of Waterloo in the group of Pr. Hany Aziz. I would like to thank the technical lab managers of the Giga-to-Nanoelectronics lab **Richard Barber** and **Robert Mullins** for their role in providing to the students the best working conditions. I would like to address special thanks to **Graeme Williams** for fruitful discussions and his great help throughout my PhD especially when I first arrived in UW and to **Qi Wang** for helping me with the adhesion measurements and to achieve a running pace of 5 min/km. Thank you to all the other group members: **Afshin Zamani** (my coffee buddy), **Mike Zhang**, **Sibi Sutty**, **Yoshitaka Kajiyama**, **Anne Bouchauty**, **Tyler**, **Thomas**, **Baolin**. They were all unique and inspiring to me in their own way.

This PhD project was part of the IDS funmat program. As part of this program, I had the occasions to meet and to discuss with people from a large variety of scientific and cultural backgrounds. It was enriching and fun, thank you guys and especially: **Alex Cunha**, **Marie Asano**, **Edgar Cao** (we are finally in the same city!), **Mathilde Champeau**, **Camillle Legros** and **An Teaspoon** (crazy food and squash buddies) and **Annie Cheng** (thank you for supporting me through the multiple periods of craziness), **Nathacha Kinadjian**, **Dan** (for all the unforgettable cookies), **Erin** (thank you so much for all the editing, for initiating my passion for yoga and running and for the great time), **Medhi**, **Nhi**, **Jiang** (my bored enemy) and **Mylène** (finalement je t'ai mise là, merci pour tout le fun et pour ton support! Je crois en toi pour la suite) and many many more.

Last but not least, I would like to thank all my family and Wi for the unconditional support that helped me throughout this journey.

Thank you all so much.

Contents

List of Figures

List of Tables

Abbreviations

A	Acceptor
AFM	Atomic Force Microscopy
AM 1.5	Air Mass 1.5
ATR	Atenuated Total Reflection
BHJ	Bulk Heterojunction
C_{60}	Buckminster fullerene
CB	Chlorobenzene
C-PYR	1-cyclohexyl-2-pyrrolidinone
D	Donor
DDP	1,4-diketopyrrolo[3,4-c]pyrrole
DEGDE	di(ethylene glycol)-diethyl ether
DPH	Dimethyl Phthalate
DPPBT	Poly(diketopyrrolopyrrole-quaterthiophene
DPPT	Poly(diketopyrrolopyrrole-terthiophene)
ETL	Electron Transport Layer
FF	Fill Factor
FWHM	Full Width at Half Maximum
GIXD	Grazing Incidence X-ray Diffraction
I_{DS}	Drain source current
HOMO	Highest Occupied Molecular Orbital
HSP	Hansen Solubility Parameters
HTL	Hole Transport Layer
ICBA	Indene-C_{60} bisadduct

$IV_{70}BA$	Indene-C_{70} bisadduct
ITO	Indium Tin Oxide
J	Current density
J-V	Current density - Voltage
J_{sc}	Short-Circuit current density
LUMO	Lowest Unoccupied Molecular Orbital
MoO_3	Molybdenum oxide
NMP	n-methyl-2-pyrrolidinone
ODCB	O-Dichlorobenzene
ODT	1,8-octanedithiol
OSC	Organic Solar Cell
OTFT	Organic Thin Film Transistor
P3HT	Poly-3-hexylthiophene
$PC_{61}BM$	[6,6]-phenyl-C60-butyric acid methyl ester
PCDTBT	Poly[N-9'-heptadecanyl-2,7-carbazole-alt-5,5-(4',7'-di-2-thienyl-2',1',3'-ben--zothiadiazole)]
PCPDTBT	Poly[2,1,3-benzothiadiazole-4,7-diyl[4,4-bis(2-ethyl-hexyl)-4H-cyclopenta[2,1--b:3,4-b0]dithiophene-2,6-diyl]]
PCE	Power Conversion Efficiency
PDQT	Diketopyrrolopyrrole (DPP) with β- unsubstituted quaterthiophene (QT)
PDTSTPD	Poly(4,4'-bis(2-ethylhexyl)-dithieno[3,2-b:2',3'-d]silole)-2,6-diyl-alt-((5-octyl--thieno[3,4-c]pyrrole-4,6-}dione)-1,3-diyl)]
Pedot-PSS	Poly(3,4-ethylenedioxythiophene):poly(styrenesulfonic acid)
PM-IRRAS	Polarization Modulated-Infra Red Reflection Absorption Spectroscopy
PTB7	Poly[[4,8-bis[(2-ethylhexyl)oxy]benzo[1,2-b:4,5-b9]dithiophene-2,6-diyl]
PVT	Poly(1-vinyl-1,2,4-triazole)
RED	Relative Energy Difference
R_{sh}	Shunt Resistance
R_s	Series Resistance
SCLC	Space Charge Limited Current
TRIB	Tributyl *o*-acetylcitrate

UV-Vis	UltraViolet-Visible
V_{DS}	Drain source voltage
V_{GS}	Gate source voltage
V_{oc}	Open Circuit Voltage
V_{th}	Threshold Voltage
XRD	X-Ray Diffraction
ZnO	Zinc Oxide

Symbols

δ	Solubility parameter [$MPa^{1/2}$]
eV	Electron Volt
μ	Mobility [$cm^2.V^{-1}.s^{-1}$]
Ω	Resistance [Ohm]

Chapter 1

Introduction to organic solar cells

1.1 General introduction

The industrial revolution represented a serious transition in humanity's standard of life leading to significant advances that contributed to higher life expectancy, quality of life and comfort. These developments, along with a growing population, caused exponential growth in energy demand over the past years.

To date, energy demand has mostly been met by burning fossil fuels (oil, gas and coal). However, such processes are not environmentally sustainable due to the emission of green house gases in Earth's atmosphere, contributing to global warming. Additionally, as fossil fuel is a non-infinite source of energy, the resource depletion causes serious societal and political issues. Alternatives must be developed to satisfy the energy demand in a sustainable way.

In this context, solar energy offers many advantages as a renewable source of energy. One of them is the large amount of energy provided by solar irradiation on Earth: estimations - considering realistic irradiated surface and conversion yield - showed that solar energy could provide up to two times the world's energy demand [54]. Additionally, the worldwide availability of solar energy could benefit remote regions of the world by means of decentralized production of energy.

Solar radiation is converted into electricity by means of photovoltaic cells, also called solar cells. They have been fabricated from a wide range of materials as shown in the National Renewable Energy Laboratory chart (Figure 1.1). To date, the most prevalent types of photovoltaic panels use crystalline silicon in the monocrystalline or polycrystalline form. At the laboratory scale, conversion efficiencies reach 25% [64], while in commercial products, the efficiencies tend to be around 20% [103]. Crystalline silicon solar cells dominate in terms of efficiency, but suffer from high fabrication costs and restrictive mechanical and physical properties, such as weight and fragility. Therefore, they have not been able to fully compete with fossil fuels. In the pursuit of further lowering module cost and encouraging wide-spread application, other technologies were developed. Thin film technologies (indicated by data in green in Figure 1.1) are a good alternative as they require less material and lower fabrication costs. Organic photovoltaics (depicted in red in Figure 1.1) are also an interesting and exciting route for the prospect of extremely low cost solar panels with additional features such as low weight and flexibility.

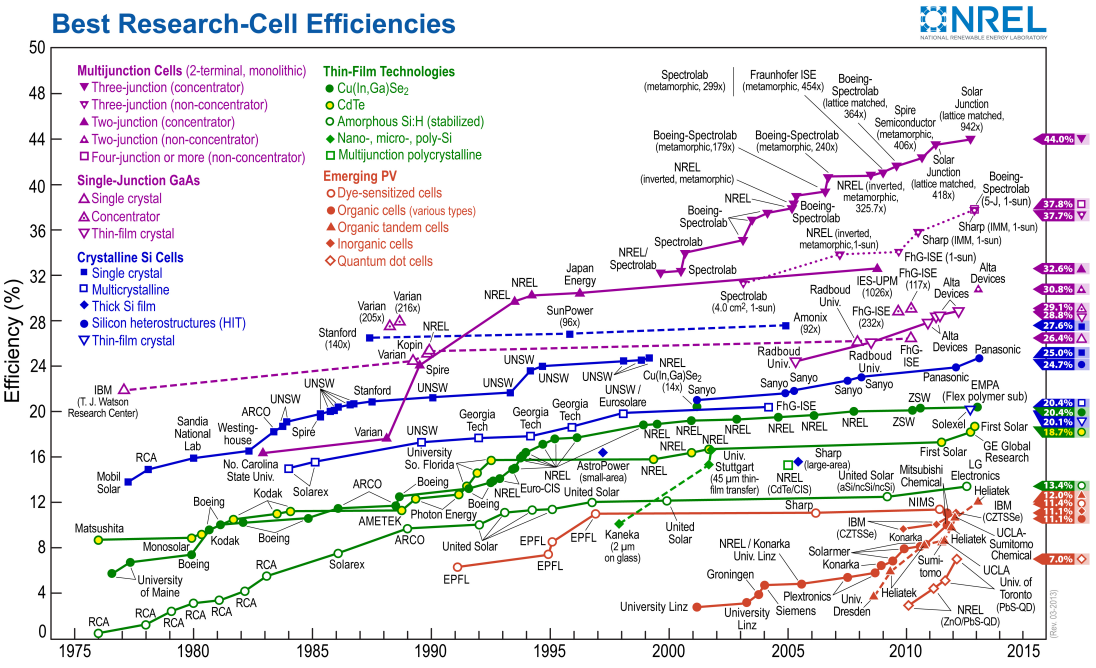

Figure 1.1: Photovoltaic device efficiency within different families of semiconductors. Reproduced from reference [1].

The history of organic photovoltaics started with the discovery of conductive properties in polymers by Heeger, MacDiarmid and Shirakawa in 1977 for which they were awarded the Nobel Prize in Chemistry in 2000 [77]. Polymers were traditionally seen as insulating materials, however, the presence of alternating π-conjugated bonds can confer semiconductive properties to polymers. Research and development in the field of organic solar cells (OSCs) are relatively new compared with traditional electronics. The first double-layer type of organic photovoltaic device was demonstrated in 1986 by Tang et al. with a power conversion efficiency of 0.95% [204]. In 1995, solution processed organic photovoltaics were fabricated for the first time from a blend of polymer and oligomer [235]. Until the early 2000s, the maximum power conversion efficiencies of organic photovoltaics remained around 3% [48, 179, 191]. For a long time, these low efficiencies were seen as a significant barrier to commercialization. However, much research was dedicated to improve the fundamental and technical knowledge in the field, which led to significant improvements in performance. Today, organic photovoltaics demonstrate their potential in becoming a market reality by exhibiting efficiencies greater than 10%. Heliatek, a spin-off from a University of Dresden laboratory in Germany is currently holding the power conversion efficiency record of 12% with a multi-junction OSC. Efficiencies approaching 10% were obtained by several groups with

single-junction devices [71, 76, 156]. From a technological point of view, the physicochemical properties of organic semiconductors open up a new route in the development of photovoltaic devices. One of the key properties is the ability to dissolve organic semiconductors in solvents, which enables OSCs to be fabricated using solution processes similar to those used in the printing industry [9, 20, 26, 33, 58, 60, 106, 107, 154]. Such processes mean easier fabrication of large area and low cost photovoltaics and consequently, a number of innovative devices can be considered, including flexible, transparent, and light weight devices as depicted in Figure 1.2 [34, 87, 194]. In addition, the fabrication of OSCs has a lower energy payback time in the long term and a smaller environmental impact than other technologies [54]. Overall, they represent a promising technology for low cost, accessible and sustainable energy.

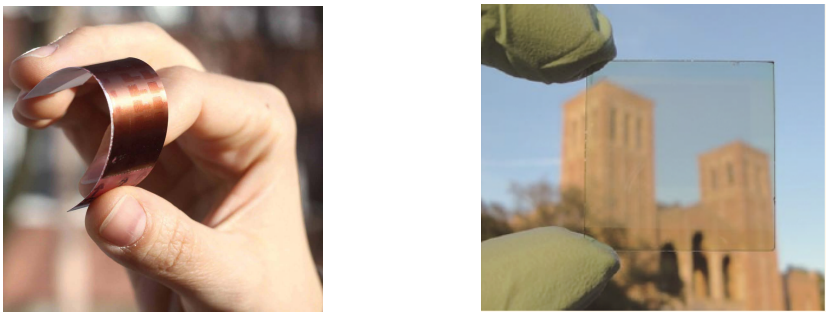

(a) (b)

Figure 1.2: Photographs of (a) an OSC printed on paper, reproduced from reference [87] with permission of Wiley and (b) a transparent OSC, reprinted with permission from [34]. Copyright (2012) American Chemical Society

To become a competitive technology, OSCs need to improve in three fronts: efficiency, lifetime and fabrication cost. Research, with the goal of improving in these areas, has been focused on the synthesis of organic semiconductors, their processing and the development of smart device architectures. All three topics contribute to the overall performance of the final device (Figure 1.3). The past decade was marked by a tremendous increase in types of organic semiconductors [41, 109], which indubitably contributed to the current success of organic photovoltaics. However, the structural properties of materials alone are not sufficient to produce high efficiency devices. The arrangement, e.g. the **morphology**, of the materials is of crucial importance in defining their performance in devices. High efficiency OSCs require a thorough control of the semiconductor morphology to best assess their potential in a device configuration.

In this context, this thesis addresses the interplay between processing method and semiconductor morphology and subsequently photovoltaic performance. The effects

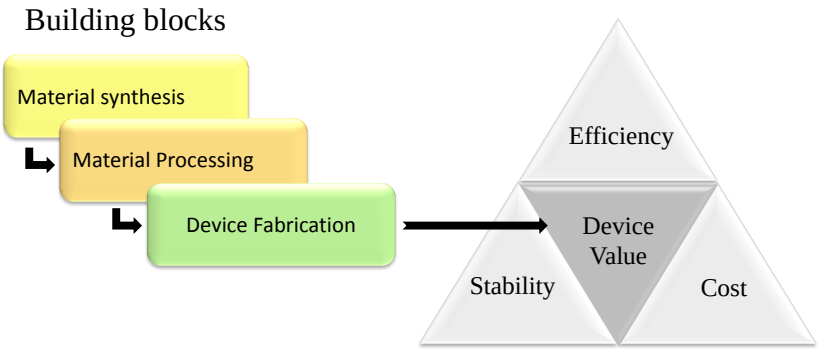

Figure 1.3: Building blocks for device fabrication and the three major axes of performance.

of processing are assessed by means of semiconductor formulation and introduction of processing additive in the formulation.

The first chapter of this thesis provides an introduction to fundamental principles of organic semiconductors and to the field of organic photovoltaics. Chapter 2 presents a detailed literature review on the current state of knowledge on formulation strategies to control active layer morphology. Emphasis is placed on the system based on poly(3-hexylthiophene) (P3HT) and [6,6]-phenyl-C61-butyric acid methyl ester ($PC_{61}BM$) as it is the main model system in this thesis. The objectives of this thesis are described at the end of Chapter 2.

Chapter 3 details the experimental and analytical methods used throughout the thesis.

Chapter 4 reports a novel method for identifying efficient processing additives to be introduced in the formulation of organic semiconductors. Details about the selection method and results confirming the model are presented.

Chapter 5 focuses on the mechanistic effects of processing additives on the morphology and efficiency. Results of structural, optical and electrical characterizations are reported and a mechanism describing the effects of processing additives on the morphology is proposed.

Chapter 6 presents results on the influence of device architecture on the performance of additive-treated OSCs.

The effects of processing conditions on device stability is addressed in Chapter 7. Results of stability tests performed on OSCs processed under different conditions are reported. Also, investigation on the origin of device degradation is presented.

Chapter 8 reports on the investigation of formulation strategies to increase the efficiency of two polymers, other than the model polymer P3HT discussed in the previous chapters.

Chapter 9 summarizes the results and provides suggestions for future work.

1.2 Functioning of solar cells

Before introducing the concept of OSCs, this section discusses the electrical functioning of solar cells and introduces the parameters that characterize their performance.

The simplified structure of a solar cell consists of two electrodes separated by a photo-active layer which contains a p-n junction. A solar cell without any irradiance (dark characteristic) behaves as a diode as shown in Figure 1.4. When a photon hits the active layer, a bond state of an electron and a vacant site of an electron called a hole is formed. The separation of the bound state, also referred to as exciton, generates charge carriers that can travel across the active layer to be collected by the electrodes. The extraction of these photo-generated charge carriers by an external load constitutes the photo-current (J_{ph}). Under illumination, the diode characteristic shifts by the amount of the photo-current.

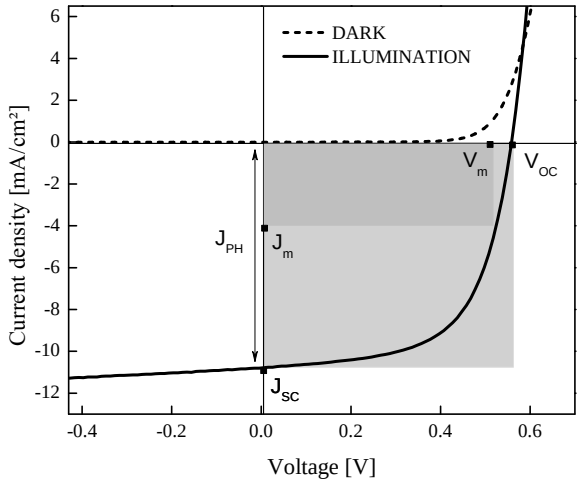

Figure 1.4: Example of a typical solar cell characteristic under light illumination and under dark condition.

The total current density through the solar cell can be analyzed using an equivalent circuit model depicted in Figure 1.5.

The equivalent circuit model consists of four parts: a photo-current source, a diode, a series resistor and a shunt resistor. The diode represents the hole-electron recombination current and the photo-current is the amount of extracted photo-generated charges. The series resistor represents the solar cell internal resistance and the shunt resistor models any leakage current through the device. The total current density J

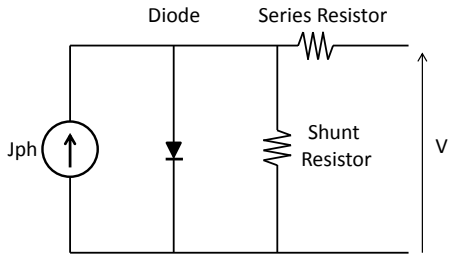

Figure 1.5: Equivalent circuit model for a solar cell.

flowing through the circuit can be described by the following relationship:

$$J = J_D(V) + \frac{V - JR_{serie}}{R_{shunt}} - J_{ph} \tag{1.1}$$

Where R_s is the series resistance, R_{sh} the shunt resistance and J_D the current characteristic for a diode.

The electrical parameters that define the efficiency of a solar cell are extracted from the current density-voltage (J-V) curves measured under light illumination. Devices are characterized by the short-circuit current (J_{sc}), the open-circuit voltage (V_{oc}) and the fill factor (FF). The V_{oc} and the J_{sc} are indicated in the typical J-V curve depicted in Figure 1.4. The J_{sc} is defined as the current at which the applied voltage is equal to 0 V. This parameter represents the number of charge carriers that are photo-generated and collected at the electrodes at short-circuit condition. The V_{oc} is defined as the voltage at which the current density is 0 mA.cm^{-2}. The FF defines the shape of the J-V curve and is defined as:

$$FF = \frac{J_m.V_m}{J_{sc}.V_{oc}} \tag{1.2}$$

where J_m and V_m are respectively the current density and the voltage at the point of the maximum output power, as represented in Figure 1.4. Finally, the power conversion efficiency (PCE) of a solar cell can be calculated as follows:

$$PCE = \frac{V_{oc}.J_{sc}.FF}{P_{in}} \tag{1.3}$$

where P_{in} is the input power density.

Solar cells are typically characterized under 100 mW.cm^{-2} light of the Air Mass 1.5 Global (AM 1.5 G) solar spectrum. The AM 1.5 G spectrum is presented in Figure 1.6, it corresponds to the solar spectrum through atmosphere, 48.2° from zenith.

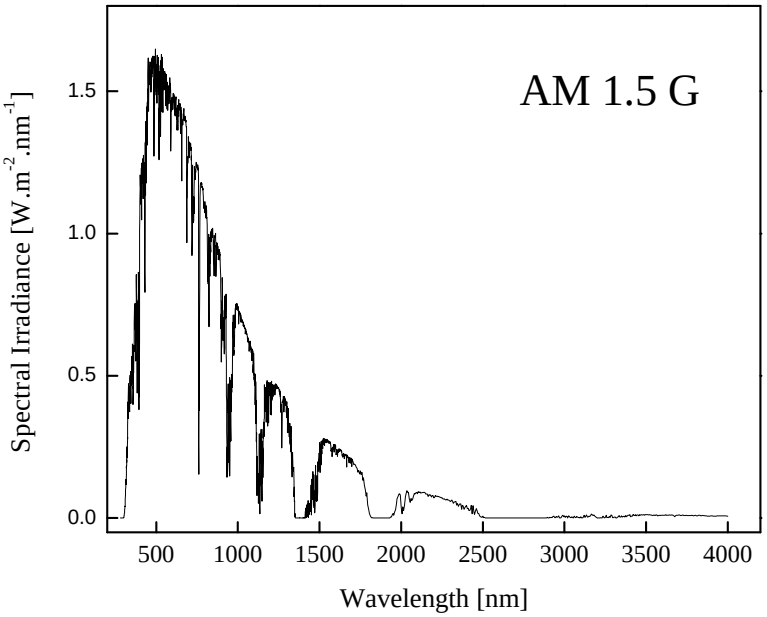

Figure 1.6: AirMass 1.5 Global solar spectrum.

1.3 Organic semiconducting materials

1.3.1 Electronic properties of organic semiconductors

Organic materials are primarily carbon-based. The fundamental property of organic semiconductors is the presence of a conjugated π-electron system within a carbon chain. In such a carbon chain, three out of the four valence electrons of each carbon atom occupy sp^2 hybridized orbitals and are involved in covalent σ-bonds. The remaining valence electron occupies a p_z orbital and can form a π-bond with a p_z electron of a neighboring carbon. As a result, the carbon chain exhibits an alternation of single (σ) and double (σ and π) bonds which constitutes the conjugated π-electron system. The simplest example of a π-conjugated system is that of polyacetylene, illustrated in Figure 1.7, which consists of repeating ethylene units.

Within a π-conjugated system, the overlap of the wave functions of the p_z orbitals of the carbon atom (and also of other atoms such as nitrogen, oxygen, sulfur) results in the formation of the π-band (forming the highest occupied molecular orbital (HOMO)) and the π*-band (forming the lowest unoccupied molecular orbital (LUMO)). Across the conjugated system, the π-electrons are delocalized. The difference between the HOMO and the LUMO levels defines the bandgap of the semiconductor. The gap narrows down as the conjugation length of the polymer chain increases. In molecular solids,

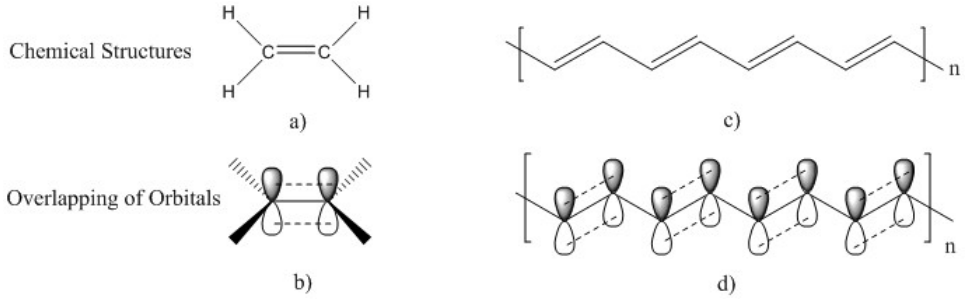

Figure 1.7: Chemical structures of: (a) ethylene, (c) polyacetylene and the overlapping of orbitals in (b) ethylene and (d) polyacetylene.

the degree of intermolecular ordering has a large impact on the energetic landscape in these materials and thus affects the band gap. Overall, increased conjugation length and intermolecular ordering cause a greater degree of electron delocalization while short conjugation length and intermolecular disorder localize electrons.

The specific electronic structure of organic semiconductors leads to major differences between the properties of organic and conventional semiconductors. An understanding of these differences, described in brief in the following sections, is essential to provide insights into understanding the design requirements for OSC active layers.

1.3.2 Charge carrier generation in organic semiconductors

Free charge carriers in semiconductors are generated by light, chemical doping, or injection of charge from an electrode. The generation of charge carriers by light occurs when a photon with an energy equal to or higher than the band gap hits the semiconductor, resulting in the photo-generation of an exciton. To generate free charge carriers, the bound electron-hole pair in the exciton must be separated. In a traditional inorganic semiconductor, the large dielectric constant (around 10 [55]) reduces the Coulomb interaction that binds the hole and the electron. This results in a large-sized type of exciton called a Wannier-Mott exciton characterized by an exciton binding energy in the range of $\sim$ 0.01 eV. This type of exciton can be dissociated by thermal energy at room temperature as the binding energy is lower than the thermal energy (0.025 eV). In contrast, in organic semiconductors, the dielectric constant is much smaller (around 3 [55]) causing a strong Coulombic interaction between the hole and the electron. This results in a small-sized exciton with a high binding energy (from hundreds of meV to

1.5 eV [10, 82, 93]) referred to as a Frenkel exciton. This high binding energy prevents the exciton from being dissociated by thermal energy at ambient temperature. One alternative for exciton dissociation is to introduce a second semiconductor with a different electron affinity. In organic semiconductors, the charge separation is generally a two-step process, where excitons are first separated into less strongly bound electron-hole pairs which can subsequently be dissociated.

1.3.3 Charge transport in organic semiconductors

In crystalline inorganic semiconductors with a 3D crystal lattice, atoms are held together by strong covalent bonds. The strong interatomic interaction leads to the formation of a conduction band and a valence band in which the free charge carriers are highly delocalized and can travel freely throughout the bands [196]. In contrast, in disordered organic semiconductors, such as π-conjugated polymers, charge carriers are localized on individual molecules because of poor intermolecular coupling. The charge transport is generally described by the variable-range hopping model [98, 197] which describes systems with mobilities around or below 10^{-2} $cm^2.V^{-1}.s^{-1}$ [98]. The mobility measures the ease with which the charge carriers move in the system and corresponds to the drift velocity of the charge carrier in an electrical field per unit of electrical field as described in the following equation [21]:

$$\mu = \frac{eD}{K_b T} \tag{1.4}$$

Where D is the diffusion coefficient, e the charge, K_b the Boltzman constant and T the temperature.

In π-conjugated polymers, the hopping transport is highly influenced by the conjugation length and the degree of intermolecular order [21]. The mobility of charge carriers in organic semiconductors thus appears to be dependent not only on the chemical structure of the semiconductors but also, and just as importantly, on their intermolecular arrangements. Generally, for semiconducting polymers processed from solution, mobilities in the range of 10^{-3} - 10^{-6} $cm^2.V^{-1}.s^{-1}$ are obtained [98]. A control over molecular organization can improve the mobility [200]. In the case of highly-ordered organic molecular crystals, charge carriers are sufficiently delocalized for band transport to occur [154].

1.4 Organic solar cells

1.4.1 Active layer architectures

As previously mentioned, thermal energy is not sufficient to dissociate Frenkel type excitons photo-generated in organic semiconductors. Instead, a junction must be created at which it is energetically favourable for an exciton to dissociate.

The first type of OSCs consisted of single layer of semiconductor that formed a rectifying junction with one of the electrodes [12, 28]. In this architecture, because of the high exciton binding energy and the low exciton diffusion length (1 - 10 nm) in organic semiconductors [72, 141, 199], the charge generation only occurs near the interface between the electrode and the active layer. This resulted in poor photo-generation of charge carriers and high series resistance as one of the charge carriers has to travel across the entire active layer to be collected. These issues were later addressed using a heterojunction between an electron donating material (D) and an electron accepting material (A) to form a so-called bi-layer. In a D/A couple, the A is the material with the largest electron affinity and the D the material with the lowest ionization potential. The energy offset at the D/A interface helps to dissociate excitons. The first heterojunction device, developed in 1986, consisted of a bi-layer of an A (tetracarboxylic derivative) and a D (copper phthalocyanine) material. These bi-layer OSCs demonstrated efficiencies approaching one percent (0.95%) [204]. However, the photo-generation of charges was still limited to occur at one single interface and excitons formed further away from the D/A interface do not dissociate into free charge carriers, therefore recombine, and thus do not contribute to photo-current.

A significant improvement with respect to bi-layer devices is the Bulk Heterojunction (BHJ) concept. A BHJ type of active layer consists of an intimate mixture of a D and an A. Such mixtures result in many D/A interfaces throughout the entire active layer and thereby provide a compromise between the amount of interface for exciton separation and D/A pathways for hole/electron transport. Figure 1.8 depicts the schematic of a bi-layer and a BHJ type of active layer. In 1992, Sariciftci et al. revealed a fast photoinduced charge transfer between poly(2-methoxy-5-(2-ethyl- hexyloxy)-1,4-phenylenevinylene) (MEH-PPV) and buckminsterfullerene (C_{60}) [183]. In 1995, solution-processed BHJ-OSCs were fabricated using the property of fast charge transfer between MEH-PPV and $PC_{61}BM$, a soluble derivative of C_{60} [235]. A blend of MEH-PPV and $PC_{61}BM$ was dissolved in xylene and spin-cast to give a thin film consisting

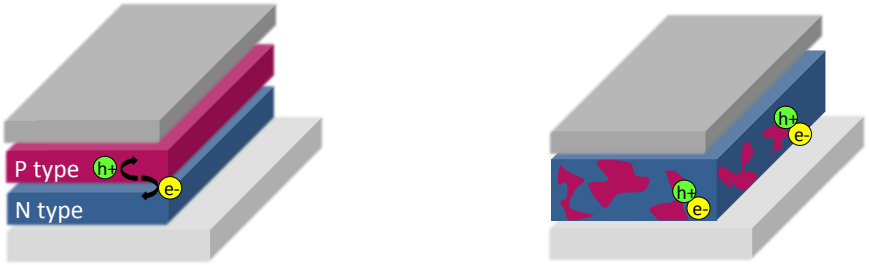

(a) (b)

Figure 1.8: Simplified schematic of (a) a bi-layer active layer and (b) a BHJ-active layer.

of an interpenetrated network between the two materials: a BHJ. The photovoltaic performance revealed that blending $PC_{61}BM$ with MEH–PPV polymer caused the PCE to increase by two orders of magnitude compared with an OSC composed of MEH-PPV only. This BHJ concept is now widely adopted and has been the subject of significant amount of research aimed at increasing the efficiency of solution-processed OSCs.

1.4.2 Formation of BHJ-OSCs

In polymeric BHJs, the D semiconductor is a polymer and the A semiconductor a small molecule. Several examples of A small molecules and D polymers are shown in Figure 1.9.

C_{60} and its derivatives are the most widely used A small molecules. C_{60} is strongly electronegative and can accept up to six electrons. Additionally, it exhibits a small reorganization energy from the ground state to the radical anion upon electron transfer which enables fast photoinduced electron transfer and slows down charge recombination compared to other types of A such as quinone derivatives [67, 88]. As the solubility of C_{60} is low in common organic solvents [189], soluble derivatives such as $PC_{61}BM$ are preferred for solution processed applications. Their HOMO LUMO energy levels are shown in Table 1.1. $PC_{61}BM$ and other fullerene derivatives such as [6,6]-phenyl-C71-butyric acid methyl ester ($PC_{71}BM$) and indene-C_{60}bisadduct (ICBA) are the best performing A small molecules to date. Alternatives have been investigated but have not yet been able to compete with them [174, 177]. On the other hand, D polymers have been the subject of much research resulting in a large panel of π-conjugated polymers. Examples are shown in Figure 1.9.

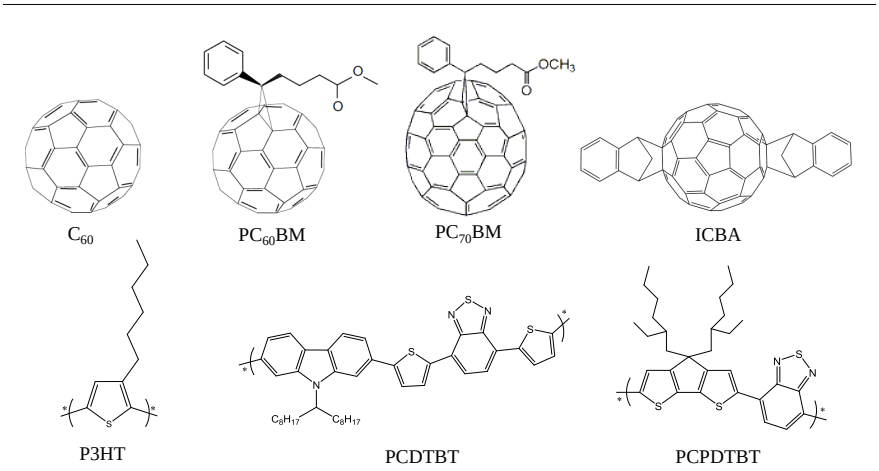

Figure 1.9: Top row: examples of A small molecules and bottom row: example of D polymers.

Table 1.1: HOMO LUMO levels of acceptor materials.

Materials	Energy Levels [eV]		References
	HOMO	LUMO	
$PC_{61}BM$	6.1	4.3	[100, 126]
C_{60}	5.8	3.9	[153, 173]

To form a BHJ, the D polymer and the A small molecule are generally mixed together in a solvent and the resulting blend is coated on a substrate. The drying process involves various phenomena including self-organization of the materials and phase separation between D and A. The resulting phase separation and degree of order in the BHJ govern the conversion from light absorption to charge collection and are therefore crucial to control. It is noteworthy to point here that few studies in the literature focused on the formation of BHJs with fixed morphology by the mean of various methods such as the use of D or A nanoparticles [61] or nanowires.[228, 229] In these approaches, the domain sizes in the BHJ are mainly determined by the size of the initial objects and are less dependent on the conditions of the drying process. This in turn enables a large degree of control in the BHJ morphology under the condition that the sizes of the initial objects are fully controlled.

1.4.3 Functioning of BHJ-OSCs

Within the interpenetrated network formed by the D and A, the conversion from light to electrical current occurs according to the following steps:

(i) Absorption of photon
(ii) Formation of a Frenkel exciton
(iii) Diffusion of the Frenkel exciton to a D/A interface
(iv) Separation of the exciton via charge transfer between D and A resulting in a charge transfer state
(v) Dissociation of the charge transfer state into free charge carriers
(vi) Transport of free charge carriers: the electrons through the A and the holes through the D
(vii) Collection of the charge carriers at the electrodes.

When an OSC is subject to light illumination, photons with appropriate energy are absorbed and cause the photo-generation of Frenkel excitons in the active layer. Because of its high exciton binding energy, the Frenkel exciton can only dissociate at the interface between D and A. This means that only excitons photo-generated within the exciton diffusion length from a D/A interface can contribute to the generation of free charge carriers. Excitons that are formed within a larger distance from this interface undergo geminate recombination and are lost. At the interface, charge transfer from the D to the A is possible if the energy offset at the interface is sufficiently large. Charge transfer occurs if the LUMO level of the A lies between the HOMO-LUMO levels of the D as shown in Figure 1.10. The energy offset between the LUMO of the D and the LUMO of the A has to be greater than 0.3 eV for charge transfer to occur [190]. At the interface, the exciton dissociates to form the charge transfer state corresponding to the e^-/h^+ pair state in which the electron is located on a neighbor molecule of the molecule on which the hole is located. The dissociation of the charge transfer state generates a free electron and a free hole which are then transported through A or D pathways to their respective electrode under the influence of an internal electric field.

In practice, a hole transport layer (HTL) and/or an electron transport layer (ETL) are inserted between the active layer and the cathode and anode respectively to facilitate the process of charge collection and to prevent additional charge recombination at the electrodes. The general energy band diagram of BHJ-OSCs that describes the above mechanisms is depicted in Figure 1.10.

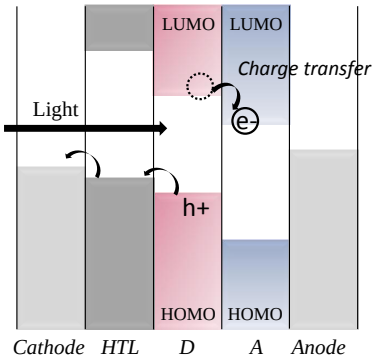

Figure 1.10: Energy diagram in BHJ-OSCs. The figure depicts a situation where the light is absorbed by the D. The photogeneration of the exciton is followed by an electron charge transfer from the LUMO of the D to the LUMO of the A.

The microstructure of the BHJ, e.g. the morphology, affects the efficiency of the different mechanisms described above [24]. The morphology of a BHJ is defined by (1) the phase separation between A and D and (2) the molecular organization.

For high performing OSCs, both charge generation and charge collection need to be considered. These two processes are in competition: charge generation requires small D/A domains to provide a large amount of D/A interface, while charge collection requires large pathways that subsequently limit the amount of D/A interfaces. A compromise is obtained when D and A domain sizes are in the range of the exciton diffusion length. The exciton diffusion length, which is in the range of 1 to 10 nm [72, 141, 199] implies that D and A domain sizes of about 10 nm offer a decent compromise. [68].

In addition to phase separation, the molecular organization within D or A domains is important. In conjugated polymers, the interlayer spacing between polymer chains, the degree of ordering and the orientation of the chains have an influence on charge carrier mobility. In OSCs, charge carrier mobility is closely related to recombination processes [158, 165]. Studies revealed that charge carrier mobility value along with a balance between electron and hole mobility contribute in improving the performance of OSCs [3, 38, 101, 113, 158].

1.4.4 Factors influencing BHJ-OSC efficiency

The previous sections describe the mechanisms related to the functioning of BHJ-OSC and the importance of the BHJ morphology. This section addresses the parameters characteristic of OSCs.

- *Jsc*

The J_{sc} is given by the amount of charge carriers that are collected at the electrodes. This parameter is therefore depends on the amount of photons absorbed and to the loss mechanisms that prevent charge collection. The morphology of the BHJ has a great impact on the amount of photo-generated charges, due to the amount of D/A interface, and on the collection of charges by the presence of D or A pathways. Recent findings have highlighted the important role of the intermixed phase in the BHJ in exciton quenching and charge generation processes [15, 40, 193, 205, 223]. In this intermixed phase, the D and the A are molecularly mixed and form amorphous domains. Studies have shown that it is crucial for these intermixed phases to coexist with the relatively pure D and A domains that stabilize charge separation and enable transport to the electrodes.

- *Voc*

Several works have ascribed the dependence of the V_{oc} to the spectral position of the charge transfer state [111, 133, 209]. The energy of the charge transfer state originates primarily from the energy difference between the HOMO of the D and the LUMO of the A (ΔE_{DA}). ΔE_{DA} determines the theoretical maximum value of V_{oc} [22, 185, 224]. Experimentally, the V_{oc} is observed to be lower than the value set by ΔE_{DA} because of several loss mechanisms at the contacts or in the active layer [209, 232]. In their early work, Scharber et al [185]. investigated the relationship between the energy levels of the D/A blends and the V_{oc} in 26 BHJ-OSCs. They found that the V_{oc} of the OSCs could be estimated by:

$$Voc = \frac{1}{e}(|E^{Donor}HOMO| - |E^{PCBM}LUMO|) - 0.3 \tag{1.5}$$

where e is the elementary charge and the value of 0.3 an empirical factor accounting for losses in OSCs.

Regarding the loss at the contacts, the properties of the HTL (energy levels and conductivity) were shown to have an influence on the built-in voltage in the device and subsequently on the V_{oc} [207]. In the case of ohmic contacts, the loss in V_{oc} at the contact was attributed to diffusion of charge carriers into the active layer at the interface with the metal electrodes resulting in a reduction of the voltage at which the flat band conditions are reached [210]. Regarding the active layer, several loss mechanisms that affect the charge transfer band position were identified. The charge transfer band was found to be dependent on the electrostatic environment, which can be altered by

the concentration of $PC_{61}BM$ nanocrystals because of their high dielectric permittivity [133, 175]. Also, the level of polymer aggregation affects the position of the charge transfer state because of its dependence on intermolecular interactions [172]. Strong intermolecular interactions were shown to result in low V_{oc} whereas low intermolecular interactions - obtained in the case of amorphous polymers, for example - lead to higher V_{oc}.

- *FF*

The origins of low FF generally arise from space-charge build up. The space-charge regions can arise in the vicinity of the active layer and the contacts, in the case of poor charge extraction at the electrodes. In this context, the nature of the charge transport layers between the active layer and the electrodes have the important role of preventing charge accumulation [163]. Efficient contacts and interlayers facilitate the extraction of charges and reduce bimolecular recombination in the active layer. Space-charge build up can also be observed in the case of increasing light intensity [111, 227], or unbalanced charge carrier mobility [3, 109]. The value of the FF is generally found to be dependent on the values of R_s and the R_{sh} measured in OSCs [97, 172].

This chapter provided an overview of the mechanisms behind OSCs and more specifically of BHJ-OSCs. The next chapter focuses specifically on the formation of that morphology and strategies to control and optimize it.

Chapter 2

Formulation strategies for controlling BHJ morphology

This chapter reviews the benefits and the limitations of three main strategies that can control the morphology of BHJ-active layers: the solvent choice, the use of post-processing steps and the use of processing additives. The objectives of the thesis are presented at the end of the chapter.

2.1 Role of solvent

The BHJ morphology is strongly dependent on thermodynamic and kinetic aspects involved during spin-casting and drying of the material formulation to form the thin film [144, 233]. The thermodynamics of the system is dictated by the intrinsic properties of the D and A materials (their tendency to crystallize, their interactions with each other and their miscibility) and by the properties of the solvent. The kinetics of drying primarily depend on the boiling point and the vapor pressure of the solvent. The effects of the solubility properties and the boiling point of solvents are reviewed below.

- Solubility properties

D and A solubility properties in solvent were found to affect the aggregation of the fullerene derivatives in the D/A films. Table 2.1 displays the solubility limits of $PC_{61}BM$ in some conventional solvents including chloroform (CF), chlorobenzene (CB), o-dichlorobenzene (ODCB) and 1,2,4-trichlorobenzene (TCB). The study by Brabec et al. on a blend of MDMO-PPV and $PC_{61}BM$ was among the first to bring some insights into the relationship between solvent quality and the morphology of a BHJ [191]. In the D/A system based on MDMO-PPV/$PC_{61}BM$, the size of $PC_{61}BM$ aggregates were found to be dependent on the solubility limit of $PC_{61}BM$ in the solvent [57, 84, 85]. When poor solvents are used (such as pyridine and toluene), the BHJ exhibits large size aggregates of $PC_{61}BM$ in the order of hundreds of nanometers. In the films spin-cast from good solvents, such as CB or ODCB, the large features are absent. Figure 2.1 shows atomic force microscopy (AFM) images that clearly depicts the dependence of $PC_{61}BM$ aggregate sizes on solvent quality. This morphology is attributed to the fact that in good solvents, $PC_{61}BM$ molecules remain finely dispersed and no over-sized aggregates are formed. Smooth films of MDMO-PPV/$PC_{61}BM$ exhibited the highest PCEs, in the order of 2.5%.

Table 2.1: Boiling points and solubility limits of $PC_{61}BM$ in various solvents.

Solvents	Boiling point	Solubility limit of $PC_{61}BM$	References
CF	61 °C	25 - 26 mg.mL^{-1}	[32, 51, 57, 181]
CB	132 °C	25 - 59.5 mg.mL^{-1}	[32, 51, 57, 181]
ODCB	183 °C	42 – 107 mg.mL^{-1}	[57, 162]
TCB	214 °C	81.4 mg.mL^{-1}	[162]
Toluene	112 °C	9 - 15.6 mg.mL^{-1}	[32, 51, 57, 181]
Xylene	138 °C	5 - 22.1 mg.mL^{-1}	[32, 51, 57, 181]
Mesitylene	163 °C	47 - 48.1 mg.mL^{-1}	[32, 51]
Carbon Disulfide	46 °C	207 mg.mL^{-1}	[57]

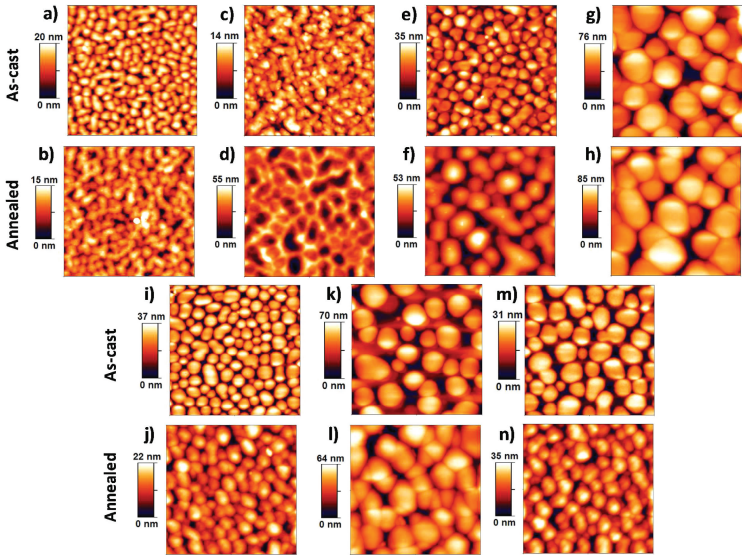

Figure 2.1: AFM topography images (2 μm x 2 μm) of as-cast and annealed films of MDMO-PPV-$PC_{61}BM$ spin-cast from (a, b) chlorobenzene (CB), (c, d) carbon disulfide, (e, f) chloroform (CF), (g, h) pyridine, (i, j) trichloroethylene, (k, l) toluene and (m, n) 1-methylpyrrole. Reproduced from reference [57] with permission of Wiley.

Similar results were reported with blends of PCDTBT/$PC_{61}BM$ [16, 166, 192] and P3HT/$PC_{61}BM$ [181, 206]. In a BHJ of P3HT/$PC_{61}BM$, it is well known that thermal annealing causes $PC_{61}BM$ to crystallize and to form microcrystals [31, 148]. Several studies revealed that thermally annealed BHJs presented the largest $PC_{61}BM$ microcrystals when spin-cast from poor solvents of $PC_{61}BM$ [181, 206]. Clearly, when $PC_{61}BM$ is blended with P3HT or MDMO-PPV, the crystallization of $PC_{61}BM$ molecules

is governed by its solubility limit. When comparing P3HT and MDMO-PPV, it is worthy to note that the crystallization of $PC_{61}BM$ seems to depend more on solvent quality when MDMO-PPV is the D. This divergent behavior was attributed to the different strength of the interactions between the polymer and the fullerene components [187]. Overall, the aggregation of $PC_{61}BM$ is shown to be affected by the D-A interactions and to be dependent on the type of solvent used.

The effect of the solvent quality on the polymeric component is another important aspect to consider. A common method to investigate the effects of solvent quality on the behavior of P3HT chains is to add a poor solvent for the polymer (e.g., acetone or hexane) to the host solvent in order to reduce the solubility of the polymer in the solvent system. Keum et al. studied the structural evolution, in solution, of P3HT chains as a function of the solvent quality, using UV-Vis absorption spectroscopy and small-angle neutron scattering [95]. They showed that the introduction of a poor solvent caused the P3HT chains to aggregate and to grow into nanorods in order to reduce the unfavorable solvent-polymer interactions. As a consequence of the preformed aggregates in solution, the crystallinity of P3HT in the dry film greatly improved [186]. Chang et al. used grazing incidence x-ray diffraction (GIXD) to show that the introduction of acetone in the solvent system increased the crystallinity of P3HT (Figure 2.2) causing as much as a 4-fold increase in mobility [32]. Overall, poor solvent quality affects the behavior of the polymer by introducing a driving force for the polymer to aggregate in order to reach a thermodynamically favorable state.

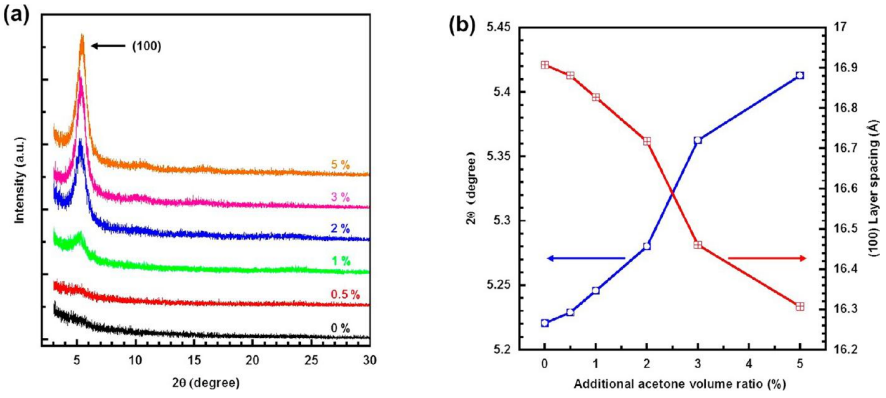

Figure 2.2: (a) GIXD profiles of P3HT films spin-cast from P3HT/CF solutions containing a range of added acetone; (b) 2θ angle (left axis) of (100) peak and corresponding layer spacing (right axis) as a function of the additional acetone volume ratio. Reprinted with permission from [32]. Copyright (2013) American Chemical Society.

- Solvent's boiling point

The organization of the material and the transition from the liquid to the solid state can be affected by the drying kinetics. Using highly volatile solvents, the kinetics of evaporation can be much higher than the kinetics of crystallization. In such cases, the resulting morphology is far from that observed under equilibrium conditions [157]. The effects of the drying kinetics on the amount of polymer chain aggregation have been widely investigated using various deposition techniques [233] and solvents with different boiling points. When P3HT/PC_{61}BM films were spin-cast from different solvents, it was generally observed that a high boiling point solvent leads to better efficiency [52]. Ruderer et al. studied the morphology of P3HT/PC_{61}BM films spin-cast from four different solvents (CF, CB, toluene and xylene) [181]. Using grazing incidence wide angle x-ray scattering, they showed that the crystallite sizes of P3HT increased with increasing boiling point of the solvent. Similarly, Verploegen et al. showed that films spin-cast from CB gave larger crystal sizes than films spin-cast from CF [211]. This was attributed to the fact that a high boiling point solvent resulted in slow drying that provided time for the self-assembly of polymer chains during solvent evaporation. These results indicate that spin-casting from high boiling point solvents allows the P3HT component to arrange in a lower free-energy state compared with thin films spin-cast from a low boiling point solvent. This phenomenon is also observed with several other D polymers such as PCPDTBT and PTB7 [59, 69].

The examples above show that the choice of solvents has a large impact on the morphology of the BHJ. During solvent evaporation, the drying kinetics and thermodynamics are in competition. For P3HT/PC_{61}BM blends, high boiling point solvents are preferred to provide time for the polymer chains to self-assemble. An appropriate choice of solvent can, therefore, optimize the morphology of a BHJ. However, there is a only a limited number of solvents that can solubilize both D and A components. In the best solvents, as cast P3HT/PC_{61}BM-OSCs still exhibit low PCEs generally reported to be below 1.5% [29, 230]. The poor performance is due to fast solvent evaporation caused by the use of spin-coating (or any other deposition technique). The fast solvent evaporation prevents the materials from aggregating and forming proper phase separated domains. As a result, P3HT and PC_{61}BM form an intimately mixed network lacking of well defined domains. This, in turn, primarly limits charge collection and results in low J_{sc} and FF. The application of post-processing steps were demonstrated to enable further optimization of the BHJ morphology.

2.2 Effects of post-processing steps

Thermal treatment - also called thermal annealing - on P3HT/PC_{61}BM-films was shown to significantly increase the degree of crystallinity of P3HT. Figure 2.3 shows the effects of thermal annealing on P3HT/PC_{61}BM films observed by UV-Vis absorption spectroscopy and by XRD measurements. UV-Vis absorption spectroscopy represents a useful technique to detect the degree of crystallinity of P3HT because increased crystallinity induces a red-shift in the absorption peak and the appearance of two vibronic peaks around 555 nm and 605 nm [237]. In the XRD pattern in Figure 2.3b, the diffraction peak at 5.5° corresponds to the edge-on orientation of the polymer chains [238]. The appearance of the diffraction peak is a signature of increased crystallinity.

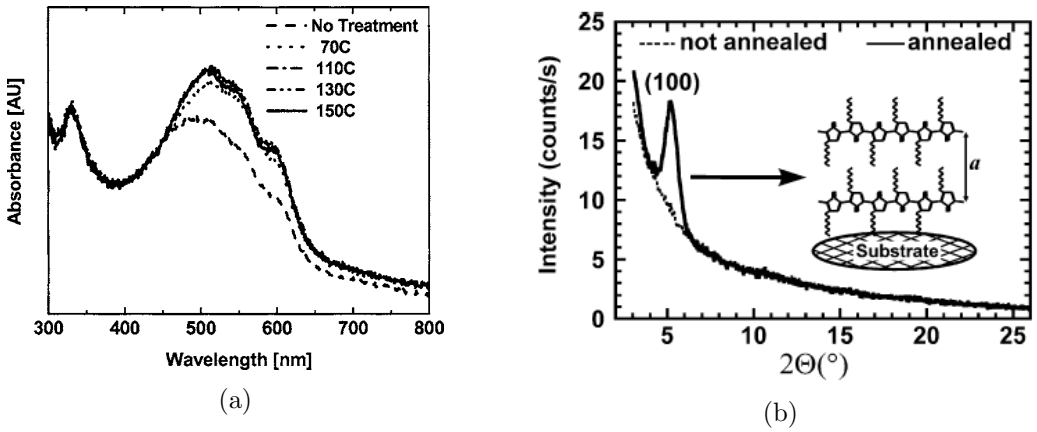

(a) (b)

Figure 2.3: Effects of thermal annealing on the crystallinity of P3HT depicted by (a) an appearance of P3HT vibronic bands in UV-Vis absorption spectra (b) an increase in diffraction peak of P3HT in XRD pattern. Figures (a) and (b) are respectively reproduced from references [116] with permission of AIP Publishing LLC and [238] with permission of Elsivier.

The increased degree of P3HT crystallinity is attributed to the fact that the polymer becomes mobile upon annealing and can self-assemble into crystalline domains. This leads to increased ordering between polymer chains. In parallel to the increased ordering of polymer chains, PC_{61}BM molecules diffuse out of the polymeric matrix and aggregate to form needle-like crystallites that can reach sizes up to a few microns under extensive thermal annealing. Upon moderate thermal annealing, P3HT and PC_{61}BM are subject to phase separation causing an increase in D and A domain sizes. Most studies report thermal annealing for a duration of 1 to 30 minutes at temperatures ranging from 110 ^{o}C - 160 ^{o}C. Upon controlled thermal annealing, J_{sc} and FF were shown to significantly increase resulting in PCEs of up to 5% [43, 115, 134, 160, 238].

A slow drying approach - or solvent annealing - was also used to control the morphology of P3HT/PC_{61}BM-films. This approach generally involves spin-casting the D/A for a short period of time so that the resulting film still contains solvents; the film can then be placed in a solvent saturated environment. In the saturated environment, the solvent evaporation is slowed compared with evaporation during conventional spin-casting. Similarly to what is observed in thermal annealing, the degree of P3HT crystallinity increases and high efficiencies are obtained upon solvent annealing [50, 78, 117]. This approach can be interpreted as an extension of the effects of high boiling point solvents described in section 2.1: during solvent annealing, the polymer chains are given more time to aggregate which results in an overall increase in domain sizes and degree of crystallinity [164, 211].

Post-processing steps can increase the efficiency of P3HT/PC_{61}BM-based OSCs. From a fundamental point of view, these approaches also provide insight into the relationship between active layer morphology and photovoltaic performance. In practice, however, thermal annealing is hardly compatible with flexible substrates that require low temperature processing conditions; overall the post-processing steps are difficult to implement in a large area high throughput line of fabrication without impacting the final cost of OSCs. Additionally, these approaches are inefficient for some low band gap polymers [44, 166]. These limitations motivate the need of a different strategy to control the BHJ morphology - specifically the use of processing additives in D/A formulations.

2.3 Use of processing additives in BHJ-OSCs

A processing additive refers to a solvent which is introduced in small proportion (generally a few volume %) into the host solvent used to solubilize the active materials. In 2006 - 2007, Peet et al. showed that introducing 1,8-octanedithiol (ODT) in a D/A solution blend increased the photocurrent and the PCE of OSCs using P3HT or PCPDTBT as D materials [169, 170]. For PCPDTBT/PC_{70}BM-based OSCs, the PCE was increased from 2.8% to 5.5%. This pioneering work represented an exciting discovery as processing additives were seen as a new method for improving the photovoltaic performance of OSCs in addition to the conventional post-processing steps.

Further work led to two competing theories regarding the specific properties of what makes a solvent an efficient processing additive. In 2008, Yao et al. proposed that

processing additives should possess:[234]
(i) a lower vapor pressure than the host solvent and
(ii) a lower solubility limit towards the fullerene derivative acceptor than that of the host solvent.
They based their selection rules on the P3HT/$PC_{61}BM$ system and suggested that during spin-casting, the processing additive and the host solvent evaporate with different rates because of the difference in vapor pressure. The host solvent, with a higher vapor pressure, would evaporate more quickly causing an increase in the additive concentration in the solvent mixture. As a consequence, the solvent quality towards $PC_{61}BM$ would decrease, leading to early formation and precipitation of clusters. This mechanism is illustrated in Figure 2.4. With a smaller amount of $PC_{61}BM$ in the solution, the P3HT chains would be able to self-organize more easily and form more crystalline domains at the origin of the improved active layer morphology.

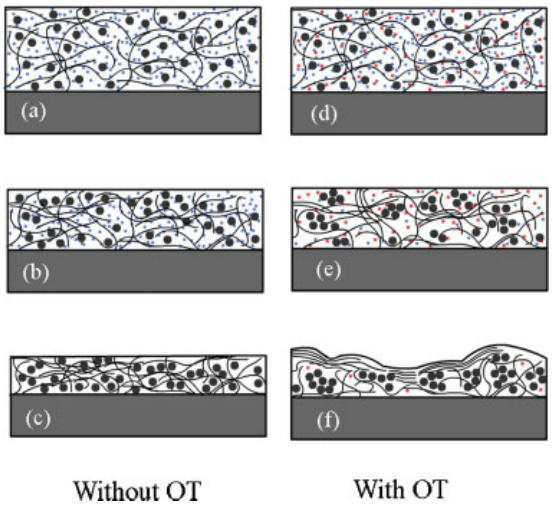

Figure 2.4: Proposed model during spin-coating process. Black wire: P3HT polymer chain; big black dots: $PC_{61}BM$; blue dots: ODCB molecules; and red dots: ODT molecules. (a–c) correspond to three stages in the spin-coating process when ODCB is the sole solvent; (d–f) correspond to three stages in the spin-casting process when ODT is added in ODCB. Reproduced from reference [234] with permission of Wiley.

In the same year, Lee et al. proposed a different set of criteria for selecting processing additives, claiming that an ideal processing additive should have [114]:
(i) a good solubility towards the fullerene derivative acceptor,
(ii) a poor solubility towards the polymer and
(iii) a boiling point higher than that of the host solvent.
The mechanism proposed here is based on the fact that processing additives are good solvents for the fullerene derivatives and are poor solvents for the D (such as P3HT or PCDTBT). During the transition from the liquid to the solid states, the high boiling

point of the solvent means that the fullerene derivatives remain longer in the solution state; this enables control of the phase separation between the polymer and the small molecule. Such a mechanism is depicted in Figure 2.5.

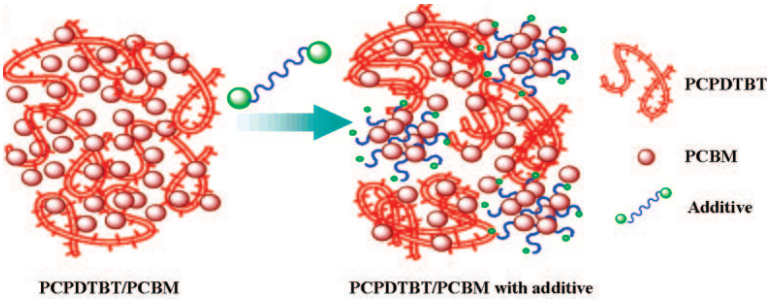

Figure 2.5: Schematic of the role of the processing additive in the self-assembly of BHJ blend materials. Reprinted with permission from [114]. Copyright (2008) American Chemical Society.

This mechanism is therefore based on the differential solubility of the additive towards the polymer and the fullerene derivative whereas the first mechanism accounts for the poorer solubility of the acceptor derivative in the additive compared with the host solvent. So far, however, no clear selection rules for selecting processing additives have emerged.

Experimentally, other solvents were found to increase the PCE of OSCs: alkanedithiol with various alkane chain lengths [159, 169, 182], 1,8-diiodooctane (DIO) [114, 131], 1-chloronaphthalene (CN) [7, 11, 92, 147], nitrobenzene [47], 1-methyl-2-pyrrolidinone (NMP) [234] and 1,8-dichlorooctane [66, 114] among others [125, 128]. Figure 2.6 depicts the chemical structures of some of the processing additives found in literature.

For the D/A system based on P3HT/$PC_{61}BM$, introducing nitrobenzene or alkanedithiols in the D/A solutions increased the PCEs up to 4% [149, 159]. These efficiencies are in the range of those normally obtained with post-processing steps [37, 159]. High efficiency P3HT/$PC_{61}BM$-based OSCs can therefore be fabricated without the use of post-processing steps, which is particularly appealing for the prospect of low fabrication cost and large area OSCs [58]. Literature shows that processing additives can increase the efficiency of OSCs in a wide range of D/A systems by optimizing the active layer morphology [63, 125, 171, 217]. Table 2.2 shows examples of some of these D/A systems along with the PCE values before and after introducing the processing additives. Based on these examples, it is clear that the use of processing additives

represents a widely applicable and efficient approach to optimize a large range of D/A systems.

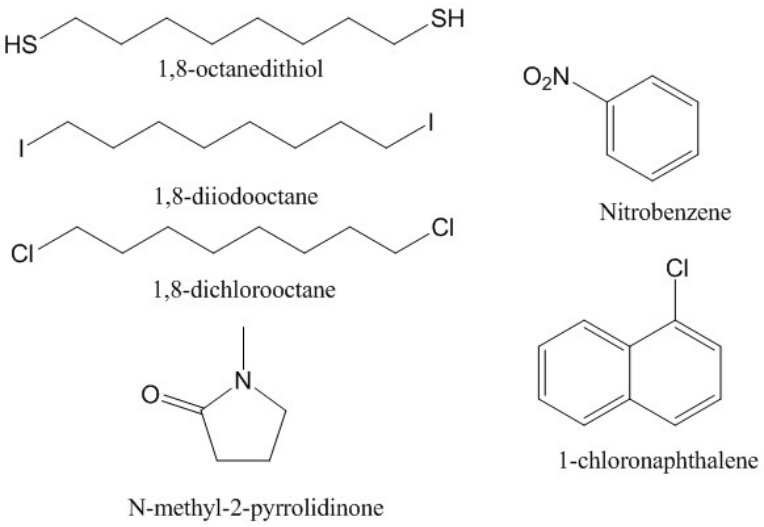

Figure 2.6: Chemical structures of processing additives.

Table 2.2: Effects of processing additives on the PCE of several types of D/A OSCs.

D/A systems[1]	Processing additive	PCE w/o additive [%]	PCE with additive [%]	Phase separation	Ref.
P3HT/$PC_{61}BM$	ODT	0.6	2.6	increase	[37]
	1,6-hexanedithiol	0.46	3.16	increase	[182]
	Nitrobenzene	1.2	3.94	-	[149]
	Dodecanedithiol	1.74	4.03	-	[159]
	NMP	0.29	∼1.5[2]	-	[234]
P3HT/$IC_{70}BA$	DIO	1.15	2.97	decrease	[70]
	ODT		3.09	decrease	
PCDTBT/$PC_{71}BM$	DIO	4.89	5.91	increase	[131]
PCPDTBT/$PC_{71}BM$	Alkanedithiol	2.8	5.5	increase	[35]
	DIO	2.6	4.5	increase	[8]
	ODT	3.35	4.5	increase	[114]
	DIO	3.35	5.12	increase	[114]
	1,8-dibromooctane	3.35	4.66	increase	[114]
PCPDTBT/$PC_{61}BM$	DIO		4.62	increase	
	ODT	1.68	3.87	increase	[66]
	1,8-dichlorooctane		3.45	increase	
PTB7/$PC_{71}BM$	DIO	3.92	7.4	decrease	[124]
DPPT/$PC_{61}BM$	DIO	0.6	3.4	decrease	[127]
DPPBT/$PC_{61}BM$	DIO	1.0	5.2	decrease	[127]
PDTSTPD/$PC_{61}BM$	DIO	1.0	7.3	decrease	[6, 46]

[1]The acronyms used for the D and A materials are defined in the Abbreviations section

[2]No exact PCE was reported

2.4 Context and objectives of the thesis

High-efficiency OSCs require a controlled and optimized BHJ morphology. Solvent choice in the D/A formulation is of major importance, but has a limited impact on the morphology due to the limited number of good solvents available for organic semiconductors. Also, upon spin-casting, the drying kinetics often dominate over the thermodynamic aspects of the D/A system, which leads to poor phase separation and

subsequently low PCE in the case of P3HT/PC_{61}BM. Post-processing steps were successful in optimizing P3HT/PC_{61}BM-based OSCs, but were not efficient in optimizing several systems based on other low band gap polymers. Additionally, post-processing steps are not ideal when thinking towards flexible and low-cost OSCs.

The use of processing additives appears to be a key approach to optimize D/A morphology: it is widely applicable and compatible with large area and high throughput fabrication of OSCs. While many studies have reported the success of processing additives in increasing the PCE of OSCs, fundamental aspects surrounding their use have not been addressed as successfully.

So far, there has been no systematic approach to identify suitable processing additives for a given D/A system. Very few studies have addressed the issue of how to identify or select processing additives from the vast array of available solvents. Consequently, their selection is generally the result of trial and error experiments.

Comparing the different studies in the literature also shows that there is no clear consensus on the mechanistic role of processing additives in influencing and controlling the BHJ morphology. Their effects on D/A phase separation have been the subject of several studies. The results of such studies, summarized in Table 2.2, show that the effects of processing additives on phase separation vary with the type of D/A blend under investigation: in some cases they increase the phase separation while in other cases, they decrease it. In the case of D/A blends based on P3HT, the literature reports contradictory results regarding the effects of additives on phase separation.

Another major aspect not considered in the literature is the effect of additives on the long-term stability of OSCs. As OSC stability is equally important as the PCE, investigating their effects on stability is of major importance.

An in-depth understanding of the effects of processing additives is required to enable and accelerate the development of efficient D/A formulations. This thesis aims to carry out a comprehensive investigation of processing additives, addressing the following objectives:

1. To establish a predictive method for identifying processing additives for D/A systems with certain given properties.

2. To elucidate the mechanistic role of processing additives in influencing and controlling the BHJ morphology and subsequently, the OSC performance.

3. To determine the impacts of the processing additive approach on the stability of OSCs.

In pursuit of these objectives, the study will primarily focus on the archetypical P3HT/$PC_{61}BM$ system. The last chapter of this thesis deals with the effects of processing additives in systems using other types of D polymers.

Chapter 3

Experimental details

3.1 Fabrication and characterization of OSCs

This PhD thesis being done in the context of a co-tutelle program between the University of Waterloo and the University of Bordeaux, the experimental details differ from experiment to experiment. Experimental details are described according to the laboratory where the studies were conducted.

Experiments reported in Chapters 4, 6 and 8 were performed at the University of Bordeaux laboratory (UB Lab).

Experiments reported in Chapters 5 and 7 were performed at the University of Waterloo Laboratory (UW Lab).

3.1.1 Materials and substrates

The P3HT and $PC_{61}BM$ were purchased from Solaris Chem Inc. and used as received. The P3HT has a molecular weight of 53 kDa and a polydispersity index of 1.49. The purity of $PC_{61}BM$ is 99.74%.

The PCDTBT is purchased from Solaris Chem Inc., its molecular weight is 85 kDa.

The PDQT was synthesized in UW Lab according to the literature [123]. The average molecular weight is 21100 and the polydispersity index 2.72.

The solvents: 1,2-dichlorobenzene, chlorobenzene were purchased from Sigma Aldrich and used as received. The processing additives: dimethyl phthalate, 1,8-octanedithiol, 1,8-diiodooctane, 1-cyclohexyl-2-pyrrolidinone, tributyl-o-acetylcitrate were purchased from Sigma Aldrich and used as received. 1-chloronaphthalene was purchased from TCI Chemical N.V. and used as received.

Zinc acetate dihydrate was purchased from Sigma Aldrich with a purity above 99.9%.

At UB Lab, the ITO coated substrates used for device fabrication were purchased from Kintec. The resistance of the ITO layer is 10 Ω/square. The shadow masks used for device fabrication enable the fabrication of four OSCs, with a surface area of 8.6 mm^2, on each substrate.

At UW Lab, the ITO coated substrates were purchased from Luminescence Technology Corporation. The resistance of the ITO layer is 15 Ω/square. The shadow masks used

for device fabrication enable the fabrication of three OSCs, with surface areas of 10 mm^2, 12.5 mm^2 and 17.5 mm^2, on each substrate.

3.1.2 Active layer formulation

The organic semiconductors are weighed with the desired proportion in vials. Solvent mixtures are introduced to the organic semiconductors to solubilize them. The preparation of solvent mixtures differs as a function of the proportion of processing additive in the host solvent.

For mixtures with a processing additive concentration below 0.8 vol%, the solvent mixture is prepared separately by blending and stirring the additive and the host solvent for 1 - 2 hours at ambient temperature. The prepared solvent mixture is further introduced in the vial containing the organic semiconducting materials. For solvent mixtures with a processing additive concentration above 0.8 vol%, the solvent and the processing additive are introduced directly with the desired concentration in the vial containing the organic semiconductors.

The final mixture containing the solvent mixture and the organic semiconductors is first stirred for 15 - 20 minutes at 90 °C in order to ensure an efficient dissolution of the polymer and to avoid large aggregates. The mixture is then stirred at 50 °C. For P3HT/PC_{61}BM solutions, the mixtures are found to be stable up to at least 6 weeks. Therefore P3HT/PC_{61}BM solutions were kept and re-used several times. For PCDTBT/PC_{61}BM and PDQT/PC_{61}BM solutions, the mixtures were stirred for a maximum period of 12 hours prior to use.

3.1.3 Substrate cleaning

The ITO coated substrates were systematically cleaned in an ultrasonic bath of acetone, ethanol and isopropanol for 15 minutes each. The substrates were then dried using a nitrogen gun and were treated in a UV-ozone oven (in UB Lab) or were treated with O_2 Plasma (in UW Lab).

3.1.4 Fabrication of OSCs using a conventional architecture

For conventional OSCs, the cleaned ITO substrates were treated under UV-ozone for 20 minutes. On top of cleaned ITO coated substrates, a thin layer of PEDOT:PSS

(Baytron P, Bayer AG/Germany) was spin-cast at 4000 rpm for 60 seconds in air. The sample is further dried at 110 °C in a vacuum oven for 20 minutes. The thickness of the PEDOT:PSS layer was determined to be $\sim$ 50 nm.

The D/A solution is further deposited by spin-casting in a glovebox environment (O_2 and H_2O levels < 0.1 ppm). Finally, calcium (20 nm) and aluminum ($\sim$ 50 - 70 nm) were thermally evaporated under a secondary vacuum (10^{-6} mbar) onto the active layer through a shadow mask.

Due to the low stability of conventional OSCs in atmosphere conditions, conventional OSCs are either measured in a glove box environment, or encapsulated (using a photo-sensitive epoxy glue to glue a glass substrate on top of the top electrode) prior to J–V characterizations measurement in air.

3.1.5 Fabrication of OSCs using an inverted architecture

For inverted OSCs, the cleaned ITO substrates were treated under UV-ozone for 10 minutes or O_2 plasma for 2 minutes. A zinc acetate precursor solution is prepared by dissolving 196 mg of zinc acetate dihydrate in 6 mL of ethanol absolute. 54 μL of ethanolamine is then introduced. The solution is then stirred on a hotplate for 2 hours at 45 °C and subsequently filtered using a 0.45 μm cellulose acetate filter. On top of cleaned ITO coated substrates, the solution of zinc acetate precursor solution is spin-cast at 700 rpm for 60 seconds. The ZnO layer is further thermally annealed on a thermally controlled hot plate at 180 °C for 60 minutes. The D/A solution is further deposited by spin-casting in a glovebox environment (O_2 and H_2O levels < 0.1 ppm). Finally, molybdenum oxide (7 nm) and silver (70 nm) were thermally evaporated under a secondary vacuum (10^{-6} mbar) onto the active layer through a shadow mask.

3.1.6 J–V characteristics measurements of OSCs

At UB Lab, J-V analysis was conducted using a K.H.S. SolarCelltest- 575 solar simulator with AM1.5G filters set at 100 mW.cm^{-2} with a calibrated radiometer (IL 1400BL). A LabVIEW-controlled Keithley 2400 SMU enabled the measurement of J-V curves.

At UW Lab, the J–V analysis was conducted on ABET technologies Sun 2000 Solar Simulator with AM1.5G filters set at 100 mW.cm^{-2}. A LabVIEW-controlled Keithley 2400 SMU enabled the measurement of J-V curves.

J_{sc}, V_{oc}, FF and the PCE were extracted from the Labview softwares used for the J–V characterizations. The shunt resistance (R_{sh}) and the series resistance (R_s) can also be extracted from the J-V characteristics.

Three regions of the J-V characteritsics can be defined as a function of the value of the applied voltage:

- At low voltage, the J-V characteristic is primarily determined by R_{sh} which can be determined from the slope of the J-V characteristic at V = 0 V:

$$\frac{1}{R_{sh}} = (\frac{dJ}{dV})_{V=0} \tag{3.1}$$

- At intermediate voltage, the diode parameter dominates.

- At higher voltage, the J-V characteristic is primarily determined by R_s. There are several methods for determining and fitting R_s. One of the simplest is to determine the slope of the J-V curve at high voltage. In the literature, the slope is found to be determined at different voltage values [45, 91, 205, 213]. It is however common to determine the series resistance at V_{oc} in order to be close to the operating conditions:[94, 102]

$$\frac{1}{R_s} = (\frac{dJ}{dV})_{V=V_{oc}} \tag{3.2}$$

3.2 Mobility measurements

In this thesis, the measurements of charge carrier mobilities are determined by two methods: the determination of charge carrier mobility in an organic thin film transistor (OTFT) configuration and in a single diode configuration.

3.2.1 Mobility measurement in OTFT configuration

An OTFT is a three-terminal device with a gate, a source and a drain. The current flowing between source and drain (I_{DS}) can be controlled by the applied gate voltage across a thin dielectric film. By applying a gate source voltage (V_{GS}) across the dielectric, a channel of charge carriers is induced in the semiconductor layer at the interface with the dielectric. This channel allows the drain current to flow through the

semiconductor when another voltage (the drain source voltage V_{DS}) is applied between the drain and the source. If V_{GS} is positive, negative charges will be attracted to the interface between the semiconductor and the dielectric, the channel is called n-type channel. On the contrary, when V_{GS} is negative, positive charges are induced at the interface between semiconductor and dielectric and the channel is a p-type channel. Electron mobility can be extracted from the n-type OTFT, while hole mobility can be extracted from the p-type OTFT.

The OTFT architecture used in this work is bottom gate, top contact as presented in Figure 3.1. The channel length (L) and channel width (W) are respectively 50 μm and 1000 μm. The substrates used are silicon wafer.

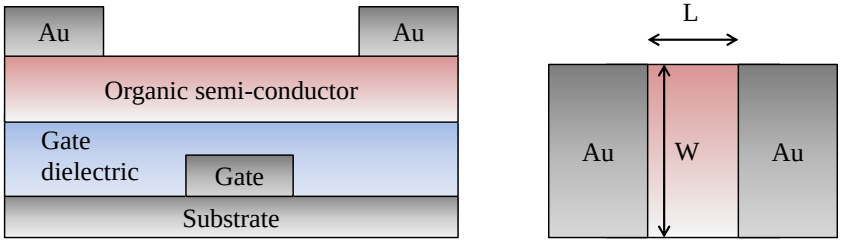

Figure 3.1: P-type bottom-gate, top-contact OTFT device architecture from a side-view (left) and from a top-view (right). L represents the channel length and W the channel width.

A layer of poly(1-vinyl-1,2,4-triazole) (PVT) is used as a dielectric. The PVT solution is prepared by dissolving PVT in ultra-pure water at a concentration of 7 weight%. The solution is filtered and spin-cast at 700 rpm for 60 seconds. The substrates are further dried at 85 °C for 120 min under a primary vacuum. The organic semiconductor materials to study are deposited on top of the dielectric. The deposition of the metals is performed by thermal evaporation. For p-type OTFTs, the electrode is gold. For n-type OTFTs, the electrode is aluminum.

The electrical characterizations are performed in a glovebox environment using a probe station (SUSS Microtec). Micro probes are used to take the contacts. A Labview controlled Keithley 4200 SMU was used for the acquisition of the electrical characteristics. A V_{DS} of +5 V is applied for n-type OTFTs and a V_{DS} of -5 V is applied for p-type OTFTs.

The mobility is extracted from the saturation regime where $|V_{DS}| > |V_{GS}\text{-}\ V_{th}| > 0$.

In the saturation regime, the current is given by:

$$I_{DS} = \frac{\mu C_i W}{2L}(V_{GS} - V_{th})^2 \tag{3.3}$$

and the carrier field effect mobility is given by:

$$\mu_{sat} = \frac{2L}{C_i W}(\frac{\partial\sqrt{I_{DS}}}{\partial V_{GS}})^2 \tag{3.4}$$

where V_{th} is the threshold voltage, C_i the gate dielectric capacitance per unit area (=14.7 nF/cm^2), μ_{sat} the mobility, W the channel width and L the channel length.

V_{th} can be extracted from measurements in the saturation region by plotting $\sqrt{I_{DS}}$ versus V_{GS} and extrapolating to $I_{DS} = 0$ [226].

3.2.2 Mobility measurement in single diode configuration

In the field of organic semiconductors, the extraction of the mobility using the space charge limited current (SCLC) has emerged as a common method to extract the charge mobility of materials [110]. The SCLC method is applied for single charge carrier devices, so called hole only devices or electron only devices. The example of hole only devices is taken to describe the electrical characteristics of a single charge carrier diode. In hole only devices, holes are injected in abundance by one of the electrode. These charge carriers are not compensated by an equal density of electrons and build up in the semiconductor: a positive space charge is formed in the semiconductor. Further increase of the voltage leads to the space-charge limited current, which is the maximum current that the semiconductor can sustain. Above a certain voltage, the current shows a quadratic behavior and the current density J can be characterized by the Child's law (also called Mott-Gurney law):

$$J = \frac{9}{8}\epsilon_r \epsilon_0 \mu \frac{V^2}{L^3} \tag{3.5}$$

where ϵ_0 is the permittivity of the vacuum, ϵ_r the dielectric constant of the polymer (assumed to be 3, which is a commonly used value for conjugated polymers), μ the mobility, V the voltage drop across the device and L the thickness of the material under study.

The previous equation assumes that the mobility is field independent. In order to consider a mobility that is field dependent, a modified equation is preferred (also called Murgatroyd equation, [137]) and J can be described by:

$$J = \frac{9}{8}\frac{\epsilon\epsilon_0\mu_0 V^2}{L^3} exp(0.89\sqrt{\frac{V}{E_0 L}}) \tag{3.6}$$

where μ_0 is the zero-field mobility and E_0 the characteristic field.

Single charge carrier devices are fabricated and further electrically characterized in order to extract the dark J-V curves. By fitting the J-V curves with the equations 3.5 or 5.2, the mobility can be extracted. In the early years, the Child's law was used to determine the mobility of single layers of materials such as (phenylene vinylene) derivatives [17, 137, 142], P3HT [203] and $PC_{61}BM$ [145]. Later, the use of the SCLC method has been broadened to the determination of single charge carrier mobility of a material blend in a BHJ configuration [143]. In order to assess the mobility of a single charge carrier of a material in a BHJ configuration, the other carrier has to be blocked. For example, for the study of hole mobility, hole only devices have to be fabricated with appropriate electrodes and electron blocking layer in order to inhibit the transport of electrons by the acceptor.

Hole only devices have been fabricated with the following configuration: ITO / MoO_3 /Active layer/MoO_3/Ag (Figure 3.2). Clean ITO substrates were treated under O_2 plasma for 2 minutes. MoO_3 (7 nm) is evaporated on the ITO substrate under a secondary vacuum. The D/A solution is further deposited by spin-casting in a glovebox environment. Finally, MoO_3 (7 nm) and silver (70 nm) were thermally evaporated under a secondary vacuum (10^{-6} mbar) onto the active layer through a shadow mask.

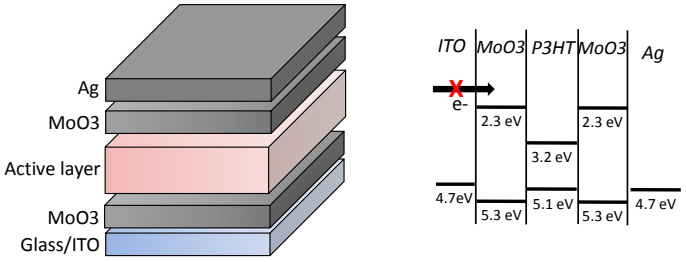

Figure 3.2: Hole only device structure.

3.3 Characterization of the BHJ morphology

3.3.1 UV-Vis absorption spectroscopy

UV-Vis spectra are recorded using a SAFAS UVMC^2 spectrophotometer at UB Lab and a Shimadzu UV-2501PC UV-Vis spectrophotometer at UW Lab.

3.3.2 X-ray diffraction measurements

The diffraction patterns obtained from the PDQT study were recorded at UB Lab using a Goniometer Pranatycal X'pert Pro.

The diffraction patterns obtained from the P3HT/PC_{61}BM study were recorded at UW Lab using a Bruker D8 advance diffractometer. The XRD measurements were performed in a reflection mode using Cu Kα1 radiation at 1.5406 Å.

The average size L of crystallites can be determined with the full width at half maximum of the diffraction peak using the Scherrer equation:

$$L = \frac{K\lambda}{\Delta cos(\theta)} \tag{3.7}$$

where K is the Scherrer's constant which depends on the crystallite shape and size distribution [112].

3.3.3 Atomic force microscopy

AFM images of PDQT were performed in UB Lab using a Veeco Dimension 3100.

AFM images of P3HT/PC_{61}BM-films were performed in UW Lab using a Dimension 3100 Scanning Probe Microscope.

3.3.4 Infrared absorption spectroscopy

PM-IRRAS spectra were recorded on a ThermoNicolet Nexus 670 FTIR spectrometer at a resolution of 4 cm^{-1}, by coadding several blocks of 1500 scans (30 minutes acquisition time). Experiments were performed at an incidence angle of 75 °using an external

homemade goniometer reflection attachment, adding a ZnSe photoelastic modulator (PEM, Hinds Instruments, type III) after the polarizer [25].

The ATR spectra of the additives were recorded with a ThermoNicolet Nexus 670 FTIR spectrometer equipped with a liquid nitrogen cooled narrow-band mercury cadmium telluride (MCT) detector using a Silver-Gate (diamond crystal) ATR accessory (Specac). Each spectrum was obtained from the acquisition of 100 scans at a resolution of 4 cm^{-1}.

3.4 Photo-stability tests

Photo-degradation tests were carried out with white light provided by a 300 W halogen lamp. The distance between the lamp and the device was adjusted so that the light intensity was 100 $mW.cm^{-2}$. The temperature is kept below 32 °C throughout the experiment using a fan to cool down the OSCs subject to light irradiation. The temperature of the OSCs were monitored with a k-type thermocouple and an Omega panel monitor. All OSCs were kept in inert conditions during light-irradiation and were placed in air during the measurements of the *J-V* characteristics.

Chapter 4

Determination of selection rules for processing additives

This work has been published in AdvenMat, 4 (3) 1-9, 2013. It has been adapted with permission from the publisher under license number 3479061354313.

As noted in Chapter 2, processing additives have been widely used for increasing the efficiency of OSCs. However, very few studies have addressed the critical question of how to identify or select processing additives from the vast array of available solvents. In this chapter, guidelines for the selection of processing additives are developed for P3HT/PC_{61}BM-based OSCs.

First, the properties of existing processing additives reported in the literature are analyzed. The novelty of the developed approach is to use the theory of the Hansen solubility parameters to analyze these processing additives. This theory is commonly used in the coating and chemical formulation industries to determine the solubility of compounds. Nevertheless, its use in the area of BHJ started only very recently and has so far been limited to the identification host solvents [161, 214], or to correlate the host solvent solubility properties with the active layer morphology [57] and with the performance of OSCs [136]. Here, the Hansen solubility parameters are used to define the interactions between solvent, processing additives and active materials.

4.1 The Hansen solubility parameters as a method for selecting processing additives

The solubility parameter (δ), first used by Hildebrand and Scott, was originally defined as the square root of the cohesive energy density (E_C) over the molar volume of the pure solvent (V):

$$\delta = \sqrt{\frac{E_c}{V}} \tag{4.1}$$

The Hansen theory is based on substituting the total cohesive energy by three components; E_D, E_P and E_H which describe the energy involved in three principal types of interactions, respectively: (i) dispersion interactions, (ii) permanent dipolar - permanent dipolar molecular interactions and (iii) hydrogen bonding interactions [73]. The parameter δ can therefore be similarly substituted by three components that describe these three interactions:

$$E_C = E_D + E_P + E_H \tag{4.2}$$

$$\delta^2 = \delta_D^2 + \delta_P^2 + \delta_H^2 \tag{4.3}$$

Where δ_D, δ_P and δ_H are the Hansen solubility parameters (HSPs). Graphically, every chemical compound can be represented by its position in a 3D space, the Hansen solubility space, with coordinates defined by the three solubility parameters. The solubility of a solute in a solvent is predicted from similarities in their interactions. Such similarity is quantified by the distance R_A between the HSPs of the solvent (δ_{D1}, δ_{P1} and δ_{H1}) and the HSPs of the solute (δ_{D2}, δ_{P2} and δ_{H2}). The distance R_A between them is calculated using the following equation:

$$R_A^2 = 4(\delta_{D1} - \delta_{D2})^2 + (\delta_{P1} - \delta_{P2})^2 + (\delta_{H1} - \delta_{H2})^2 \tag{4.4}$$

In addition to δ_{D2}, δ_{P2} and δ_{H2}, a solute requires a boundary of solubility to define and differentiate between "sufficient" and "non-sufficient" interactions from a solubility standpoint. Therefore a solute is described as a sphere in the Hansen solubility space, the HSPs are the centre of the sphere and R_O is the radius representing the boundary of solubility. The interactions between a solvent and a solute are considered to be strong only if the distance R_A is smaller than the radius of the sphere R_O. The relative energy difference (RED) can be used as a numerical parameter to compare R_A and R_O, and is defined as:

$$RED = R_A/R_O \tag{4.5}$$

If the RED is higher than 1, the solvent is outside the solubility sphere of the solute and can be expected to be a bad solvent. On the other hand, if the RED is between 0 and 1, the solvent is inside the solubility sphere of the solute and is expected to be a good solvent. The HSPs of a wide range of solvents can be found in reference textbooks [73]. They have been calculated using either equations of state derived from statistical thermodynamics or using the group contribution method. The group contribution method predicts the HSPs of a compound by adding the solubility parameters of all the contributing chemical groups or atoms. For a new solute, the HSPs can be also determined experimentally by performing solubility tests. The solute is mixed with a wide range of solvents with different known HSPs. The quality of interactions is scored for each solute-solvent combination. The results are recorded on the Hansen solubility space and are fitted to a sphere with all the good solvents inside the sphere and the poor solvents outside. The HSPs of the compound result from the fitting of

the sphere. Figure 4.1 depicts the process of sphere fitting using the software HSPiP 3rd edition.

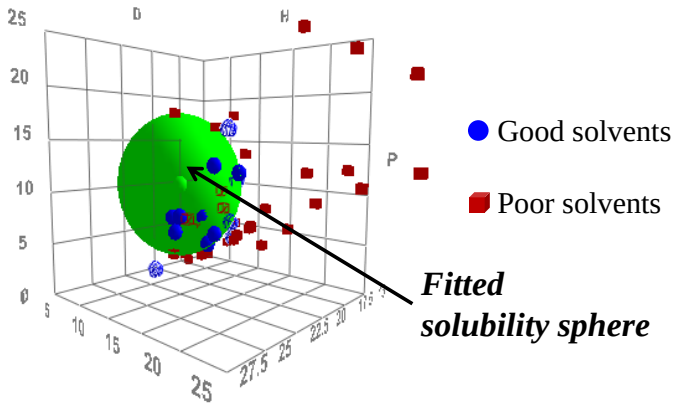

Figure 4.1: HSPs diagrams showing the good and the poor solvents resulting from solubility tests and the fitted solubility sphere of the compound under study.

4.2 Determination of the HSPs of P3HT and $PC_{61}BM$.

The HSPs of P3HT and $PC_{61}BM$ were already determined by other groups [57, 63, 135, 136]. By comparing the results, it was found that the values can vary depending on the specific material characteristics (molecular weight and polydispersity of the polymer) and the method used in the solubility tests. Therefore, instead of using HSP values extracted from the literature, the HSPs of P3HT and $PC_{61}BM$ are determined experimentally. The HSPs were determined by performing solubility tests in which the materials are mixed with various solvents that cover the whole range of the Hansen solubility space. Fifty-four solvents and around ten solvent mixtures were used. In each test, 4 mg of material is diluted in 2 mL of each solvent to obtain a concentration of 2 $mg.mL^{-1}$. Each solution is stirred overnight at room temperature. The quality of solubility is assessed by visual inspection and assigned a score of 1 for good solubility or 0 for poor solubility, depending on whether or not a solid residue can still be detected after the stirring step. These results are used to fit the solubility sphere of the material where all the good solvents (the ones scored 1) are inside the sphere and the bad solvents (the ones scored 0) are outside the sphere. As the data fitting may contain false negative and false positive errors (i.e bad solvents inside the solubility sphere and good solvents outside the solubility sphere, respectively), the fitting accuracy needs to be estimated. This is usually estimated using a quality of fit function of the form:

$$DATA\ FIT = (A_1 * A_2 * \ldots * A_n)^{1/n} \tag{4.6}$$

where n is the number of solvents used for the solubility tests and A_i is given by:

$$A_i = e^{-(Error\ distance_i)} \tag{4.7}$$

The *Error distance*$_i$ represents the distance of the false positive and false negative solvents from the sphere boundary. The DATA FIT reaches 1 for an ideal fit without any erroneous solvents. The results of the fitting are summarized in Table 4.1. Figure 4.2 depicts the solubility spheres of P3HT and $PC_{61}BM$.

Table 4.1: HSPs of P3HT and $PC_{61}BM$.

Materials	HSP[$MPA^{1/2}$]				Fit	Errors	
	δD	δP	δH	R_o		False negative	False positive
P3HT	19.05	3.3	2.8	3.9	0.95[a]	2/64[b]	1/64[c]
$PC_{61}BM$	20.02	5.2	5.88	8.4	0.97[a]	2/65[b]	0/65[c]

[a] As determined by the HSPiP software using Equation 4.6.

[b] Number of bad solvents inside the solubility sphere.

[c] Number of good solvents outside the solubility sphere.

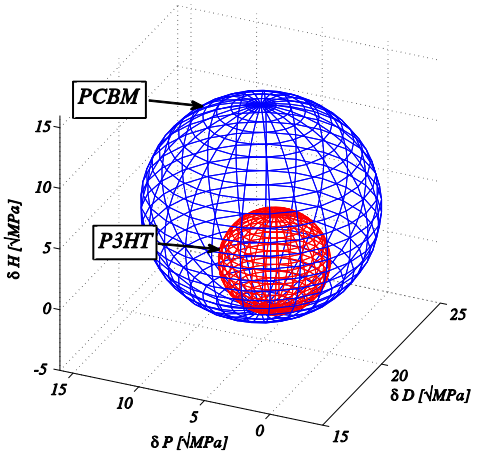

Figure 4.2: Solubility spheres of P3HT and $PC_{61}BM$.

4.3 HSPs of commonly used processing additives

Next, the solubility properties of some processing additives reported to improve the efficiency for P3HT/PC_{61}BM-based OSCs in the literature are examined: ODT, 1,6-hexanedithiol, 1,12-dodecanedithiol, di(ethylene glycol)-diethyl ether (DEGDE), n-methyl-2-pyrrolidinone (NMP) and 4-bromoanisole. With the exception of 4-bromoanisole, which HSPs need to be calculated using the group contribution method, the HSPs of all these processing additives can be obtained from the database supplied by Hansen et al. [73]. After determining the HSPs of the processing additives and the active materials, the RED values are calculated using the equations described above. The results are shown in Table 4.2. For 4-bromoanisole, ODT, hexanedithiol and dodecanethiol, the RED values are found to be < 1 with PC_{61}BM and > 1 with P3HT. This is in agreement with the conclusions of Lee et al. that a processing additive should be a good solvent of PC_{61}BM and a poor solvent of P3HT. In contrast, NMP and DEGDE exhibit RED values with PC_{61}BM that are close to 1. The solubility of PC_{61}BM in NMP and DEGDE is reported to be low ($\sim$0.3 mg.mL^{-1}[234]) which may explain their higher RED values. It is also noteworthy to point that DEGDE and NMP seem less effective in improving the efficiency of OSCs in comparison to the other processing additives (PCE: 1.5 % in case of NMP or DEGDE versus 2.6 - 4.0% with the other processing additives) [130, 159, 182]. The observation that can be made from this study is that efficient processing additives possess RED values with PC_{61}BM clearly below 1 and RED values with P3HT above 1. This indicates the effectiveness of using the HSPs as a tool to predict novel processing additives for P3HT/PC_{61}BM-based OSCs.

4.4 Identification of novel processing additives

Based on the RED values above, the criteria that need to be satisfied by a processing additive for P3HT/PC_{61}BM-based OSCs are defined as follows: RED with PC_{61}BM < 0.9, RED with P3HT > 1.0 and boiling point 100 °C higher than that of the host solvent. The RED with PC_{61}BM is set to < 0.9 instead of < 1 in order to ensure selecting solvents in which PC_{61}BM solubility is sufficiently high. The third criterion is based on the general requirement that the boiling point of the processing additive must be higher than that of the host solvent, which in this case is ODCB (boiling point = 180 °C). A processing additive with a boiling point 100 °C higher provides a sufficient latitude for differential evaporation of the two solvents. Additionally, for

Table 4.2: Characteristics of processing additives: HSPs, RED with P3HT and $PC_{61}BM$, reported PCEs.

Materials	HSPs [$MPa^{1/2}$]				RED with		PCEs [%]	
	δD	δP	δH	R_o	P3HT	$PC_{61}BM$	without additive	with additive
P3HT	19.05	3.3	2.8	3.9	ND	ND		
$PC_{61}BM$	20.02	5.2	5.88	8.4	ND	ND		
DEGDE	15.8	4.7	4.4		1.75	1.02	0.29%	5 times higher[a)] [27]
NMP	18	12.3	7.2		2.62	0.99	0.29%	5 times higher[a)] [27]
4-Bromoanisole	19.8	7.7	7		1.61	0.33	1.65%	2.60%[32]
ODT	17.4	7.3	5.2		1.47	0.68	0.46%	3.12%[19]
Hexanedithiol	17.4	7.6	6.4		1.67	0.69	0.46%	3.16%[19]
Dodecanethiol	17.3	5.7	4.1		1.14	0.68	1.74%	4.03%[26]

[a)] No exact PCE is reported

safety concerns, only solvents that are not carcinogenic are considered. Applying the above selection criteria on an array of 723 solvents with known HSPs that are present in the Hansen software database (HSPiP 3rd edition), three solvents were shown to satisfy the requirements. These are 1-cyclohexyl-2-pyrrolidinone (C-PYR), dimethyl phthalate (DPH) and tributyl *o*-acetylcitrate (TRIB). The molecular structures of the selected solvents are presented in Figure 4.3. As shown in Table 4.3 , they all have REDs with $PC_{61}BM < 0.9$ and REDs with P3HT > 1.0. Graphically, these three solvents are positioned inside the solubility sphere of $PC_{61}BM$ and outside the sphere of P3HT, as depicted in Figure 4.4.

Table 4.3: Characteristics of processing additives: HSPs, *REDs* with P3HT and $PC_{61}BM$ and boiling points.

Solvents	HSPs [$MPa^{1/2}$]			RED with		Boiling point
	δD	δP	δH	P3HT	$PC_{61}BM$	
C-PYR	18.2	6.8	6.5	1.38	0.48	306 ^{o}C
DPH	18.6	10.8	4.9	2.01	0.76	284 ^{o}C
TRIB	16.7	2.5	7.4	1.70	0.87	388 ^{o}C

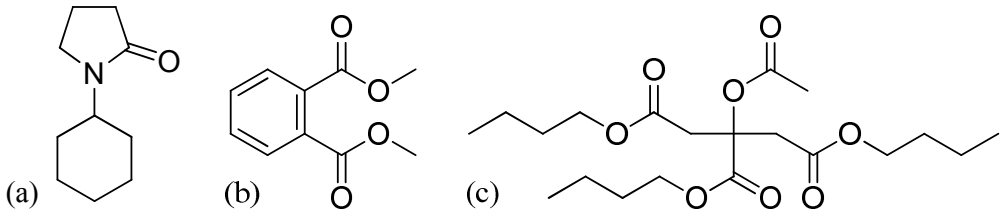

Figure 4.3: Molecular structures of: (a) C-PYR, (b) DPH and (c) TRIB.

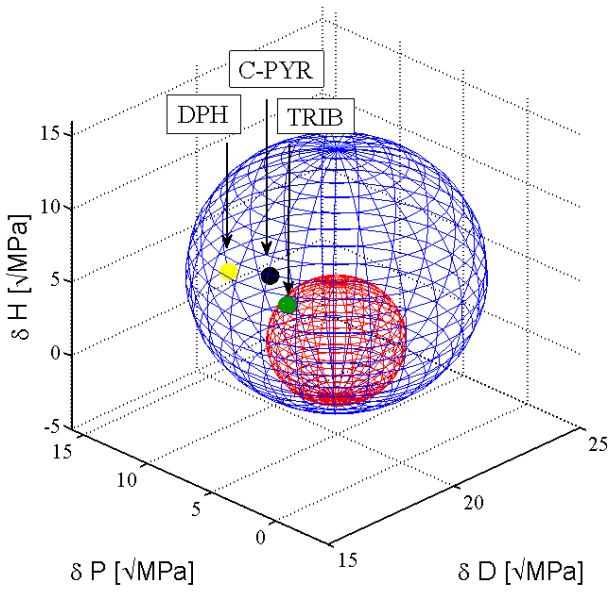

Figure 4.4: Positions of C-PYR, DPH and TRIB in the Hansen solubility space with respect to the solubility spheres of P3HT and $PC_{61}BM$.

For verification, the solubilities of $PC_{61}BM$ and P3HT in these solvents are experimentally tested. P3HT was dissolved in processing additives with a concentration below 0.002 mg.mL^{-1}. For the specific case of DPH, P3HT was observed to float above the solvent, clearly indicating its non-solubility. For C-PYR and TRIB, UV-Vis absorption spectra of the solutions were measured and compared to the spectrum of a solution of P3HT in ODCB (concentration of 0.03 mg.mL^{-1}) where the polymer is expected to be fully solubilized. The UV-Vis absorption spectra of P3HT in ODCB showed a unique absorption peak at 465 nm whereas the UV-Vis absorption spectra of P3HT in C-PYR and TRIB both showed a broad absorption peak extending beyond 650 nm indicating the presence of P3HT aggregates. The UV-Vis spectra are shown in Figure 4.5. These results indicate that P3HT is not soluble at a concentration of 0.002 mg.mL^{-1} in C-PYR and TRIB.

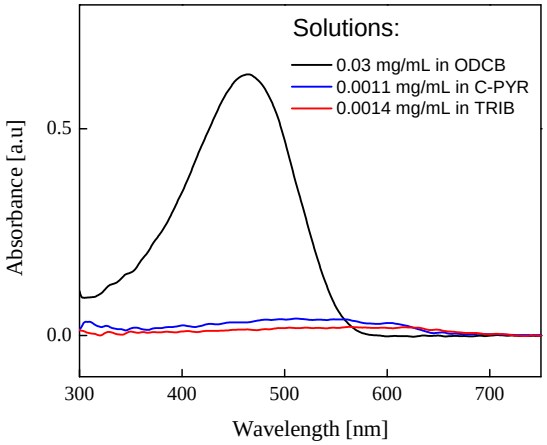

Figure 4.5: UV-Vis absorption spectra of solutions of P3HT in ODCB, C-PYR and TRIB.

Several solutions of $PC_{61}BM$ in CB were prepared in various concentrations ranging from 0.01 mg.mL^{-1} to 0.042 mg.mL^{-1}. The UV-Vis absorption was measured for each of the solutions in order to trace a calibration curve (Figure 4.6). The calibration curve enables the estimation of the concentration of $PC_{61}BM$ in any solution based on optical absorbance data.

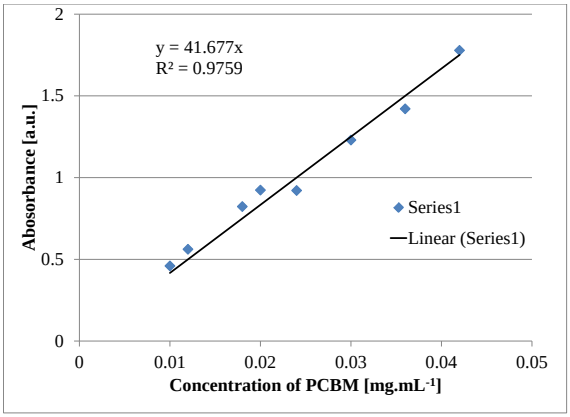

Figure 4.6: Calibration curves obtained from dissolving $PC_{61}BM$ in CB with different concentrations.

Over-saturated solutions of $PC_{61}BM$ in C-PYR, DPH and TRIB were prepared and stirred overnight at 50 ^{o}C. After a centrifugation step (7000 rpm for 10 min), the supernatants were removed, transferred and further diluted. The supernatants were diluted 1600 to 2000 times for solutions of C-PYR, 80 to 200 times for DPH and 30 to 40 times for TRIB. The absorbance maxima in the UV-Vis spectra of these diluted

solutions were measured and the concentrations of initial solutions were determined using the calibration curve. The solubility limits of $PC_{61}BM$ in the three solvents are listed in Table 4.4.

Table 4.4: Solubility of P3HT and $PC_{61}BM$.

Solvents	Solubility limits [mg.mL^{-1}]	
	P3HT	$PC_{61}BM$
C-PYR	<0.002	31.4
DPH	<0.002	2.2
TRIB	<0.002	0.4

The test results in Table 4.4 confirmed the solubility of $PC_{61}BM$ and the poor solubility of P3HT in the three solvents. Also, it is noteworthy to mention that the values of the solubility limits appear to be consistent with the trend in the RED values reported in Table 4.3: C-PYR, which exhibited the smallest RED, with $PC_{61}BM$ appears to be the best solvent while TRIB, which exhibited the highest RED with $PC_{61}BM$, demonstrates the lowest solubility. The RED values appear to be efficient in predicting the solubility of organic semiconductors in solvents.

Next, to investigate the influence of C-PYR, DPH and TRIB as processing additives on P3HT/$PC_{61}BM$-BHJ morphology, UV-Vis absorption measurements were carried out on a series of P3HT/$PC_{61}BM$ films. The films were fabricated by spin-casting solutions of P3HT/$PC_{61}BM$ in ODCB that contain a processing additive in one of the following concentrations (by volume): 0.4 vol%, 0.8 vol%, 1.2 vol%and 1.6 vol%. The UV-Vis absorption spectra obtained are displayed in Figure 4.7. For each processing additive, the spectra show an increase in the main P3HT absorption peak (at 520 nm) and the appearance of vibronic bands at 550 nm and 600 nm. The appearance of these bands is indicative of an increase in P3HT crystallinity [238]. Similar bands are known to appear when P3HT/$PC_{61}BM$ films are treated by thermal annealing, or solvent annealing. These results suggest that the three processing additives increase P3HT crystallinity and may, therefore, increase the efficiency of OSCs.

To study their effect on the photovoltaic performance, a series of OSCs utilizing formulations that contain various concentrations of these three processing additives are fabricated and tested. For comparison, OSCs utilizing ODT are also fabricated and tested because it is a widely used processing additive known to improve the PCE of P3HT/$PC_{61}BM$-based OSCs. The J-V characteristics of the OSCs are measured using

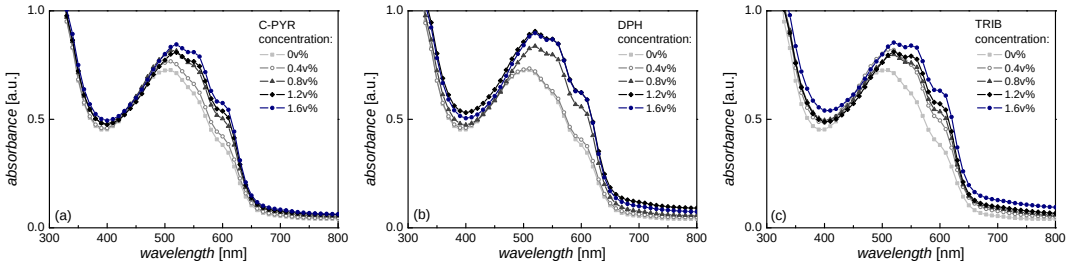

(a) (b) (c)

Figure 4.7: Solid state UV-Vis absorption spectra for P3HT/$PC_{61}BM$ blends with varying concentration of processing additives: a) C-PYR, b) DPH and c) TRIB.

a solar simulator with AM1.5G filters set at 100 mW/cm^2. Figure 4.8 shows the photovoltaic parameters (V_{oc}, FF, J_{sc} and PCE) of the OSCs with the different processing additives and their corresponding concentrations. The data in the figures represents the average values obtained from measurements on eight to twelve individual OSCs for each system. The best values for each system are recorded in Table 4.5.

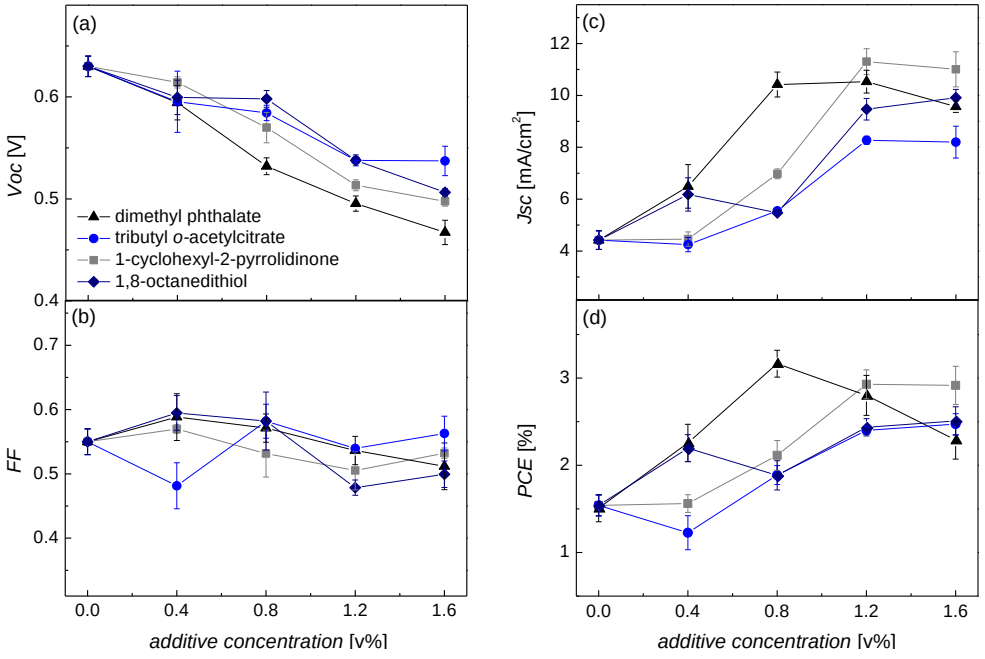

Figure 4.8: Photovoltaic parameters of OSCs with varying concentration of processing additives: (a) V_{oc}, (b) FF, (c) J_{sc} and (d) PCE.

DPH and C-PYR increase the PCE by respectively 113% and 93% in comparison to control devices devoid of processing additives and any post processing step, resulting in a PCE of 3.2% in case of DPH (at a concentration of 0.8 vol%) and 2.9% in case of C-PYR (at a concentration of 1.6 vol%) (Table 4.5). At a concentration of 1.6

Table 4.5: Photovoltaic properties of OSCs. For each processing additive, the table shows the photovoltaic properties of OSCs containing the processing additive at a concentration giving the best PCE.

Processing additive	Concentration	V_{oc} [V]	FF	J_{sc} [mA.cm^{-2}]	PCE [%]
No additive		0.63 ±0.01	0.55 ±0.02	4.4 ±0.4	1.5 ±0.1
C-PYR	1.6 vol%	0.50 ±0.01	0.53 ±0.01	11.0 ±0.7	2.9 ±0.2
DPH	0.8 vol%	0.53 ±0.01	0.57 ±0.02	10.4 ±0.5	3.2 ±0.2
TRIB	1.6 vol%	0.54 ±0.01	0.56 ±0.03	8.2 ±0.6	2.5 ±0.1
ODT	1.6 vol%	0.51 ±0.00	0.50 ±0.02	9.9 ±0.3	2.5 ±0.2

vol%, the OSCs with ODT and TRIB exhibit efficiencies of 2.5% corresponding to an increase of 67%. The PCE of a control OSC is 1.5% and is in par with what is generally obtained for OSCs fabricated without any thermal or solvent annealing [29, 230]. The main parameter responsible for the increase in PCE is the J_{sc} which is found to increase significantly on increasing the concentrations for C-PYR, TRIB and ODT. The increase in PCE is, on the other hand, somewhat limited by the negative impact of the processing additives on the V_{oc} which is observed to decrease as the concentration of the processing additive increases. This change in V_{oc} is commonly observed for OSCs undergoing solvent annealing or thermal annealing processes [116, 117]. Chen et al. showed that the introduction of ODT in a P3HT/$PC_{61}BM$ blend increased the crystallinity of P3HT and caused the interlayer spacing between P3HT chains to be shorter [37]. The decrease in V_{oc} observed with ODT and the other processing additives may be attributed to the increase in P3HT crystallinity, together with the reduction of the interlayer spacing of P3HT which can induce a reduction of the band gap [39]. As a result, the difference between the LUMO of $PC_{61}BM$ and the HOMO of P3HT becomes somewhat smaller, causing a decrease in V_{oc} [185]. Clearly, all three additives produce similar trends in terms of their effects on OSC parameters; not unlike those produced by ODT and all lead to significant improvements in the PCE. The results therefore show that the use of HSPs and the specific selection criteria that were defined are indeed successful in screening and identifying processing additives that are capable of improving the performance of BHJ-OSCs.

4.5 Conclusion

In conclusion, the HSPs are shown to be efficient in guiding the selection of processing additives for P3HT/PC_{61}BM-OSCs. Using selection criteria based on the HSPs, three novel processing additives for the P3HT/PC_{61}BM system have been identified: C-PYR, DPH and TRIB. Through the developed approach, the number of suitable processing additives that can be investigated could be significantly increased. Also, it provides a methodological approach based on the solubility parameters of the active materials and the solvents for selecting processing additives.

Chapter 5

The influence of processing additives on the formation of the bulk heterojunction

This chapter focuses on elucidating the mechanistic effects of processing additives on the formation of the BHJ. To verify the universal aspect of the study, three processing additives of significantly different molecular structures are investigated: C-PYR, DPH and ODT. Optical, structural and electrical characterizations are conducted to understand the effects of processing additives on the formation of the BHJ during spin-casting. Using the results of these characterizations, a general mechanism that explains the role of additive in optimizing the BHJ morphology is proposed.

5.1 Effects of processing additives on the efficiency of OSCs

First, the effects of processing additive concentration on the electrical parameters of the OSCs are studied. A series of OSCs utilizing formulations that contain various concentrations of the three processing additives (from 0 vol% to 4 vol%) in ODCB is fabricated. The *J-V* characteristics of the OSCs are measured using a solar simulator with AM1.5G filters set at 100 mW.cm^{-2}. Figure 5.1 shows the photovoltaic parameters V_{oc}, FF, J_{sc} and PCE of the OSCs with the different processing additives and their corresponding concentrations. The data in the figures represent the average values obtained from six individual OSCs for each system.

The V_{oc} decreases with increasing concentration of processing additive. This loss in V_{oc} is particularly pronounced in the case of the DPH. OSCs with 4 vol% of DPH have an average V_{oc} of 0.44 V which represents a loss of 0.23 V compared to the V_{oc} of OSCs without any processing additive. At a concentration of 4 vol%, C-PYR and ODT demonstrate a loss of only 0.15 V. As already mentioned in the previous chapter, this change in V_{oc} is attributed to an increased crystallinity in P3HT which induces a reduction of the band gap. Therefore, this suggests that processing additives increase the crystallinity of P3HT in the BHJ.

Regarding the J_{sc} and the FF, two regimes are observed: increasing the processing additive concentration first causes an increase in the J_{sc} and the FF until an optimum concentration is reached. A further increase in the concentration leads to a deterioration in these electrical parameters, which is particularly pronounced in the case of DPH: from an optimum J_{sc} of 8.5 mA.cm^{-2}, the J_{sc} drops to 7.2 mA.cm^{-2} when the additive concentration reaches 4 vol%.

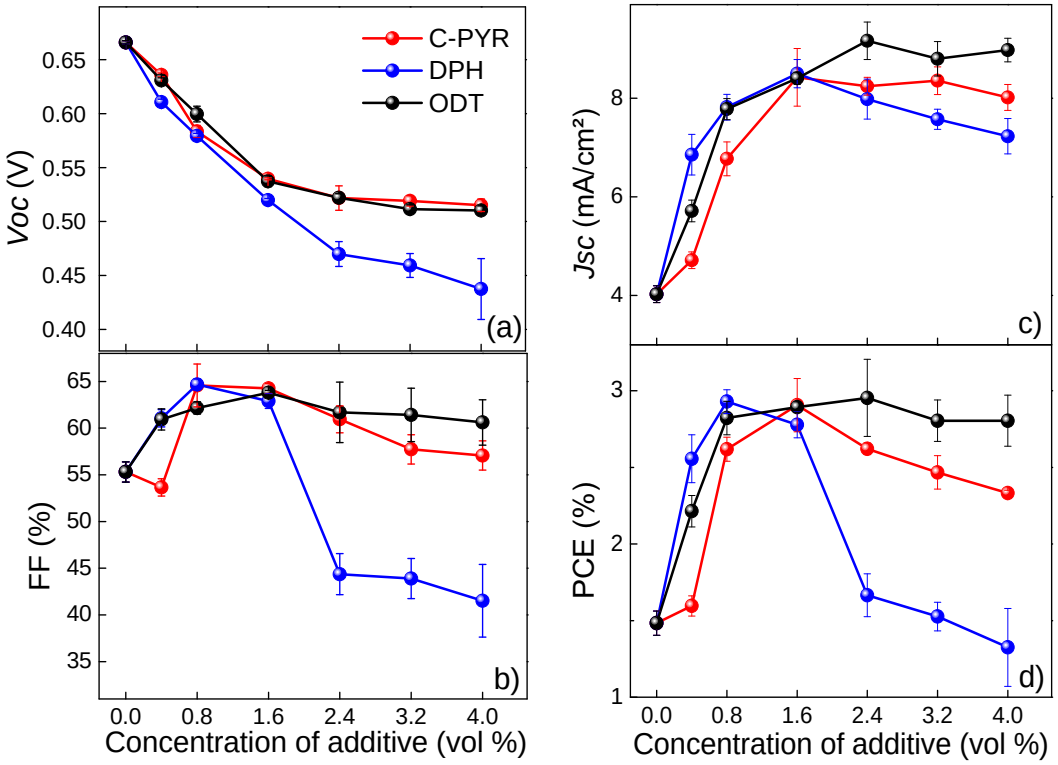

Figure 5.1: Electrical parameters of OSCs with different concentrations for the three processing additives: a) V_{oc}, b) FF, c) J_{sc} and d) PCE.

Overall, the value of the PCE reflects the evolution of the FF. The maximum PCEs are 2.9% for both C-PYR and DPH and 3.0% for ODT.

5.2 Characterizations of films prepared from processing additive

5.2.1 UV-Vis absorption spectroscopy

In order to gain insights into the effects of processing additives on the crystallinity of P3HT, UV-Vis absorption spectroscopy was carried out on a series of P3HT/$PC_{61}BM$-films spin-cast from a solution with varying additive concentrations. The UV-Vis spectra of films prepared with processing additives are presented in Figure 5.2.

In these spectra, the absorption band of P3HT increases on increasing processing additive concentration and the vibronic bands of P3HT at 556 nm and 605 nm become

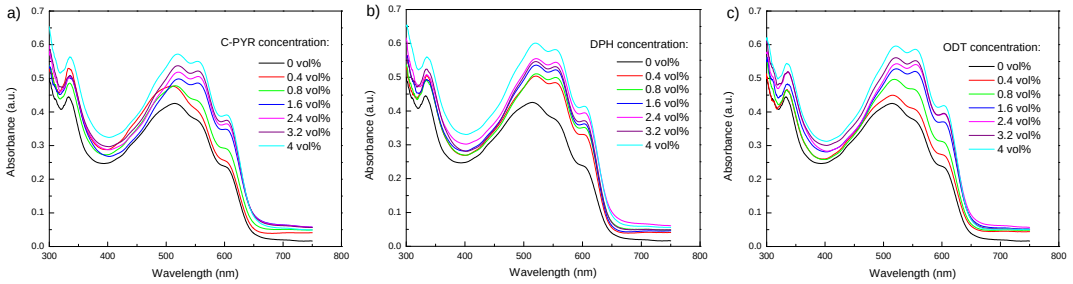

Figure 5.2: Solid state UV-Vis absorption spectra for P3HT/$PC_{61}BM$ blends with various concentration of a) C-PYR, b) DPH and c) ODT.

more intense. These changes in P3HT absorption spectra suggest that the introduction of processing additive in the solvent mixture increases the crystallinity of P3HT in the BHJ, which is in agreement with the V_{oc} trends observed in Figure 5.1 .

5.2.2 XRD measurements

In order to further investigate the effects of the processing additives on the crystallinity of P3HT, X-ray diffraction (XRD) measurements were conducted on P3HT/$PC_{61}BM$ films. Figure 5.3 depicts the XRD patterns of P3HT/$PC_{61}BM$ films with different concentrations of the three processing additives.

The diffraction peak at 5.5° corresponds to the edge-on orientation of the polymer chains [238]. The intensity of the diffraction peak at 5.5° decreases when processing additives are introduced in the solution blend. This result is consistent with earlier observations by Guo et al. who showed that introducing processing additives into a blend of P3HT/indene-C70 bisadduct ($IC_{70}BA$) leads to a decrease in the P3HT diffraction peak [70]. They attributed this result to a decrease in phase separation. The average domain sizes of P3HT can be estimated using the Scherrer equation:

$$L = \frac{K\lambda}{\Delta cos(\theta)} \tag{5.1}$$

Where L is the average crystallite size of P3HT (1 0 0) plane, λ is the wavelength of the X-ray ($\lambda = 0.154$ nm), Δ is the full width at half maximum (FWHM) of the diffraction peak, θ is the diffraction angle and K the Scherrer's constant. Using this equation, the FWHM can be correlated to the size of P3HT crystallites. Table 5.1 displays the values of the FWHM for all the films.

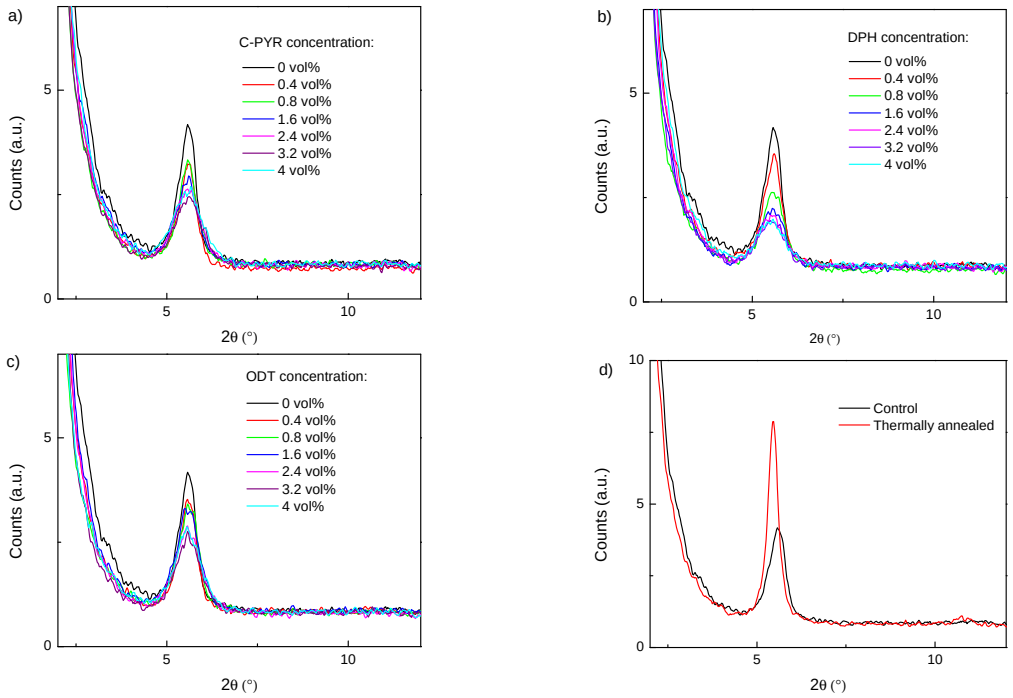

Figure 5.3: XRD patterns of P3HT/PC_{61}BM fims spin-cast from solutions containing 1.6 vol% of a) C-PYR, b) DPH, c) ODT and d) thermally-annealed film.

Table 5.1: Values of the FWHM of P3HT diffraction peak at 5.5° for different active layer compositions.

Type of	FWHM (°)						
Processing	0 vol %	0.4 vol%	0.8 vol%	1.6 vol%	2.4 vol%	3.2 vol%	4 vol%
C-PYR	0.49	0.42	0.49	0.61	0.71	0.79	0.81
DPH	0.49	0.51	0.58	0.61	0.77	0.65	0.71
ODT	0.49	0.51	0.6	0.63	0.64	0.72	0.71
Thermally annealed	0.32						

As shown in Table 5.1, the values of the FWHM of the diffraction peak at 5.5° increase with increasing concentration of processing additives. According to Equation 5.1, the domain size is inversely proportional to the FWHM. Therefore, the increase in FWHM suggests that the introduction of processing additives leads to smaller domains of P3HT crystallites. The average crystallites sizes can be assessed using equation 5.1, providing that the value of K is known which value depends on the crystallite shape and the crystallite-size distribution [112]. The determination of K in a BHJ configuration is beyond the scope of this work but an approximation of the crystallite sizes can nevertheless be assessed. Figure 5.4 depicts the evolution of crystallite sizes as calculated

with equation 5.1 using 0.9 for the value of K (considering crystalline domains as being spherical). The results clearly show that P3HT crystallites decrease with increasing concentration of processing additives.

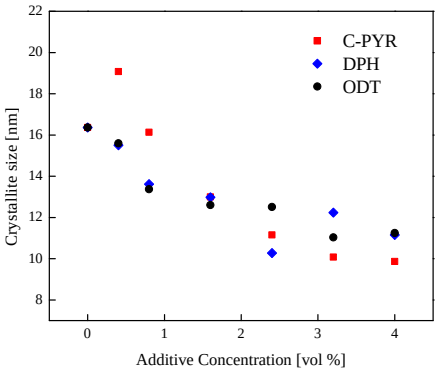

Figure 5.4: Average size of P3HT crystallites as a function of processing additive concentration.

As a comparison, XRD measurements were also conducted on a film of P3HT/$PC_{61}BM$ which was thermally annealed at 110 °C for 15 min (Figure 5.3d). In this case, the diffraction peak of P3HT becomes narrower (FWHM=0.32°) which implies that the P3HT domain sizes increase after thermal annealing. This shows that the BHJ morphology of a thermally annealed P3HT/$PC_{61}BM$ film is fundamentally different from that obtained with processing additives, despite the fact these two methods increase the PCE of OSCs in a similar manner. When a thermal annealing is performed, the domain sizes of P3HT crystallites increase whereas when processing additives are used, the domains sizes of P3HT crystallites decrease.

The previous results in UV-Vis absorption spectroscopy and the trend in V_{oc} suggest that processing additives increase crystallinity of P3HT in the BHJ. The increased crystallinity can be due to two factors: either an increasing crystallite domain sizes and/or an increasing number of crystallite domains. Since the XRD measurements show that the size of the crystallite domains decreases, it is clear that the introduction of processing additives contribute to generate more crystallites of P3HT and smaller in size.

The question that is naturally arising now is whether the processing additives have a direct effect on P3HT crystallinity or they have an effect on $PC_{61}BM$ and the observed crystallinity change in P3HT is a consequence of it. To address this question, XRD measurements were performed on films of sole P3HT spin-cast from solutions with various concentrations of processing additive, in this case DPH. The XRD patterns of

P3HT-films, depicted in Figure 5.5, show that the introduction of DPH decreases the intensity of the diffraction peak of P3HT, similar to that observed in P3HT/$PC_{61}BM$ films. This result indicates that processing additives have a direct effect on the crystallinity of P3HT by generating more numerous and smaller crystallites.

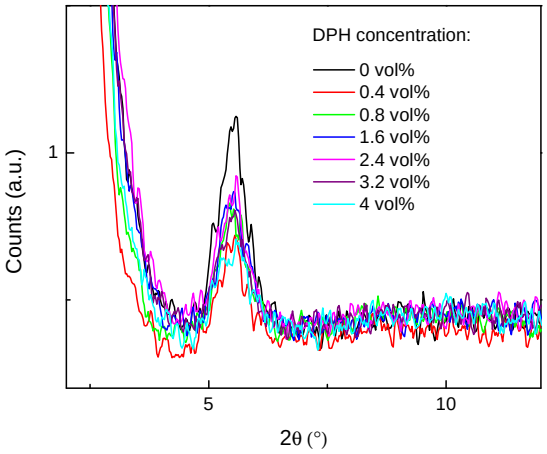

Figure 5.5: XRD patterns of P3HT films spin-cast from solutions containing various concentrations of DPH.

In order to determine how this structuring reflects on the transport of holes, the hole mobility across the BHJ is measured.

5.3 Hole mobility measurements

The hole mobility across the BHJ can be determined by using the standard Space Charge Limited Current (SCLC) method [53, 63, 116]. Single carrier devices, in this case hole-only devices, are fabricated using the following structure: ITO/MoO_3/active layer/MoO_3/silver. The device structure and the related energy diagram are depicted in Figure 5.6.

Above a certain voltage, the transport of holes in this device architecture becomes limited by the space charge that is formed. In this regime, the hole mobility can be extracted from the fitting of the J-V characteristics in the dark using the following equation:

$$J = \frac{9}{8}\frac{\epsilon\epsilon_0\mu_0 V^2}{L^3} exp(0.89\sqrt{\frac{V}{E_0 L}}) \tag{5.2}$$

where ϵ_0 is the permittivity of the vacuum, ϵ_r is the dielectric constant of the polymer (assumed to be 3, which is a commonly used value for conjugated polymers), V is the

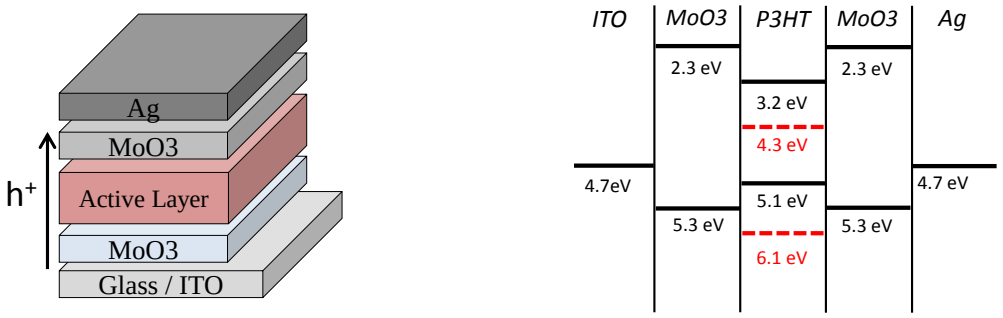

(a) (b)

Figure 5.6: (a) Device structure of hole-only device and (b) corresponding energy diagram.

voltage drop across the device, L the thickness of the material under study and where μ_0 is the mobility.

Hole-only devices are fabricated from active layers with various compositions. For each type of active layers, the thicknesses are measured using a profilometer. The thickness of the active layer devoid of processing additive is 101 nm and increases up to 121 nm, 135 nm and 113 nm for active layers prepared with 4 vol% of C-PYR, DPH and ODT respectively. To measure the J-V characteristics, a positive bias, defined as the ITO being at a more positive potential relative to the metal electrode, was used. Under such a bias, holes flow across the P3HT/PC_{61}BM layer and are collected by the MoO_3/Ag electrode. Therefore, the direction of hole transport in these hole-only devices is the same as in the operating mode of inverted OSCs devices. Figure 5.7 shows plots depicting $J.L^3$ as a function of the applied voltage from a series of hole-only devices fabricated from different types and concentrations of additive.

In order to extract the mobility, the J-V characteristics are fitted with Equation 5.2 for voltages ranging from around 2 to 5 V. The starting voltage is found to be appropriate for fitting around 2 V and slightly varies as a function of the composition of the active layer.

Figure 5.8 shows the evolution of the hole mobility as a function of the concentration of processing additive. The data in the figures represent the average values obtained from measurements on two to four individual hole-only devices for each material system.

The average hole mobility in a BHJ without processing additive is 1.4x10^{-4} cm^2.V^{-1}.s^{-1}. For the three processing additives, two regimes appear: the hole mobility increases

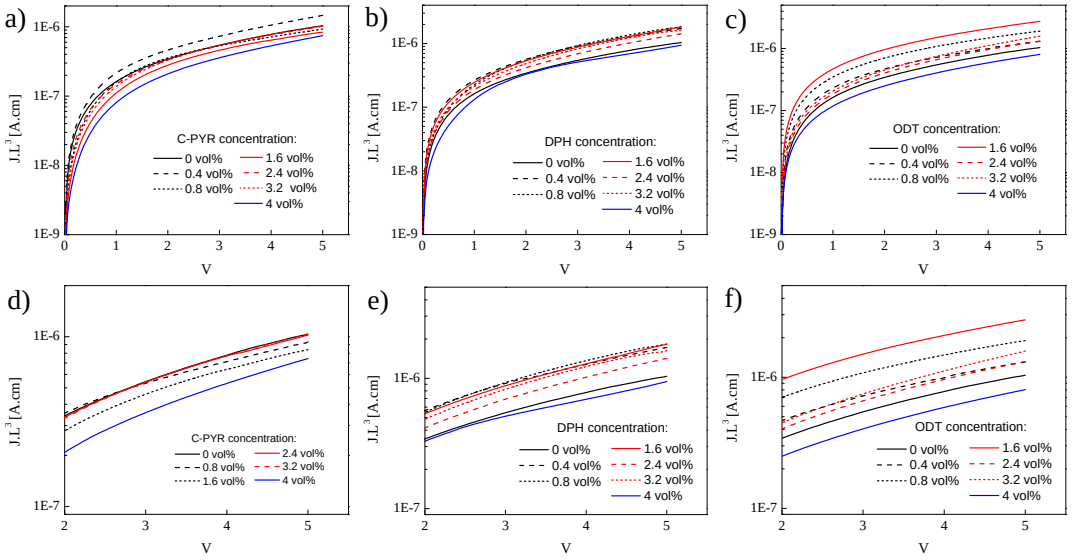

Figure 5.7: J.L^3 as a function of applied voltage for hole-only devices prepared from: a) and d) C-PYR, b) and e) DPH, and c) and f) ODT. Figures a - c) depict plots for an applied voltage ranging from 0 to 5 V and figures d - f) depict zoomed-in plots in the region 2 to 5 V.

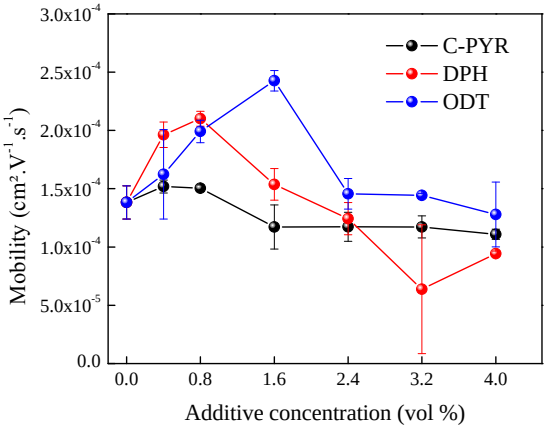

Figure 5.8: Calculated SCLC hole mobility as a function of the concentration of processing additive.

initially with increasing concentration of the processing additive, reaching a certain peak value and then starts to decrease upon increasing concentration. The optimum concentration at which this peak value is reached is 0.8 vol% for C-PYR and DPH, at which the hole mobility reaches 1.5x10^{-4} cm^2.V^{-1}.s^{-1} and 2.1x10^{-4} cm^2.V^{-1}.s^{-1} respectively. For ODT, the optimum concentration is 1.6 vol% and leads to a hole mobility of 2.4x10^{-4} cm^2.V^{-1}.s^{-1}. The two regimes can be explained by the structural modification in the BHJ caused by processing additives. As suggested earlier from the UV-Vis absorption spectra and the XRD measurements above, processing

additives increase the overall crystallinity of P3HT and decrease the crystallite sizes. The initial increase in hole mobility likely reflects the increase in P3HT crystallinity in the BHJ. But alongside with the increased crystallinity, the crystallites get smaller which contributes to reduced sizes of hole transport pathways and the appearance of grain boundaries. The shorter pathways together with the grain boundaries are likely responsible for the decrease in hole mobility at high concentrations of processing additive.

Figure 5.9 displays the evolution of hole mobility as a function of additive concentration along with the FFs of the corresponding OSCs. The graphs show that the variation in hole mobility appears to correlate with the change in FF. For C-PYR and DPH, both the FF and the hole mobility reach their maximum values for an additive concentration of 0.8 vol%. For ODT, the maximums of FF and hole mobility are obtained for a concentration of 1.6 vol%. This suggests that the evolution of FF upon the introduction of processing additive arises from changes in the hole mobility and thus, from the morphological changes caused by the processing additive.

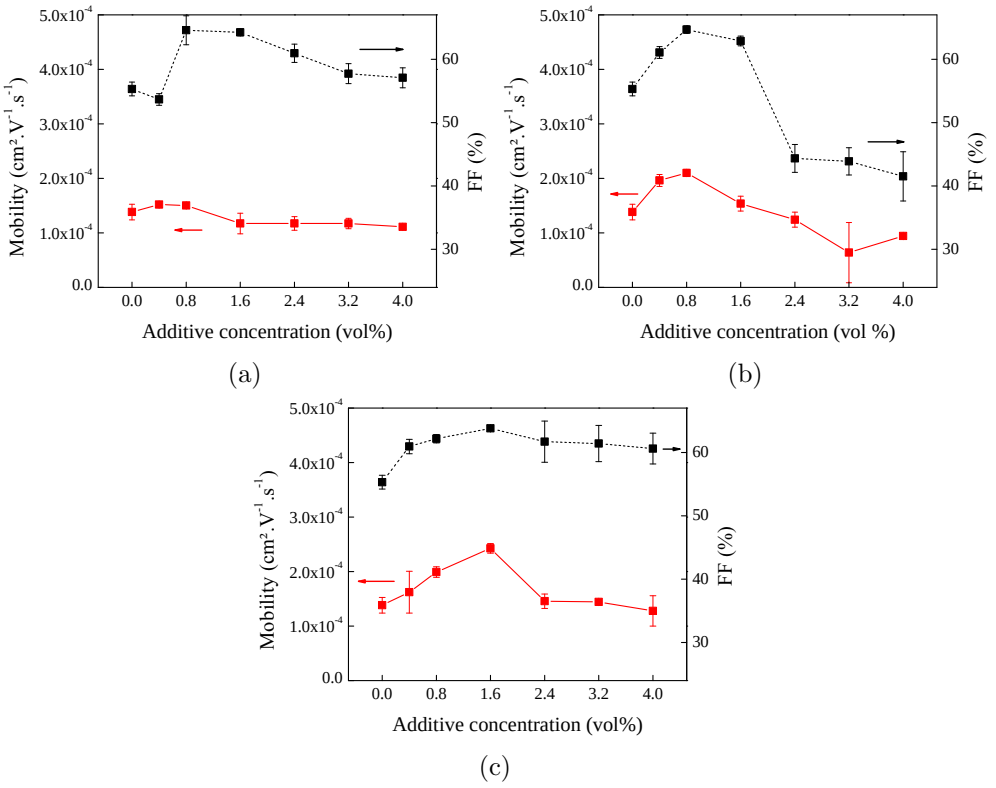

Figure 5.9: Evolution of hole mobility and FF as a function of the concentration of processing additive in OSCs prepared with (a) C-PYR, (b) DPH and (c) ODT.

5.4 Mechanistic effects of processing additives on the self-assembly of P3HT

The optical and structural characterizations showed that processing additives have a significant effect on the BHJ morphology. The introduction of processing additives leads to a morphology which is different from that obtained by means of thermal annealing, as revealed by the XRD measurements. With processing additives, the crystallites of P3HT become smaller and more numerous. Such morphological modifications naturally have an effect on the mobility and the electrical performance. In the literature, a number of mechanisms have been proposed for describing the effects of processing additives. For example, Lee et al. suggested that processing additives lead to three separate phases during the process of liquid-liquid phase separation step of the drying process: a fullerene-additive phase, a polymer aggregate phase and a polymer-fullerene phase. As the processing additive has a higher boiling point, the fullerene remains in solution longer which affects the phase separation [114]. Chen et al. proposed that processing additives provide a driving force for the aggregation of polymer chains [37]. However, neither mechanism adequately explains the evolution of the structure of P3HT crystallites and its dependence on the concentration of processing additive. In this section, a mechanism based on the HSPs of the solvent mixture is proposed.

During the process of solvent evaporation, the higher boiling point of the processing additive causes it to evaporate more slowly than the host solvent and hence the effective concentration of processing additive gradually increases in the solvent mixture. Consequently, the solvent quality towards P3HT changes with time. In order to follow the evolution of the solvent quality towards P3HT, the RED values between the solvent mixture and the polymer are measured. The HSPs of the solvent mixture for various concentration of processing additives are calculated by adding the contributions of each of the component (the processing additive and the ODCB), as described in the following equation:

$$\begin{aligned} \delta D_{mixture} &= \phi_{ODCB}.\delta D_{ODCB} + \phi_{additive}.\delta D_{additive} \\ \delta P_{mixture} &= \phi_{ODCB}.\delta P_{ODCB} + \phi_{additive}.\delta P_{additive} \\ \delta H_{mixture} &= \phi_{ODCB}.\delta H_{ODCB} + \phi_{additive}.\delta H_{additive} \end{aligned} \tag{5.3}$$

where:

$\delta D_{mixture}$, $\delta P_{mixture}$ and $\delta H_{mixture}$ are the HSPs of the solvent mixture,

δD_{ODCB}, δP_{ODCB} and δH_{ODCB} are the HSPs of ODCB,
$\delta D_{additive}$, $\delta P_{additive}$ and $\delta H_{additive}$ are the HSPs of the additive,
ϕ_{ODCB} and $\phi_{additive}$ are the volume fraction of respectively ODCB and the additive in the solvent mixture.

The plots showing the evolution of the RED of P3HT and $PC_{61}BM$ as a function of the effective concentration of the processing additive during film forming are displayed in Figure 5.10. In Figure 5.10, the dotted line at *RED* of 1 represents the threshold value separating the regions where the compound is soluble ($RED < 1$) and non soluble ($RED > 1$) in the solvent mixture.

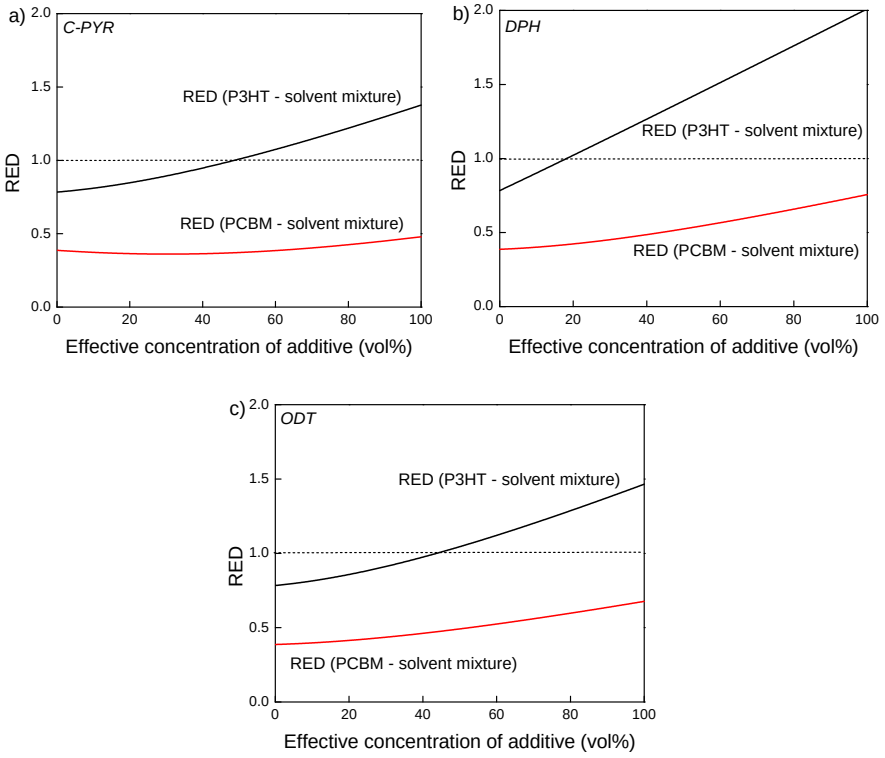

Figure 5.10: Evolution of the *RED* with P3HT (in black) and with $PC_{61}BM$ (in red) as a function of the effective concentration of a) C-PYR, b) DPH and c) ODT. The dotted line at *RED* of 1 depicts the theoretical *RED* threshold value separating the regions where the compound is non-soluble and soluble.

In all cases, the *RED* values between $PC_{61}BM$ and the solvent mixture remain below 1 despite the increasing concentration of additive. Therefore, the solvent mixture remains a good solvent for $PC_{61}BM$ for any concentration of additive. The evolution of the RED values between P3HT and the solvent mixtures exhibits a different behavior. For the initial concentration (from 0 to 4 vol%), the RED between P3HT and the solvent mixture is < 1, meaning that P3HT is soluble in the initial solution mixture. As the

effective concentration of the additive increases, the RED also increases, eventually reaching the threshold concentration at which the RED becomes 1. The threshold concentrations for C-PYR and ODT are 49 vol% and 44 vol% respectively, whereas for DPH, it is only 18 vol%. When the concentration of additive has reached the threshold concentration, the solvent mixture becomes a poor solvent for P3HT while remaining a good solvent for $PC_{61}BM$. The change in solvent quality causes the transition of P3HT from the liquid state to the solid state by the formation of nuclei of P3HT. Without processing additive, the transition from the liquid state to the solid state happens when the solubility limit of P3HT is reached [187] and with processing additive, the transition is shifted forward.

The XRD data showed that the size of the P3HT crystallite domains is dependent on the initial concentration of the processing additive. This effect can also be understood using the RED versus processing additive concentration plots. For a formulation with a given concentration of processing additive, a certain volume of the host solvent has to evaporate before reaching the threshold concentration. When the initial concentration of the processing additive is high, a small amount of the host solvent has to evaporate before the threshold concentration is reached. Therefore, the P3HT nucleates in a medium that is fairly dilute. In this case, the P3HT chains are more spread apart and are also given less time to assemble before the nucleation process starts. As a result, the crystallites of P3HT are expected to be more numerous and smaller. On the other hand, when the initial concentration of the processing additive is low, a larger amount of the host solvent needs to evaporate before the threshold concentration is reached. The P3HT chains nucleate in a more concentrated medium and are given more time to aggregate prior to the transition from the liquid to the solid states. Consequently, the crystallites are larger than in the first case. The starting concentration therefore plays a crucial role in the size and the amount of crystallites in the final BHJ morphology. Figure 5.11 illustrates the BHJ morphologies obtained from D/A formulations containing different starting concentrations of processing additive.

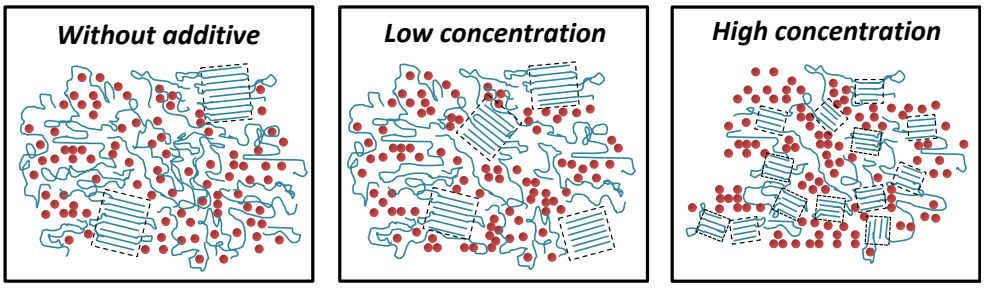

Figure 5.11: Schemes representing the BHJ morphology spin-cast from formulations with various concentration of additive. The crystallites of P3HT become more numerous and smaller as the starting concentration or processing additive increases.

5.5 Conclusions

Correlating structural and optical characterizations revealed the mechanistic role of processing additives in improving the BHJ morphology, hence attaining higher OSC efficiency. The characterizations were performed on BHJs with varying concentration of processing additives, investigating, in this pursuit, three processing additives with different chemical structures in order to determine and verify the universality of the behavior.

The evolution of the V_{oc} and of the UV-Vis absorption spectra showed that processing additives increased the overall crystallinity of P3HT in the BHJ whereas XRD patterns revealed that the increased crystallinity is associated with a decrease in the polymer crystallite sizes. These results suggest that processing additives leads to the formation of BHJ with more numerous but smaller polymer crystallites. Studies of charge carrier mobility revealed that this modification in crystallinity caused the mobility to increase at first but ultimately to decrease because of factors accompanying the crystallinity such as the appearance of grain boundaries.

In order to determine how such a morphology can be induced, the role of processing additives during solvent evaporation is identified by studying the evolution of the RED values (e.g. the interactions) between the solvent mixture and the compounds. At the initial stage, both P3HT and $PC_{61}BM$ are soluble in the solvent mixture. As the host solvent evaporates, the concentration of processing additive increases until reaching a threshold concentration at which the polymer chains start to nucleate. The nucleation process and the growth of the nuclei are dependent on the initial concentration of processing additive, as illustrated in Figure 5.11. A high initial concentration of the processing additive leads to smaller but more numerous polymer crystallites whereas

a low concentration leads to larger but less numerous crystallites. The morphological changes closely explain the evolution of the electrical parameters of OSCs with processing additives.

Chapter 6

Effect of device architecture on OSCs prepared with additives

6.1 Introduction

In practice, OSCs can be fabricated in two different architectures: conventional or inverted. In the conventional architecture, the photo-generated electrons are collected by the top electrode whereas in the inverted architecture they are collected by the bottom electrode. The structure of the OSCs and the types of interlayers used are depicted in Figure 6.1.

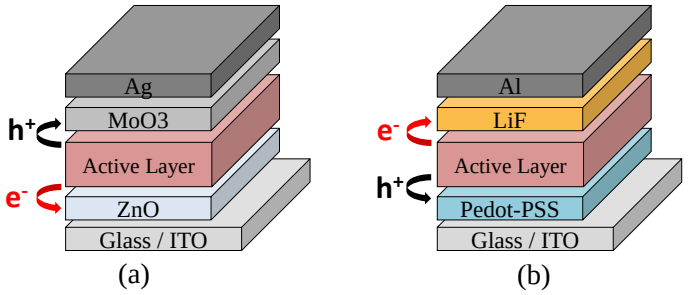

Figure 6.1: OSC architecture: (a) inverted and (b) conventional.

The previous chapters depicted OSCs that were fabricated exclusively in inverted configurations. Here, the effect of device architecture on the performance of OSCs prepared with additive is studied. The initial motivation behind this study is to determine whether processing additives cause a vertical phase separation of D and A in the BHJ.

Vertical phase separation appears to be an important parameter for the efficiency of OSCs [236], but currently there is no clear consensus on this subject [96, 167, 168]. Vertical phase separation was shown to be dictated by several parameters such as the surface energy of the layer beneath the active layer [27, 62], the application of a thermal annealing treatment [208, 231] and the spin-casting conditions [27]. Overall, the literature suggests that processing conditions affect the vertical phase separation in BHJ and it is therefore natural to verify whether processing additives also play a role in phase separation. In case of vertical phase separation induced by additives, the performance of additive-treated OSCs would be sensitive to the device architecture. Comparing the photovoltaic parameters of OSCs fabricated in inverted and in conventional architectures represents therefore an indirect approach to verify whether such vertical phase separation occurs in the active layer.

The studies presented here are carried out with two processing additives: DPH and ODT.

6.2 Electrical performance of OSCs using different architectures

6.2.1 OSCs with ODT

OSCs prepared with various concentrations of ODT (0 to 2.4 vol%) are fabricated in an inverted and in a conventional architecture. The J-V characteristics of the OSCs are measured and Figure 6.2 shows the photovoltaic parameters (V_{oc}, J_{sc}, FF, PCE, R_s and R_{sh}) of the OSCs as a function of additive concentration. The data in the figures represents the average values obtained from four to eight OSCs for each system.

The V_{oc} and the R_{sh} decrease with increasing concentration of additive independent of the type of architecture used. Apart from V_{oc} and R_{sh}, the other electrical parameters demonstrate significant differences as a function of the type of device architecture. The most significant difference arises from the FF: in conventional OSCs, the FF decreases significantly upon the introduction of the additive while in inverted OSCs, not much change is observed. When OSCs are prepared with 2.4 vol% of ODT, the FF of conventional OSCs drops to 0.31 causing the PCE to decrease to 1.23 % (less than half the PCE of OSC without additive). Significant differences are also observed from the J-V characteristics of OSCs (Figure 6.3). The J-V characteristics under illumination of conventional OSCs prepared with 2.4 vol% of ODT demonstrate a S-shape behavior which is generally associated with charge accumulation [176, 218]. This can be induced by several parameters such as interfacial barriers [42, 218] and unbalanced charge carrier mobilities [176]. In contrast, the J-V characteristics of inverted OSCs do not exhibit this behavior. Clearly, the processing additives give different effects in the different architectures. While ODT is highly beneficial for the performance of inverted OSCs, it demonstrates negative impact on that of conventional OSCs. In order to verify that these trends are not limited to the specific use of ODT only, similar studies are carried out with DPH.

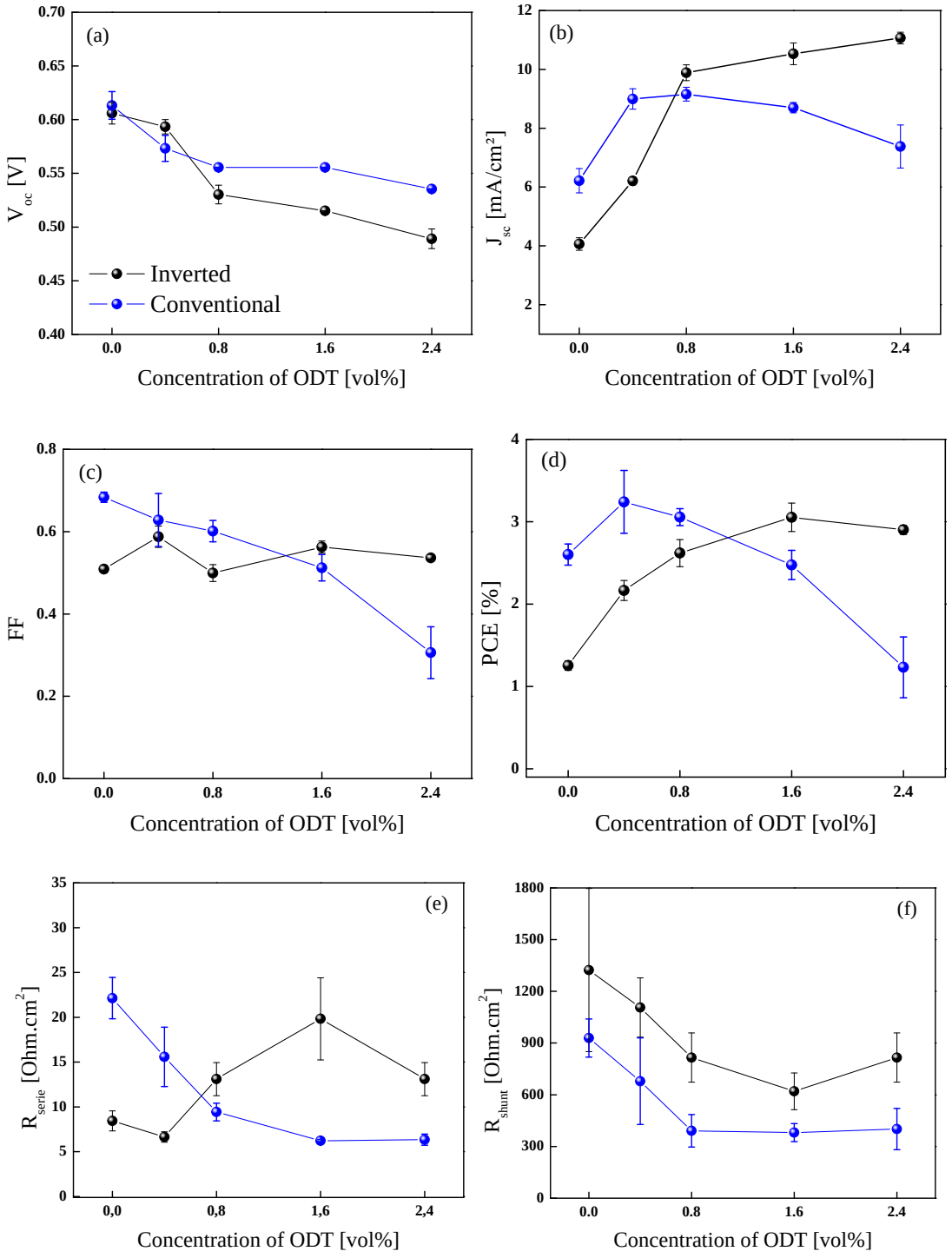

Figure 6.2: Effects of ODT on the electrical parameters in a conventional and in an inverted architecture of OSCs: (a) V_{oc}, (b) J_{sc}, (c) FF, (d) PCE, (e) R_s and (f) R_{sh}.

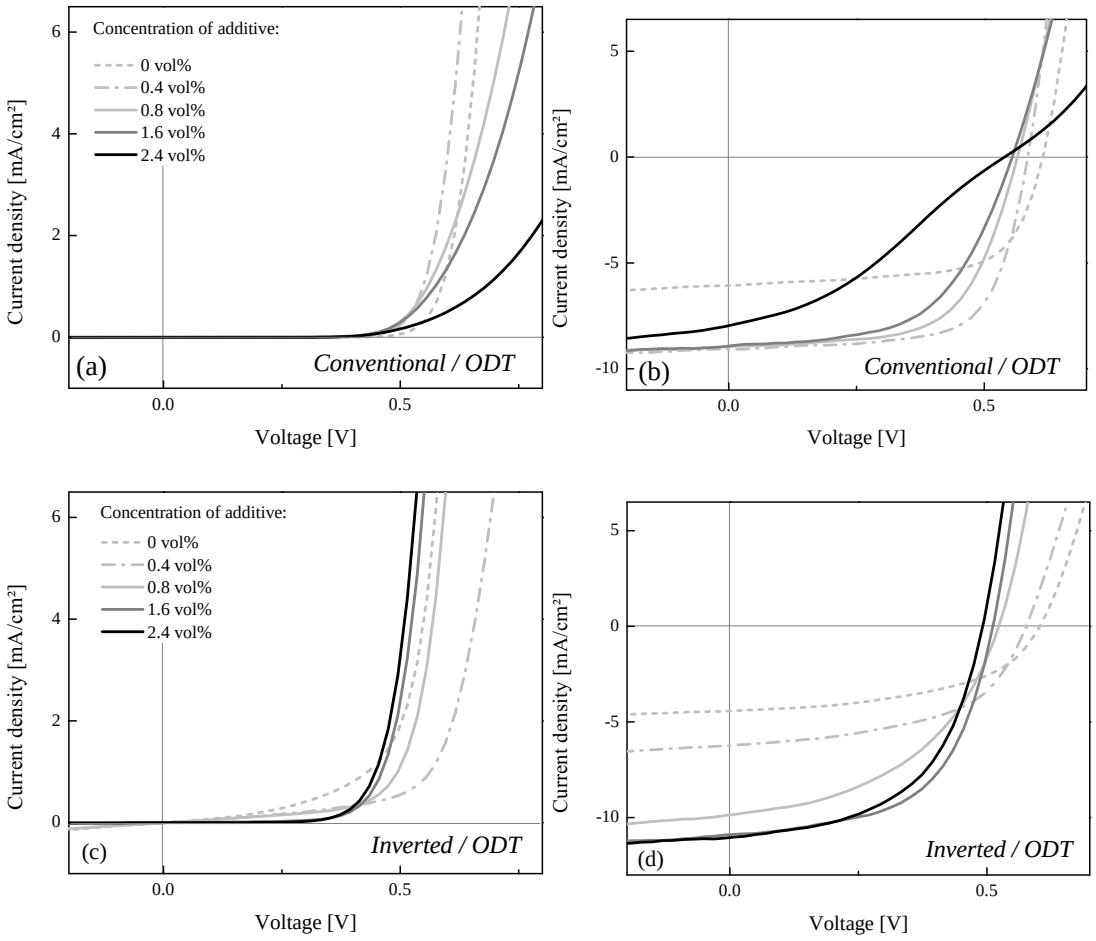

Figure 6.3: J-V curves of OSCs with various concentrations of ODT under dark conditions (a) in a conventional configuration and (c) in an inverted configuration and J-V curves under illumination (b) in a conventional configuration and (d) in an inverted configuration.

6.2.2 OSCs with DPH

Similar to ODT, OSCs prepared with solutions containing various concentrations of DPH are fabricated in an inverted and in a conventional architecture. Figure 6.5 shows the photovoltaic parameters (V_{oc}, J_{sc}, FF, PCE, R_s and R_{sh}) of the OSCs and their corresponding concentrations. The data in the figures represents the average values obtained from four to eight OSCs for each system.

The electrical performance shows a similar trend as previously observed with ODT. V_{oc} and R_{sh} decrease with increasing concentration of DPH regardless of the architecture. The FF and the J_{sc} exhibit poor values at high DPH concentration in conventional OSCs while in inverted OSCs, the FF remains relatively unchanged and the J_{sc} is

increased. In the case of DPH, the differences between conventional and inverted OSCs appear to be more pronounced than in the ODT case. Conventional OSCs prepared with 2.4 vol% of DPH exhibit a particularly low efficiency with a FF of 0.23 and an average PCE of 0.12%. This low performance is expected from the non-diode behavior observed in its J-V characteristics depicted in Figure 6.4.

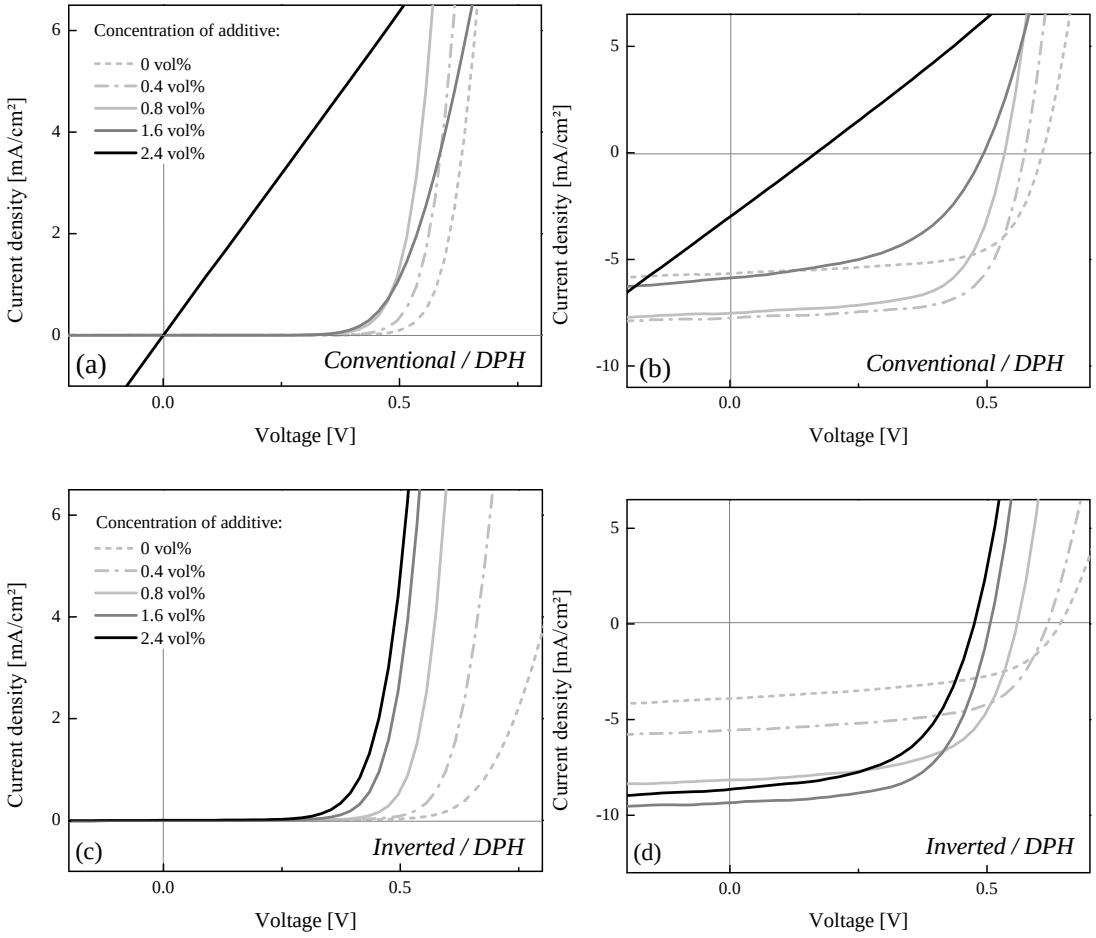

Figure 6.4: J-V curves of OSCs with various concentrations of DPH under dark conditions (a) in a conventional configuration and (c) in an inverted configuration and J-V curves under illumination (b) in a conventional configuration and (d) in an inverted configuration.

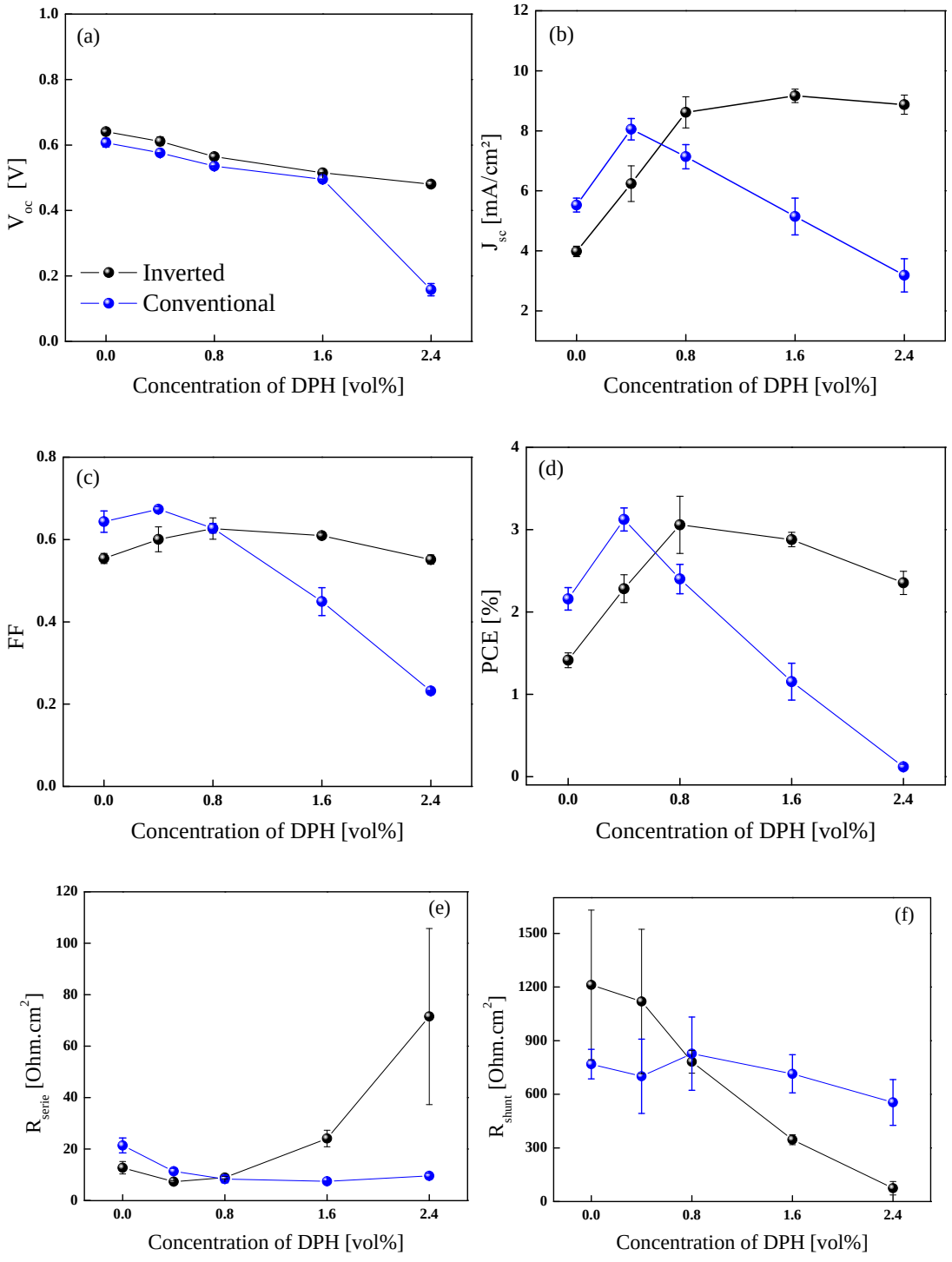

Figure 6.5: Effects of DPH on the electrical parameters in a conventional and in an inverted architecture of OSCs: (a) V_{oc}, (b) J_{sc}, (c) FF, (d) PCE, (e) R_s and (f) R_{sh}.

6.2.3 Conclusions on OSCs with ODT and DPH

Overall, the additives demonstrate different effects on the photovoltaic performance depending on the OSC architecture. The PCE of conventional OSCs decreases significantly upon the introduction of processing additive whereas the PCE increases in the case of inverted OSCs. The difference between the two architectures could be explained by the location where the charge carriers are collected (Figure 6.1). In an inverted architecture, the holes are collected by the top electrode suggesting that the charge transport of holes is facilitated if D pathways are predominantly present in the top of the active layer. In other words, a BHJ with a P3HT-enriched layer on the top and a $PC_{61}BM$-enriched layer on the bottom is preferred for inverted OSCs. This is depicted in the scheme (b) in Figure 6.6 which shows the schematic illustrations of three scenarios of vertical phase separation. The fact that additives perform better in inverted OSCs compared to conventional OSCs leads to the hypothesis that a vertical phase separation as indicated in (b) takes place.

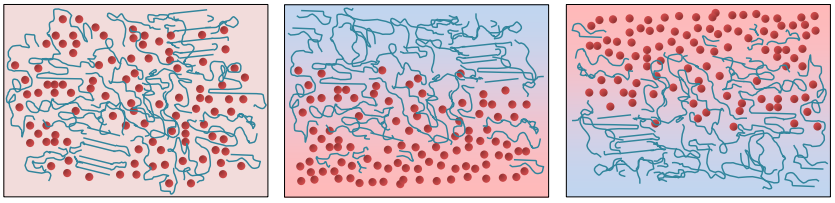

Figure 6.6: Different scenarios of vertical phase separation in BHJ: (a) no vertical phase separation - homogeneous active layer, (b) BHJ with a P3HT-enriched top and a $PC_{61}BM$-enriched bottom and (c) BHJ with a P3HT-enriched bottom and a $PC_{61}BM$-enriched top.

As the proportions of D and A in the layer are expected to influence the charge carrier mobility, the hypothesis of vertical phase separation is verified by means of hole and electron mobility measurements using an organic thin film transistor (OTFT) configuration. Such technique appears to be suitable for this study as it selectively measures the mobility at the lower part of the active layer.

6.3 Measurements of charge carrier mobility using OTFT configuration

6.3.1 Fabrication of OTFTs

The electron and hole mobilities are respectively measured using n-type and p-type OTFTs. In n-type OTFTs, a positive gate-source voltage leads to the formation of a negative channel at the interface between the semiconductor and the dielectric, where electrons can be injected by the source and collected by the drain. In p-type OTFTs, a negative gate-source voltage is applied to form a positive channel at the interface where hole transport can occur. Source and drain consist of aluminum as a low work function metal for n-type OTFTs, and of gold as a high work function metal for p-type OTFTs.

The transfer characteristic (which is the drain-source current (I_{DS}) as a function of the gate-source voltage (V_{GS})) is measured at a drain-source voltage (V_{DS}) of +5 V for n-type OTFTs and -5 V for p-type OTFTs. The mobility is extracted from the saturation regime where $|V_{DS}| > |V_{GS}\text{-}\ V_{th}| > 0$.

In the saturation regime, the current is given by:

$$I_{DS} = \frac{\mu_{sat} C_i W}{2L}(V_{GS} - V_{th})^2 \tag{6.1}$$

and the carrier field effect mobility is given by:

$$\mu_{sat} = \frac{2L}{C_i W}\left(\frac{\partial\sqrt{I_{DS}}}{\partial V_{GS}}\right)^2 \tag{6.2}$$

where V_{th} is the threshold voltage, C_i the gate dielectric capacitance per unit area, μ_{sat} the mobility, W the channel width and L the channel length.

6.3.2 Mobility measurements of films prepared from ODT

N-type and p-type OTFTs are fabricated with P3HT/$PC_{61}BM$ active layers prepared with various concentrations of ODT (from 0 to 2.4 vol%). The transfer characteristics of the OTFTs are shown in Figure 6.7.

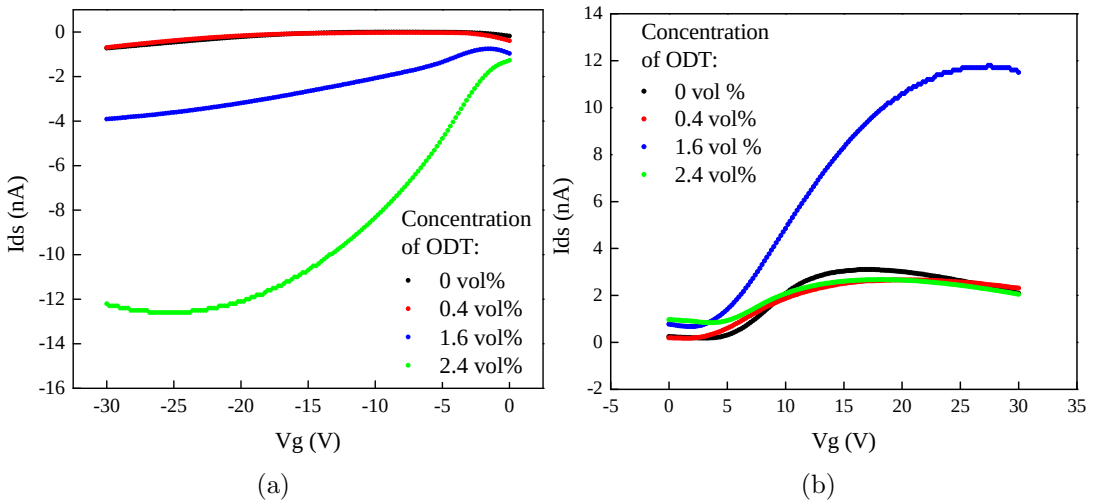

Figure 6.7: Transfer characteristics of OTFTs prepared with various concentrations of ODT in: (a) p-type OTFTs and (b) n-type OTFTs.

In p-type OTFTs, the transfer characteristics show that higher I_{DS} is obtained in films treated with ODT. In contrast, for the n-type OTFTs, no significant change is observed from the transfer characteristics, except those prepared with 1.6 vol% of ODT.

The mobilities are then calculated for different values of V_{GS} using Equation 6.2. The extracted hole and electron mobilities are plotted as a function of V_{GS}-V_{th} in Figure 6.8a. For p-type OTFTs prepared from 0 and 0.4 vol% of ODT, the I_{DS} in the transfer characteristics is so low that the calculated hole mobilities appear to be in the noise margin and can therefore not be considered reliable. For ODT concentrations $\geq$ 1.6 vol%, the hole mobility increases significantly. In order to evaluate clearly the dependence of electron and hole mobilities on ODT concentration, they are extracted and compared at V_{GS}-V_{th} values of + (or -) 2 V for electron (or hole) mobility. The mobility values are depicted as a function of ODT concentration in Figure 6.8b. Table 6.1 shows the corresponding mobility values as well as the ratio of hole mobility (μ_{h^+}) over electron mobility (μ_{e^-}).

Figure 6.8b clearly shows that hole mobility increases with increasing concentration of ODT while electron mobilities remain relatively unchanged upon the introduction of ODT. Films prepared with concentrations of ODT $\leq$ 1.6 vol% demonstrate a μ_{h^+}/μ_{e^-} ratio $<$ 1 indicating higher electron mobility. However, OTFTs with an ODT concentration of 2.4 vol%, exhibit a μ_{h^+}/μ_{e^-} ratio of 7.05 indicating that additives cause the hole mobility to surpass that of electrons.

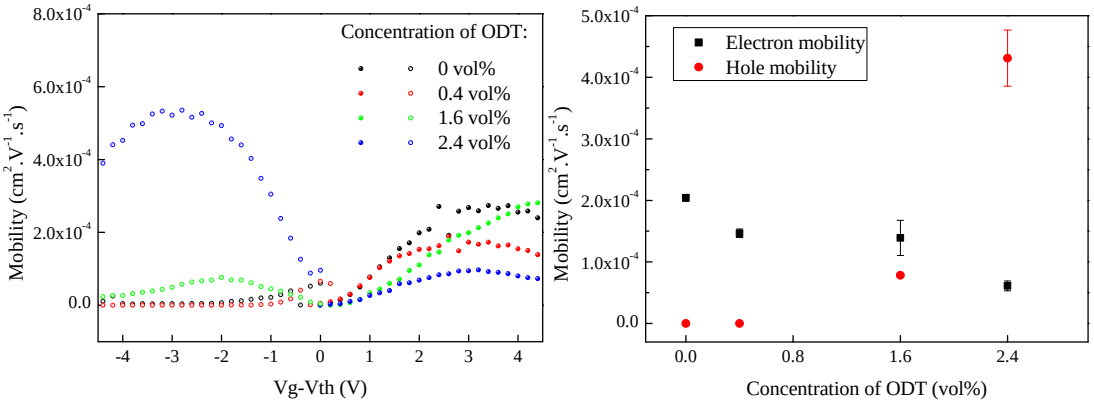

(a) (b)

Figure 6.8: (a) Mobility values of OTFTs prepared with various concentrations of ODT as a function of V_{GS}-V_{th}: the left side of the graph depicts hole mobility and the right side the electron mobility. (b) Electron and hole mobilities at V_{GS}-V_{th} of +2 V and -2 V respectively, as a function of ODT concentration.

Table 6.1: Mobility of holes and electrons as a function of the concentration of ODT.

ODT ratio [vol%]	N-TYPE $*10^{-4}$[$cm^2.V^{-1}.s^{-1}$]	P-TYPE $*10^{-4}$[$cm^2.V^{-1}.s^{-1}$]	μ_{h^+}/μ_{e^-}
0	2.04 ±0.06	~ 0	-
0.4	1.47 ±0.07	~ 0	-
1.6	1.39 ±0.29	0.78 ±0.03	0.56
2.4	0.61 ±0.08	4.31 ±0.46	7.05

6.3.3 Mobility measurements of films prepared from DPH

Similarly to ODT, n-type and p-type OTFTs are fabricated with active layers prepared with concentrations of DPH ranging from 0 to 2.4 vol%. Figure 6.9 depicts the transfer characteristics of the n-type and p-type OTFTs. The transfer characteristics of p-type OTFTs, depicted in Figure 6.9a, also demonstrate higher I_{DS} upon increasing DPH concentration.

Next, the OTFT mobilities are calculated at different values of V_{GS} using Equation 6.2. Figure 6.8a depicts the hole and electron mobilities as a function of V_{GS}- V_{th} for OTFTs prepared from various concentrations of DPH and Figure 6.8b shows the evolution of the electron and hole mobility extracted at V_{GS}- V_{th} values of +2 V and -2 V respectively. Similarly to the case of ODT, the hole mobility increases with increasing concentration of DPH. It is found here that the electron mobility decreases upon the

introduction of DPH. The ratios μ_{h^+}/μ_{e^-}, presented in Table 6.2, are shown to be < 1 in OTFTs prepared with DPH concentrations ≤ 0.8 vol%. This ratio increases and is > 2 for OTFTs prepared with DPH concentrations of 1.6 and 2.4 vol%. This indicates that the introduction of DPH also cause the hole mobility to surpass that of electrons, similar to that observed with ODT.

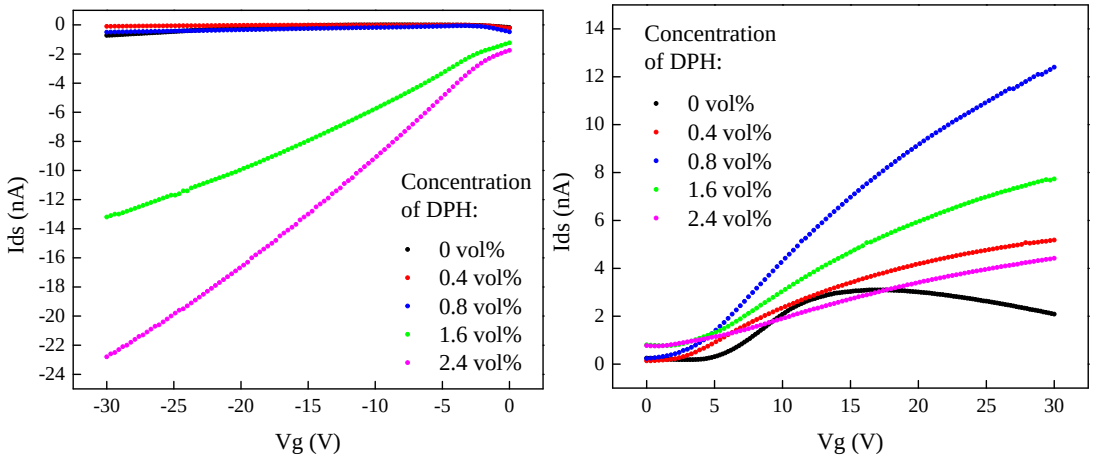

Figure 6.9: Transfer characteristics of OTFT prepared with various concentrations of DPH in: (a) p-type OTFTs and (b) n-type OTFTs.

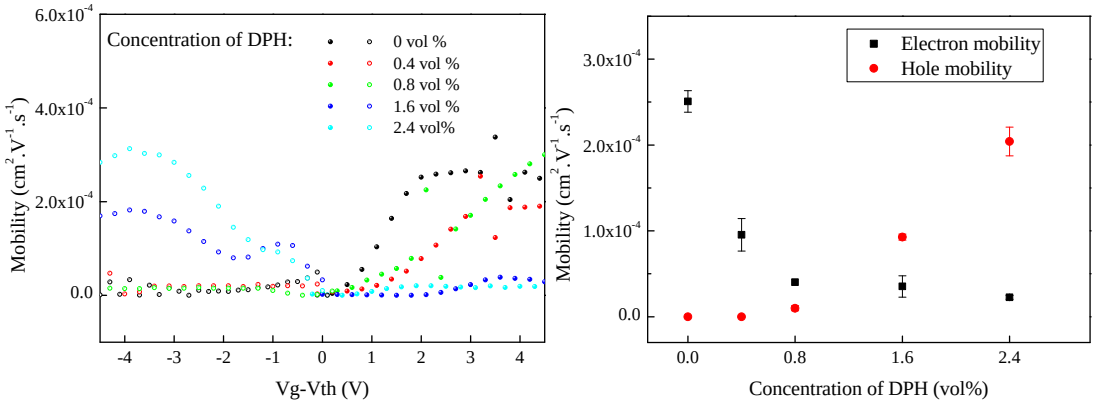

Figure 6.10: (a) Mobility values of OTFTs prepared with various concentrations of DPH as a function of V_{GS}-V_{th}: the left side of the graph depicts hole mobility and the right side the electron mobility. (b) Electron and hole mobilities at V_{GS}-V_{th} of +2 V and -2 V respectively, as a function of DPH concentration.

Table 6.2: Mobility of holes and electrons as a function of the concentration of DPH.

DPH ratio [vol%]	N-TYPE $*10^{-4}[cm^2.V^{-1}.s^{-1}]$	P-TYPE $*10^{-4}[cm^2.V^{-1}.s^{-1}]$	μ_{h^+}/μ_{e^-}
0	2.51 ±0.12	∼0	-
0.4	0.95 ±0.19	∼0	-
0.8	0.40 ±0.00	0.10 ±0.03	0.25
1.6	0.35 ±0.12	0.93 ±0.04	2.63
2.4	0.23 ±0.02	2.04 ±0.17	9.02

6.4 Origins of additive dependence on OSCs architecture

In order to explain the higher performance obtained from an additive-treated OSC in an inverted architecture compared to a conventional one, the question of the vertical phase separation with a depleted polymer layer at the bottom was addressed. The results show that OTFTs prepared with processing additives exhibit an enhanced hole mobility compared the OTFTs without the additive. This result suggests that processing additives do not lead to any vertical phase separation that decreases the D concentration in the lower part of the film. In view of the results obtained in OTFT-mobility measurements, it is concluded that the difference between conventional and inverted architectures do not arise from vertical phase separation. This observation is in disagreement with a recent report by Wang et al. where several techniques (transmission electron microtomography, X-ray photoemission spectroscopy and dynamic secondary ion mass spectroscopy) were used to suggest that the introduction of ODT caused the formation of a P3HT-depleted layer at the bottom of the BHJ [216]. However, the OTFT-mobility measurements conducted here show that, even in the hypothetical case of vertical phase separation caused by additives, the electron and hole mobilities are not impacted by it.

Ruling out vertical phase separation effects, the difference between conventional and inverted OSCs may instead be explained in terms of the location where the excitons are formed. In both architectures, the light is received by the OSC through the ITO substrate. Consequently, photon absorption is expected to occur predominantly in the bottom part of the active layer. As a result, charge carriers are also predominantly generated near the bottom. In a conventional architecture, the electrons are collected by the top electrode. In this case, the photo-generated electrons have to traverse across

the whole thickness of the organic layer to be collected by the top electrode. In contrast, holes travel a much shorter distance to reach the hole collecting electrode. Therefore, in this configuration, a high electron mobility is more favorable to account for the long distance that the electrons need to travel. In other words, a ratio $\mu_{h^+}/\mu_{e^-} < 1$ is preferred in this configuration. Such a mobility ratio is obtained in films treated with low concentrations of additive. This, in turn, could explain the superior performance of conventional OSCs prepared with low concentrations of additive as depicted in Figure 6.2 and Figure 6.5. An explanatory scheme supporting this proposition is depicted in Figure 6.11.

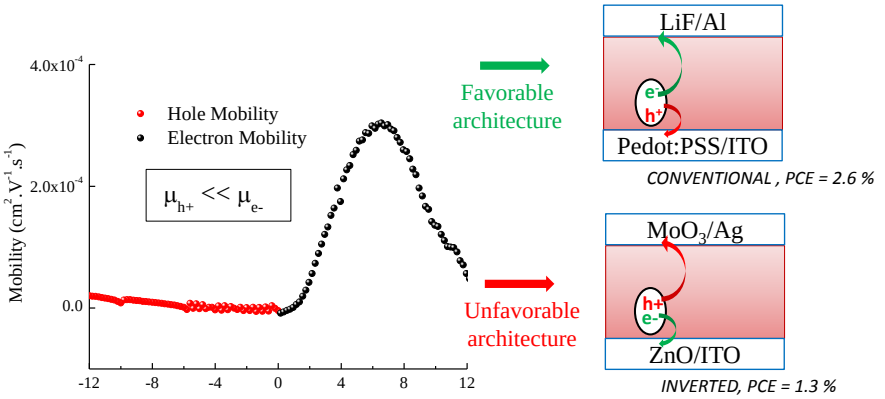

Figure 6.11: A schematic description of hole and electron transport in OSC without processing additive and subsequent preferential architecture.

In contrast, in an inverted architecture, most of the photo-generated holes are required to travel a longer distance relative to the electrons. In this configuration, a ratio $\mu_{h^+}/\mu_{e^-} > 1$ can be expected to be more favorable for a more balanced collection. As the introduction of processing additive increases the hole mobility, the inverted architecture is favorable here. An explanatory scheme supporting this proposition is depicted in Figure 6.12.

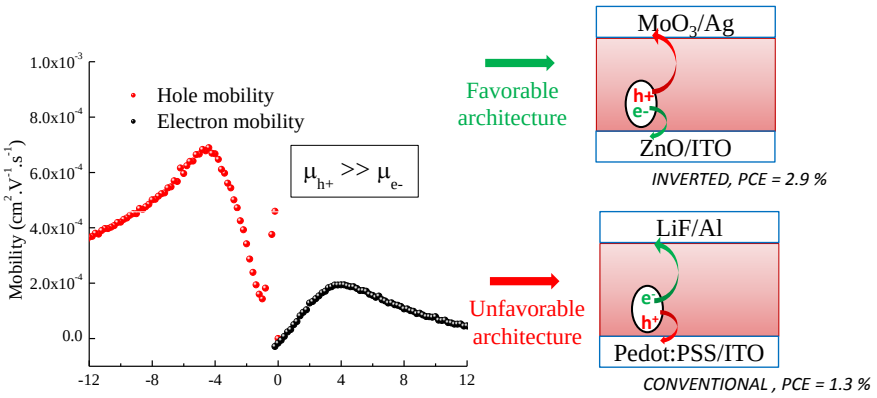

Figure 6.12: A schematic description of hole and electron transport in OSC prepared with 2.4 vol% of additive and subsequent preferential architecture. OSCs with 2.4 vol% depict the case where hole mobility is higher than electron mobility.

To conclude, additive-treated OSCs were shown to perform better in inverted OSCs compared to conventional OSCs. The results of OTFT mobility measurements confirmed that vertical phase separation is not responsible for the differences obtained in conventional and inverted OSCs. Instead, the increasing hole mobility with additive concentration indicates that the difference arises from the location where the excitons are formed. Additionally, this analysis indicates that the ratio of electron and hole mobilities appear to play a crucial role in the choice of OSC architecture.

Chapter 7

The effects of processing additives on the stability of OSCs

In this chapter, the question of the effect of the active layer processing conditions on the stability of OSCs is addressed. Commercial application of OSCs is only viable when stability requirements are met. Therefore the research on OSCs cannot be only focused on higher efficiencies, but also on the stability. Much research has focused on several stability related topics that include the identification of degradation factors and mechanisms, and routes for stability improvement. Therefore, before addressing the question of the effect of processing additives on the OSC stability, it is prudent to provide first a brief background on the stability issues of OSCs.

7.1 Background on the stability issues of OSCs

7.1.1 Stability of organic semiconductors

Organic semiconducting materials are known for their relatively poor stability to ambient conditions. Pure P3HT was shown to be susceptible to photo-bleaching in the presence of oxygen in the solution state [4], as well as in the solid state [83, 139, 140]. In the solid state, the degradation occurs by radical oxidation that first occurs at the side chains and further leads to the degradation of the polythiophene ring causing a loss of π-conjugation. Such degradation appears in the form of a decrease in the polymer optical absorption in the UV-Vis absorption spectrum. The photo-oxidation is accelerated in the presence of humidity, light and high temperature [83]. Aside from the light-induced changes in the presence of oxygen, P3HT is also subject to degradation under light irradiation in the absence of oxygen, a phenomenon called photolysis [138]. It is noteworthy to point out that the degradation rate caused by photolysis is much slower. Manceau et al. showed that light irradiation of P3HT in inert atmosphere caused its absorbance to decrease by 20% within 10 000 hours, whereas the same happens in only 20 hours in the presence of oxygen [138].

Despite the severe degradation behavior observed in neat materials, blends of D/A generally exhibit less degradation. The introduction of fullerene derivatives was shown to slow down the rate of photo-oxidation and photolysis of π-conjugated polymers [30, 155, 184]. Figure 7.1 compares the UV-Vis absorption spectra of neat polymer and of polymer/$PC_{61}BM$ blends under light irradiation in the presence or absence of oxygen.

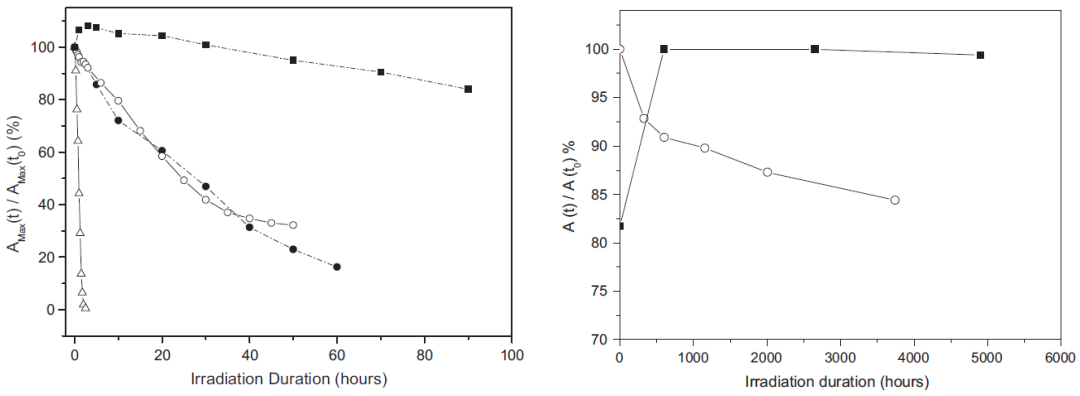

(a) (b)

Figure 7.1: (a) Normalized UV-Vis absorption (at 500 nm) of MDMO-PPV (△), MDMO-PPV/$PC_{61}BM$ (◯) and normalized UV-Vis absorption (at 520 nm) of P3HT (●) and P3HT/$PC_{61}BM$ (■) samples during photo-oxidation. (b) Normalized UV-Vis absorption of MDMO-PPV/$PC_{61}BM$ (at 500 nm (◯)) and P3HT/$PC_{61}BM$ (at 520 nm (■)) samples during photolysis. Reproduced from reference [180] with permission of Elsivier.

The comparison demonstrates that the introduction of $PC_{61}BM$ reduces significantly the photo-bleaching of P3HT in the presence of oxygen and suppresses it almost completely in the absence of oxygen [180]. In inert atmosphere, the optical properties of P3HT were shown to be stable for periods as long as 5000 hours. The enhanced photostability of blends was attributed to radical scavenging property of $PC_{61}BM$ and its ability to quench the P3HT singlet state [138].

Thermal stability represents a severe issue in the stability of D/A blends, mainly due to the tendency of $PC_{61}BM$ to form micrometer size crystals. Such crystals can be observed in optical microscopy, as depicted in the Figure 7.2 which shows a thermally annealed P3HT/$PC_{61}BM$ films exhibiting $PC_{61}BM$ crystals.

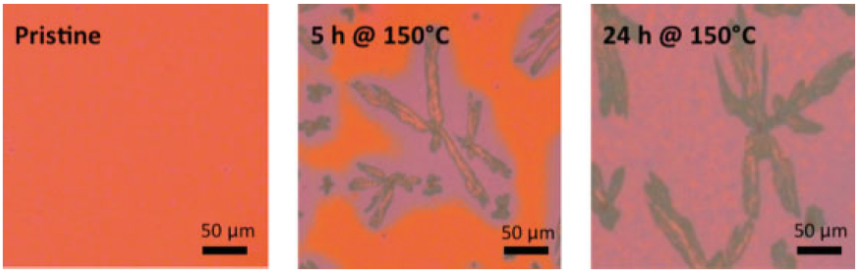

Figure 7.2: Optical microscopy images of P3HT/$PC_{61}BM$ layers before and after being thermally annealed at 150^{o}C for 5 hours or 24 hours. Reproduced from reference [222] with permission of Wiley.

7.1.2 Stability of OSCs

The factors that cause degradation at the material level such as oxygen and light irradiation subsequently cause significant failure at the device level. Additionally, the OSCs under usage conditions can be subject to several other degradation mechanisms such as electrical stress and mechanical stress [23]. The mechanisms of degradation can be categorized in three types:[65]

1. Degradation of D and A materials,

2. Morphological changes in the active layer,

3. Interfacial degradation.

Oxygen was shown to play a key role in degradation mechanisms (1) and (3). The effects of oxygen on mechanism (1) were discussed previously. Additionally, oxygen induces several types of interfacial degradation mechanism especially in conventional OSCs [104, 219]. Inverted OSCs in which holes are collected by the top electrode are more stable, owing in part, to the higher work function of the top electrode [49, 132]. Nevertheless, even in inverted OSCs, oxygen remains one the major factors of degradation because of the severe damages caused to the active layer [188]. In order to prevent deterioration from oxygen and humidity, much work has been done on the use of protection barriers and as a result, OSCs protected with barriers could demonstrate stabilities of several years [74, 105, 108]. To conclude, the issue of oxygen can then (at least partially) be solved by choosing an appropriate device architecture as well as using barriers to encapsulate OSCs.

In the absence of oxygen, light irradiation only does not play a major role on mechanisms 1 and 2. However, several studies did reveal the dependence of the photo-stability of OSCs on the types of interlayers suggesting the presence of photo-degradation at the interfaces (mechanism 3) [212, 225].

As reported in this brief literature review, each component of an OSC is subject to degradation: the electrodes, the interface between active layer and the contacts, and the organic semiconducting materials. These components have to be chosen carefully in order to limit OSCs degradation. On the other hand, the dependence of OSCs stability on the active layer morphology - and subsequently the processing conditions - has not yet been addressed adequately.

In this chapter, the photo-stability of OSCs that are thermally annealed is compared to the photo-stability of OSCs fabricated using additives. Stability tests under light irradiation in air and in inert atmosphere are performed and compared. In order to limit thermal degradation of OSCs, the temperature of the substrates is kept below 32°C during light irradiation.

7.2 Traces of processing additives in the active layer

The boiling points of the processing additives are relatively high (C-PYR: 306 °C, DPH: 284 °C, ODT: 270 °C and TRIB: 388 °C). Therefore, traces of them can be expected to be present in the active layer and to subsequently alter the stability of OSCs.

In order to detect the presence of processing additive in the active layer, infra-red (IR) absorption spectra of the active layers are characterized with Polarization Modulation-Infrared Reflection Absorption Spectroscopy (PM-IRRAS). The PM-IRRAS spectrum is compared to that of the pure additive determined by Attenuated Total Reflectance (ATR) Spectroscopy to detect whether peaks related to the additive are present in the PM-IRRAS spectrum. For each additive, two sets of P3HT/PC_{61}BM films are investigated: one set consists of as cast-films and a second set consists of films that were placed under vacuum at a pressure of $\sim$ 5x10^{-6} mbar, which reproduces the vacuum step caused by thermal evaporation of top contacts. Figure 7.3 depicts a scheme explaining the tests. The films of P3HT/PC_{61}BM are spin-cast from solutions containing 1.6 vol% of processing additives on ITO substrates coated with ZnO. A P3HT/PC_{61}BM-film spin-cast without processing additive serves as a control film.

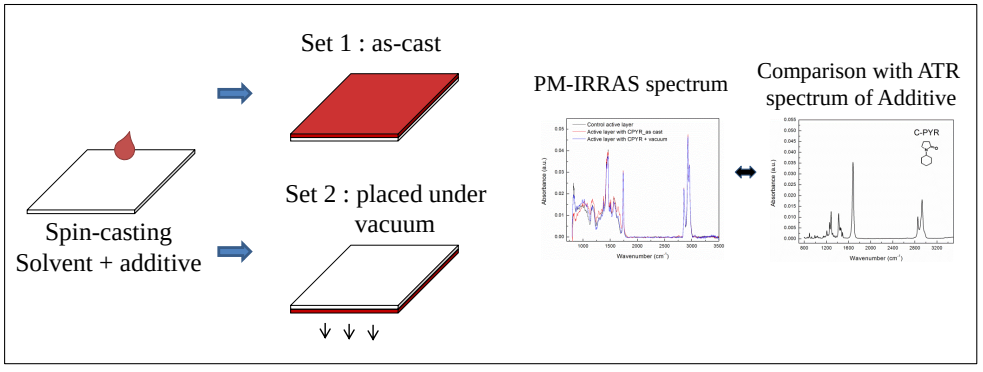

Figure 7.3: Scheme of the procedure for the detection of processing additive in P3HT/PC_{61}BM films.

- PM-IRRAS spectra of C-PYR-treated active layers

As depicted in the ATR spectrum of C-PYR in Figure 7.4a, C-PYR exhibits an intense absorption peak at 1683 cm^{-1} that accounts for the C=O stretching mode. Figure 7.4b shows the PM-IRRAS spectra of P3HT/PC_{61}BM films, prepared with and without C-PYR, in the 1600 – 1900 cm^{-1} region. The peak at 1683 cm^{-1} is absent in the control active layer but is detected in the films prepared with C-PYR. This suggests that, after spin-casting, residual C-PYR is present in the active layer. When the film is placed under vacuum, the intensity of the absorption peak at 1683 cm^{-1} decreases and is almost not detectable anymore. Therefore, the vacuum is effective in reducing the amount of C-PYR in the active layer.

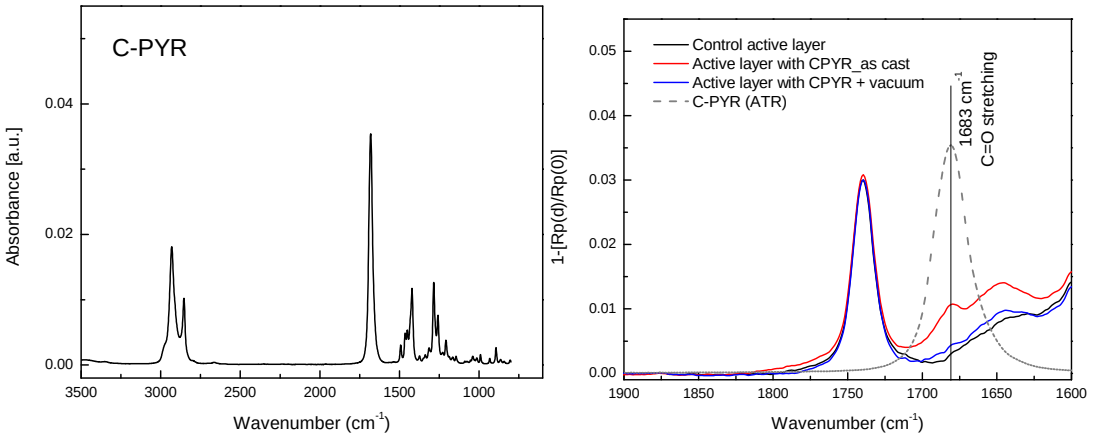

Figure 7.4: (a) ATR spectrum of C-PYR, (b) Zoomed-in PM-IRRAS spectra of P3HT/PC_{61}BM films with and without C-PYR (region 1900 - 1600 cm^{-1}).

- PM-IRRAS spectra of DPH-treated active layers

The ATR spectrum of DPH (Figure 7.5a) presents no absorption peak that can be clearly discriminated from the PM-IRRAS absorption spectra of P3HT/PC_{61}BM films (Figure 7.5b). However, the absorption peak corresponding to the C=O in DPH appears at lower wavelength compared to the C=O peak in P3HT/PC_{61}BM films. This difference causes a broadening of the peak in DPH-treated active layers (Figure 7.5b). In the spectrum of the control active layer, the FWHM of this peak is 17.1 cm^{-1} and it increases up to 19.6 cm^{-1} for DPH-treated films. This suggests that there is a contribution of the C=O from DPH that is remaining in the active layer. The vacuum step reduces the FWHM to 17.7 cm^{-1}. This shows that the vacuum step is effective in removing DPH, but traces of it are still detectable in the active layer.

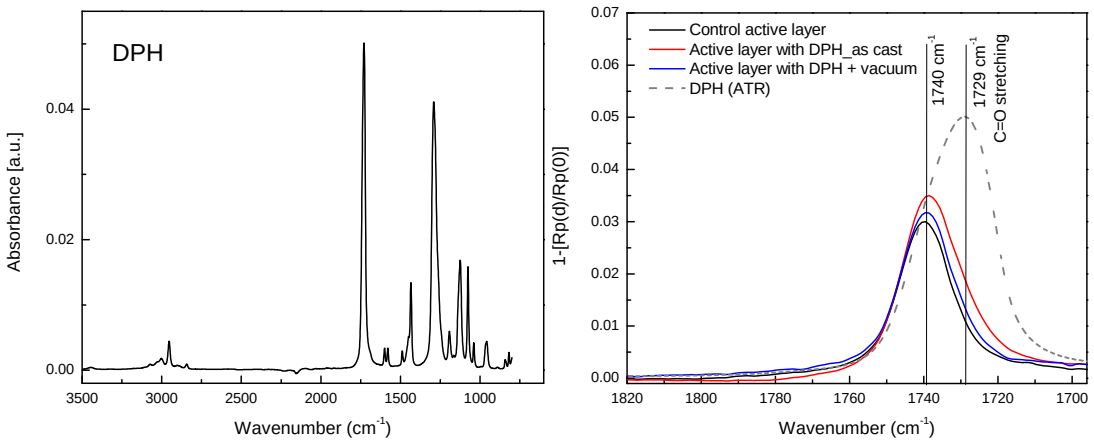

(a) (b)

Figure 7.5: (a) ATR spectrum of DPH, (b) Zoomed-in PM-IRRAS spectra of P3HT/$PC_{61}BM$ films with and without DPH (region 1820 - 1700 cm^{-1}).

- PM-IRRAS spectra of TRIB-treated active layers

As depicted in the ATR spectrum of TRIB in Figure 7.6a, the additive exhibits an intense absorption peak at 1740 cm^{-1}, which remains visible in the PM-IRRAS spectra of TRIB-treated films (Figure 7.6b). In the active layer prepared with TRIB, the intensity of the peak at 1740 cm^{-1} is four times more intense than in a control film. The vacuum step reduces the intensity to 41% of the original signal before the vacuum step. Other peaks characteristic for the ATR spectrum of TRIB (at 959 cm^{-1} and 1076 cm^{-1}) appear in films prepared with TRIB. The intensity of these peaks decreases after the vacuum step. To conclude, TRIB remains in P3HT/$PC_{61}BM$ film after spin-casting and after the vacuum step.

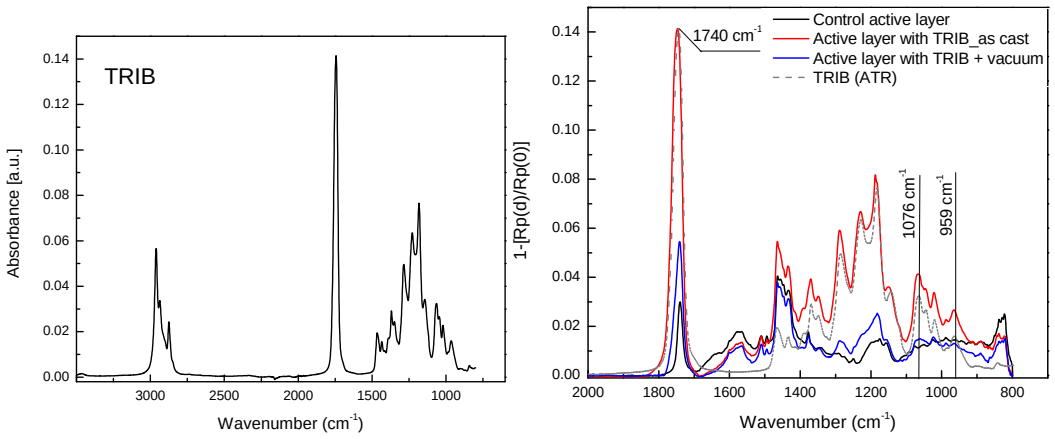

(a) (b)

Figure 7.6: (a) ATR spectrum of TRIB, (b) Zoomed-in spectra of the region 1800 - 1700 cm^{-1} of PM-IRRAS spectra of P3HT/PC_{61}BM films with and without TRIB.

- PM-IRRAS spectra of ODT-treated active layers

The peak at 2560 cm^{-1} in the ATR spectrum of ODT, attributed to S-H, is absent in the PM-IRRAS spectra of ODT-treated films shown in Figure 7.7. Overall, as cast-films and films placed under vacuum prepared from ODT show no significant difference compared to films prepared without additive. This observation suggest that the amount of residual ODT in P3HT/PC_{61}BM-films is negligeable.

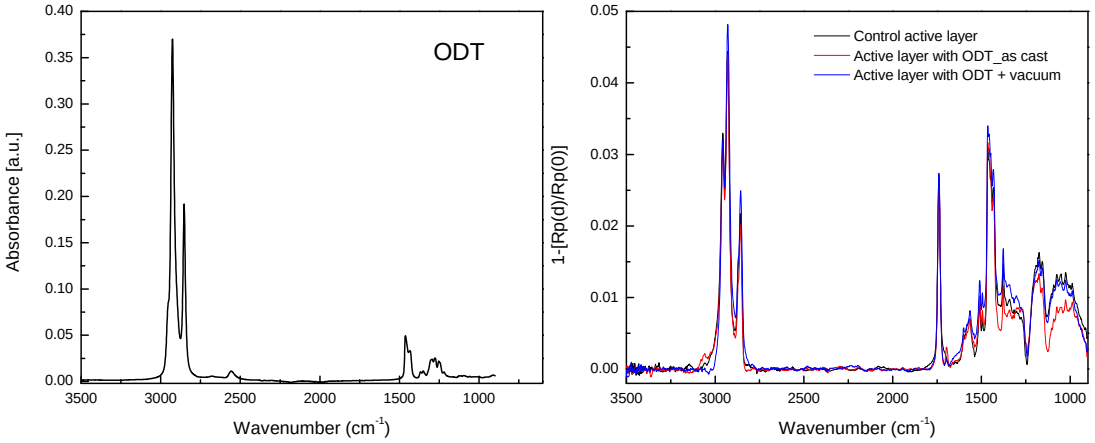

(a) (b)

Figure 7.7: (a) ATR spectrum of ODT, (b) PM-IRRAS spectra of P3HT/PC_{61}BM films with and without ODT.

To conclude, the vacuum step was shown to be effective in reducing the amount of additive in as-cast films. Traces of DPH and TRIB are detected in the active layer even after the vacuum step while C-PYR and ODT are not.

7.3 Photo-stability tests on OSCs

7.3.1 Photo-stability tests on OSCs in air

Photo-stability tests are performed on OSCs prepared with different types of active layers. Table 7.1 gives the initial photovoltaic performances (i.e. at t=0) of the OSCs under study. Attention was paid to fabricate OSCs with similar efficiencies (between 2.6% and 3.0%) in order to allow for comparison between them to yield accurate conclusions.

Table 7.1: Initial electrical performances of OSCs with different types of active layer.

Initial values	Thermal annealing	C-PYR	DPH	ODT
J_{sc}	9.2	9.2	8.7	8.9
[mA.cm^{-2}]	±0.6	±0.4	±0.7	±0.6
V_{oc}	0.56	0.53	0.52	0.50
[V]	±0.03	±0.02	±0.01	±0.02
FF	0.58	0.62	0.66	0.59
	±0.03	±0.06	±0.02	±0.03
PCE	2.6	3.0	3.0	2.6
[%]	±0.4	±0.4	±0.3	±0.2
R_s	4.4	2.5	1.4	3.9
[Ohm.cm^2]	±2.3	±1.7	±0.4	±1.3
R_{sh}	8008	8460	8356	7192
[Ohm.cm^2]	±1771	±2268	±1680	±1987

The OSCs are prepared and exposed to light irradiation in air. OSCs containing processing additives are exposed to light irradiation for a period of 252 hours while thermally annealed OSCs are exposed for only 90 hours because of the low performance obtained after this period. The J-V curves were measured at several intervals within the duration of the light irradiation. Table 7.2 indicates the normalized electrical parameters of OSCs after light irradiation and Figure 7.8 depicts the evolution of the photovoltaic parameters as a function of irradiation time. The normalized parameters

correspond to the percentage of initial value (at t=0) measured before the prolonged light exposure.

Table 7.2: Normalized electrical performance after light irradiation in air: 252 hours of light irradiation for OSCs with processing additives, 90 hours for thermally annealed OSCs.

Normalized values [%]	Thermal annealing	C-PYR	DPH	ODT
J_{sc}	49.1	63.2	59.4	85.7
V_{oc}	16.7	55.3	48.3	81.5
FF	22.3	33.2	13.0	51.8
PCE	1.8	11.8	3.7	36.2
R_s	153.8	1168.8	2642.7	297.3
R_{sh}	6.4	34.1	60.7	77.0

For all OSCs, the FF is the parameter that is the most impacted by the degradation. The decrease in FF is likely to be linked to the significant increase in R_s upon light irradiation. The increase in R_s suggests either an increase in the internal resistance of the active layer or an increase in the resistance at the contacts.

The photo-stability of OSCs differs significantly as a function of the active layer processing conditions. The thermally annealed OSC is the least photo-stable with a PCE of 1.8% of the initial value after 90 hours of light irradiation. On the other hand, ODT-treated OSCs present the best photo-stability with a PCE remaining at 36.2% of the initial value after 292 hours of light irradiation. The most striking difference between thermally annealed and ODT-treated OSC is the V_{oc}. For thermally annealed OSCs, the V_{oc} decreases significantly with increasing irradiation time, whereas ODT-treated OSCs demonstrate less than 15% loss in V_{oc} after the total irradiation time. OSCs with C-PYR and DPH-treated active layers present intermediate stabilities as depicted in Figure 7.8.

7.3.2 Photo-stability tests on OSCs in inert atmosphere

OSCs prepared in conditions identical to those previously described are fabricated and irradiated for a period of 393 hours in inert atmosphere. The J-V curves were measured

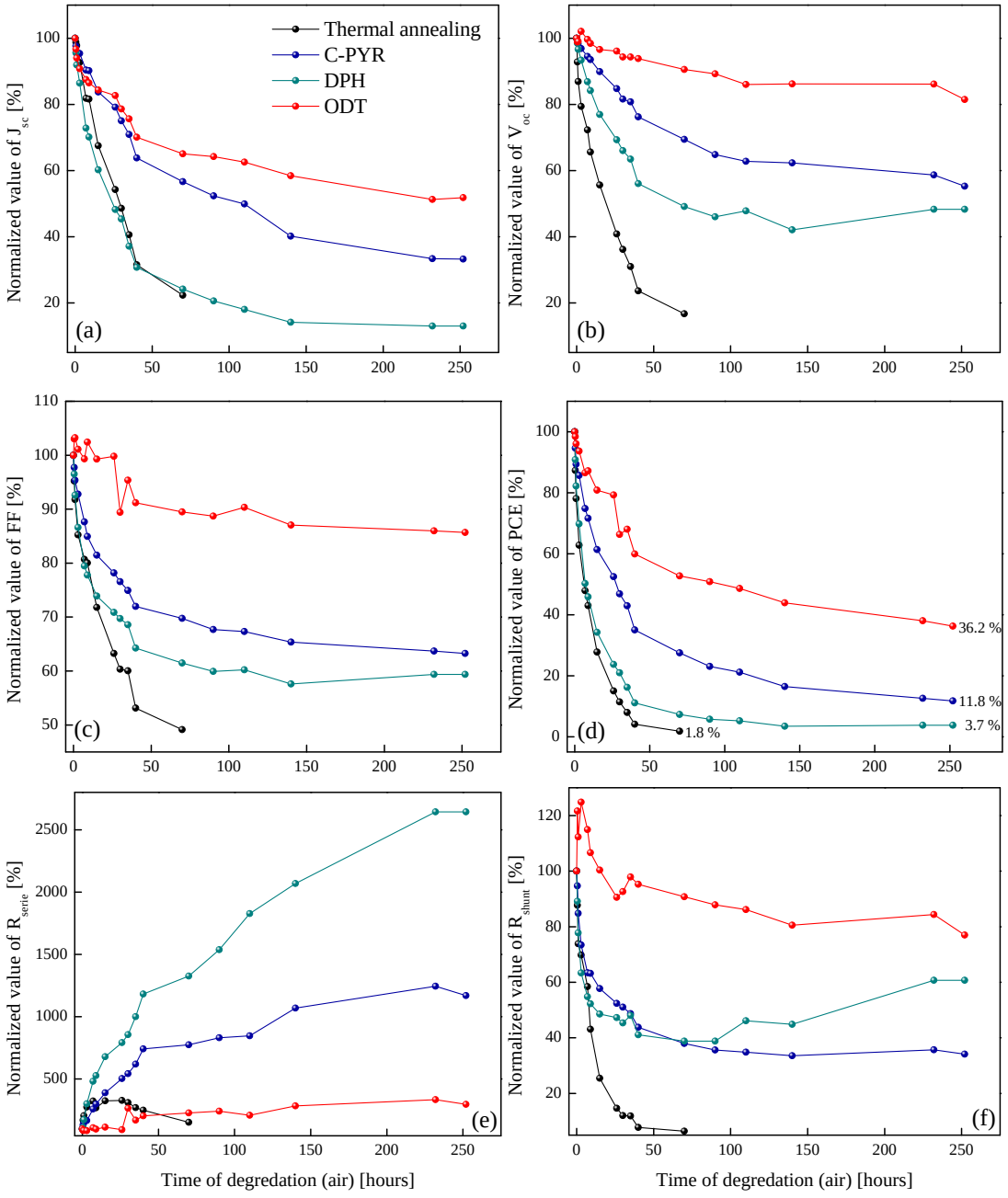

Figure 7.8: Normalized electrical parameters of OSCs subjected to light irradiation in air: (a) J_{sc}, (b) V_{oc}, (c) FF, (d) PCE, (e) R_s and (f) R_{sh}.

at several intervals within the duration of the light irradiation. Table 7.3 reports the normalized photovoltaic parameters of OSCs after 393 hours of light irradiation and Figure 7.9 depicts the evolution of the photovoltaic parameters as a function of the time of light irradiation.

The results depicted in Figure 7.9 show that OSCs photo-stability in inert atmosphere

Table 7.3: Normalized photovoltaic parameters of OSCs after 393 hours of light irradiation in inert atmosphere.

Normalized value [%]	Thermal annealing	C-PYR	DPH	ODT
J_{sc}	75.4	66.8	67.9	78.9
V_{oc}	79.2	91.6	78.3	95.6
FF	52.9	73.7	67.2	94.4
PCE	32.0	44.9	36.0	71.2
R_s	128.2	145.1	402.2	119.1
R_{sh}	33.9	52.8	50.0	77.3

is significantly higher than that in air. This is expected as the inert atmosphere substantially reduces degradation due to photo-oxidation. Interestingly, the dependence of the photo-stability on the processing conditions follows the same trend as observed in air: thermally annealed OSCs exhibit the poorest photo-stability whereas ODT-treated OSCs exhibit the highest photo-stability. OSCs with C-PYR and DPH exhibit intermediate stabilities. Similarly, the V_{oc} is the most discriminant parameter: the thermally annealed OSC has its V_{oc} reduced to 79.2% after 393 hours of light irradiation, whereas the V_{oc} of ODT-treated OSC remains almost unchanged (less than 5 % decrease from the initial value). Along the same line, the decrease in FF is the most significant in thermally-annealed OSC, whereas irradiated ODT-treated OSC demonstrate a FF maintained at 94.4% of the initial value after the total irradiation time. Overall, ODT-treated OSCs are the most photo-stable OSCs with a final PCE of 71.2% of the initial value while the PCE of thermally annealed OSCs is reduced to 32.0% of the initial value.

To conclude, in air and in inert atmosphere, processing conditions have an influence on the photo-stability of OSCs. It is noteworthy to remind here that DPH-treated active layers were shown to retain some additive. However the photo-stability tests show that DPH-treated OSCs have a higher stability than thermally annealed OSCs. This suggests that the remaining additive does not play a major role in OSC photo-degradation.

The following sections aim at identifying the origins of the photo-stability dependence on the processing conditions.

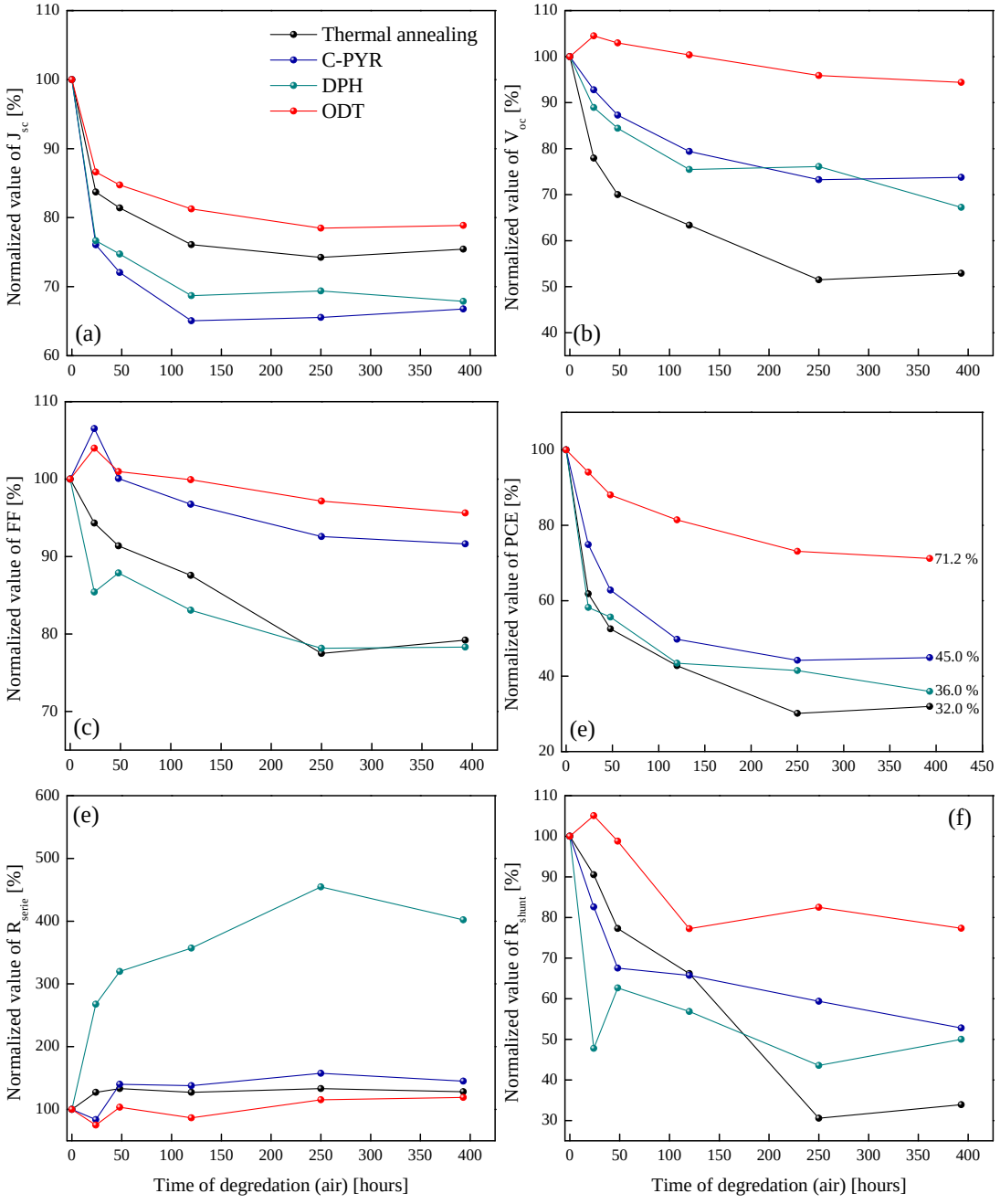

Figure 7.9: Normalized electrical parameters of OSCs subjected to light irradiation in inert atmosphere: (a) J_{sc}, (b) V_{oc}, (c) FF, (d) PCE, (e) R_s and (f) R_{sh}.

7.4 UV-Vis absorption spectroscopy of light-irradiated active layers

To investigate the effects of light irradiation on the optical properties of P3HT/$PC_{61}BM$-films, the UV-Vis absorption spectra of active layer films were measured after being subjected to light irradiation for 60 hours in air. The spectra are shown in Figure 7.10.

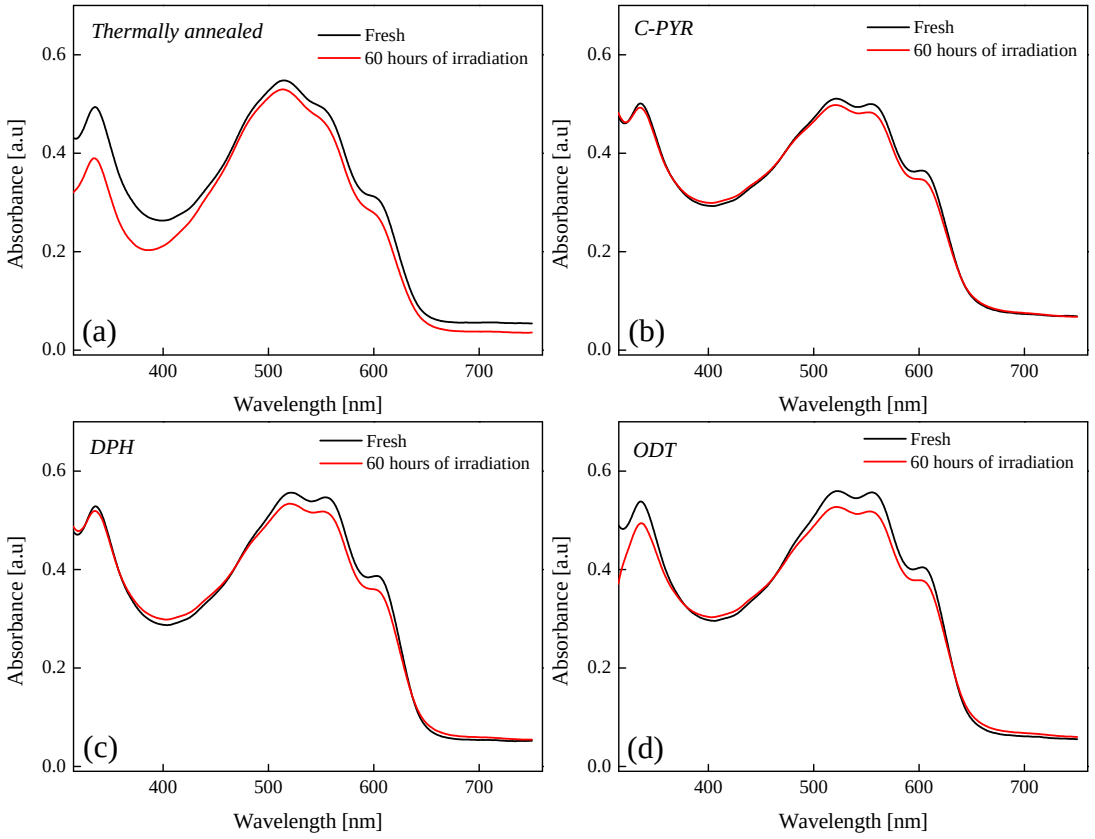

Figure 7.10: UV-Vis absorption of P3HT/$PC_{61}BM$ films before and after light irradiation for 60 hours in air for (a) Thermally annealed, (b) C-PYR, (c) DPH and (d) ODT-treated active layers.

In air, the intensity of the absorption band of P3HT decreases after light irradiation for all the types of active layers, indicating that photo-oxidation of P3HT occurs in all cases. The loss in optical density at 601 nm is calculated and recorded in Table 7.4.

The decrease in optical density of ODT-treated active layers appears to be in the same range as that of C-PYR and DPH-treated active layers. The higher photo-stability of ODT-treated OSCs seems therefore to be independent of the optical density losses associated with photo-bleaching.

Table 7.4: Decrease in optical density measured at 601 nm.

Types of active layers	Loss in optical density [%]
Thermally annealed	11.0
C-PYR	4.8
DPH	7.0
ODT	6.4

The UV-Vis absorption spectra of light-irradiated active layers in inert atmosphere are depicted in Figure 7.11.

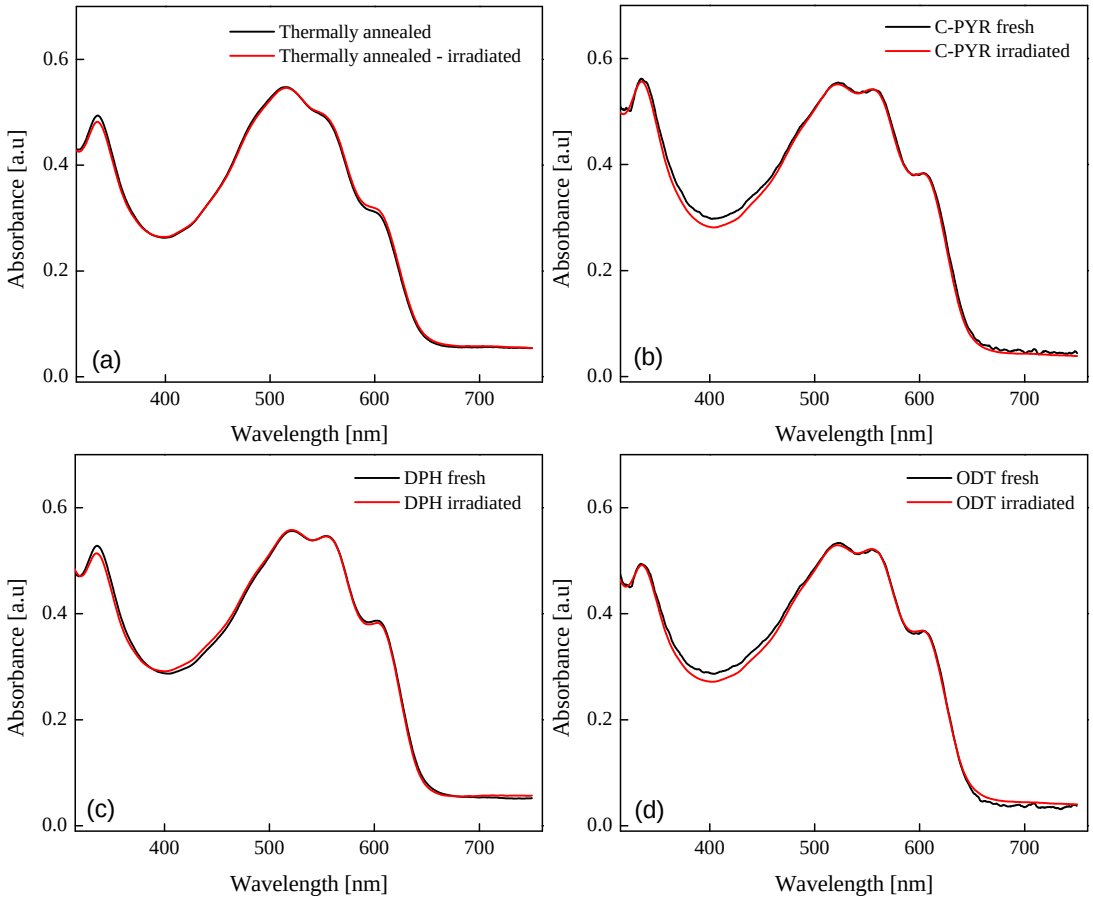

Figure 7.11: UV-Vis absorption spectra of P3HT/$PC_{61}BM$ films before and after light irradiation for 60 hours in inert atmosphere for (a) Thermally annealed, (b) C-PYR, (c) DPH and (d) ODT-treated active layers.

In inert atmosphere, the absorption spectra do not exhibit significant change after 60

hours of light irradiation indicating that the π-conjugated system as well as the chemical structure of P3HT are not affected by light irradiation. This confirms that OSC photo-degradation in inert atmosphere does not arise from chemical photo-degradation of P3HT.

The results in UV-Vis absorption spectroscopy do not explain the dependence of OSC photo-stability on processing conditions. Besides, the presence of traces of additive does not explain it neither. These two results suggest that the major origin of the photo-degradation is not the active layer. Therefore, the degradation at the interfaces (between the active layer and the top electrode or the bottom electrode) are investigated. As the trends in photo-stability are similar in air and in inert atmosphere, the following studies are carried out in inert atmosphere only.

7.5 Photo-stability study on the bottom interface

Photo-stability tests are carried out on OSCs containing a buffer interlayer which makes the bottom interface independent from the active layer processing conditions. The objective here is to verify if the photo-stability dependence on the processing conditions remains identical after the insertion of the buffer interlayer. To this end, a layer of C_{60} is introduced as an interlayer between ZnO and the active layer as depicted in Figure 7.12.

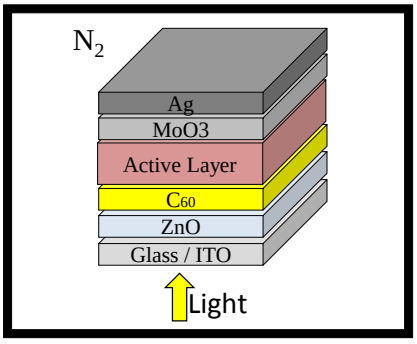

Figure 7.12: Scheme of photo-stability tests on OSC with a C_{60} buffer interlayer.

The energy level diagram, shown in Figure 7.13, suggests that a C_{60} interlayer introduces a small energy barrier (0.4 eV) to the transport of electrons from the active layer to the ZnO layer. Therefore, the photovoltaic performance of OSCs with a C_{60} interlayer needs to be optimized.

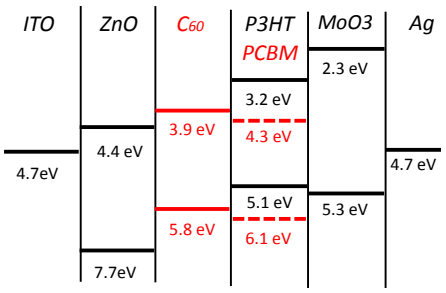

Figure 7.13: Energy levels of OSCs containing C_{60} as an interlayer between ZnO and the active layer.

A series of OSCs containing C_{60} interlayers with different thicknesses are fabricated. Figure 7.14 depicts the evolution of the PCEs as a function of the thickness of C_{60}. The results show that a C_{60} interlayer with a thickness $\leq$ 10 nm does not alter significantly the PCE of the different types of OSCs whereas 20 nm of C_{60} decreases the PCE of thermally annealed OSC. This decrease is attributed to structural changes in the interlayer caused by the thermal annealing step. As the introduction of a C_{60} interlayer with a thickness $\leq$ 10 nm does not affect the photovoltaic performance of OSCs, they are suitable to be used for photo-stability tests.

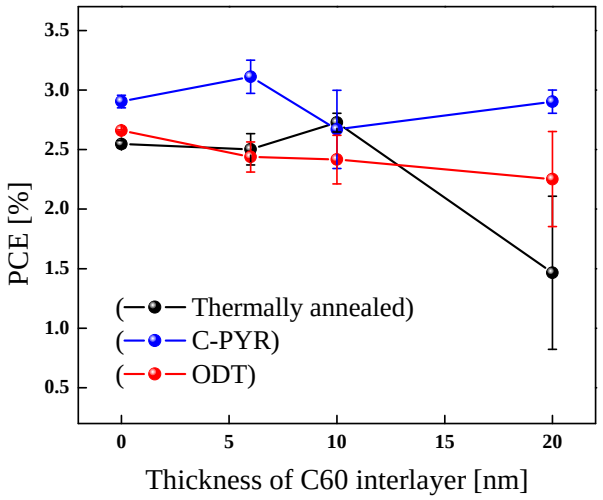

Figure 7.14: Effects of C_{60} thickness on the PCE of OSCs.

Photo-degradation tests in inert atmosphere are performed on OSCs containing a 10 nm interlayer of C_{60}. The OSCs are irradiated for 390 hours and the J-V characteristics are measured at several intervals within the duration of light irradiation. Figure 7.15

depicts the evolution of PCE and V_{oc} as a function of the time of light irradiation for OSCs containing or not a C_{60} interlayer.

The results show that regardless of the type of processing conditions, OSCs containing a C_{60} interlayer photo-degrade following the same trend as OSCs without interlayer. The unchanged trend in photo-stability indicates that the changes in photo-stability are not due to variations at the bottom contact caused by the processing additives.

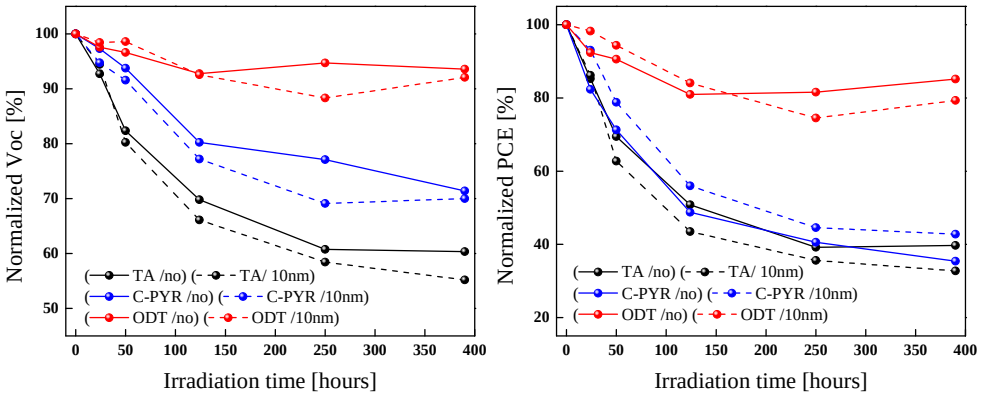

Figure 7.15: Evolution of normalized (a) V_{oc} and (b) PCE as a function of irradiation time for OSCs without (solid line) and with (dashed line) a C_{60} interlayer.

7.6 Photo-stability study on the top interface

7.6.1 Photo-stability tests on OSC active layers

In order to investigate the role of the top interface (i.e. the interface between the active layer and MoO_3/Silver), photo-degradation tests in inert conditions are performed on samples that contain a stack of ITO/ZnO/Active layer only, refer to as incomplete OSCs. The incomplete OSCs are light-irradiated in inert atmosphere for 40 hours and then the fabrication is completed by the thermal evaporation of MoO_3/Silver after that. The photovoltaic performances are measured and compared to those of fresh OSCs. The normalized PCEs are reported in Table 7.5.

OSCs with ODT present a slight increase in J_{sc}, V_{oc} and PCE. The increase in these parameters can be attributed to external parameters such as the increase in the work function of silver or internal parameters such as changes in the ZnO layer upon light

irradiation. In this experiment, ODT-treated OSCs remain the most photo-stable. On the other hand, the photo-stability of OSCs with DPH, C-PYR and which are thermally annealed all exhibit similar performance loss: their PCEs decrease to around 80% of their initial values after 40 hours of light irradiation. This is in contrast with the trends observed in the photo-stability tests of complete OSCs shown earlier in sections 7.3.1 and 7.3.2 in which the stabilities were different.

Table 7.5: Normalized photovoltaic performance of C-PYR, DPH and ODT-treated OSCs and thermally annealed OSCs subjected to light irradiation in inert atmosphere for 40 hours.

	Normalized parameters [%]					
Types of OSCs	J_{sc}	V_{oc}	FF	PCE	R_s	R_{sh}
Thermally annealed	86.3	93.3	88.6	82.8	164.4	111.1
C-PYR	93.4	95.7	92.8	83.0	202.1	48.3
DPH	100.8	92.3	83.6	78.5	333.6	58.2
ODT	109.0	101.1	94.5	104.4	153.0	71.3

The photovoltaic parameters of OSCs subjected to photo-degradation in the complete or incomplete way are compared to identify the role of the top electrode in photo-degradation. The normalized photovoltaic performances are compared after 40 hours of light irradiation (for the tests performed on complete OSCs, the electrical performances were determined by the extrapolation of the trends in Figure 7.9 at 40 hours). The normalized V_{oc} and PCE in the two experiments are shown as a function of the processing conditions in Figure 7.16.

Interestingly, the OSCs subjected to light irradiation without top electrode appear to be more stable than the OSCs irradiated with the top electrode. In the photo-degradation tests on complete OSCs, the V_{oc} is the parameter that discriminates the most the different types of processing conditions, whereas in the tests on incomplete OSCs, the V_{oc} remains relatively similar for all the types of active layers. Two conclusions can be drawn:

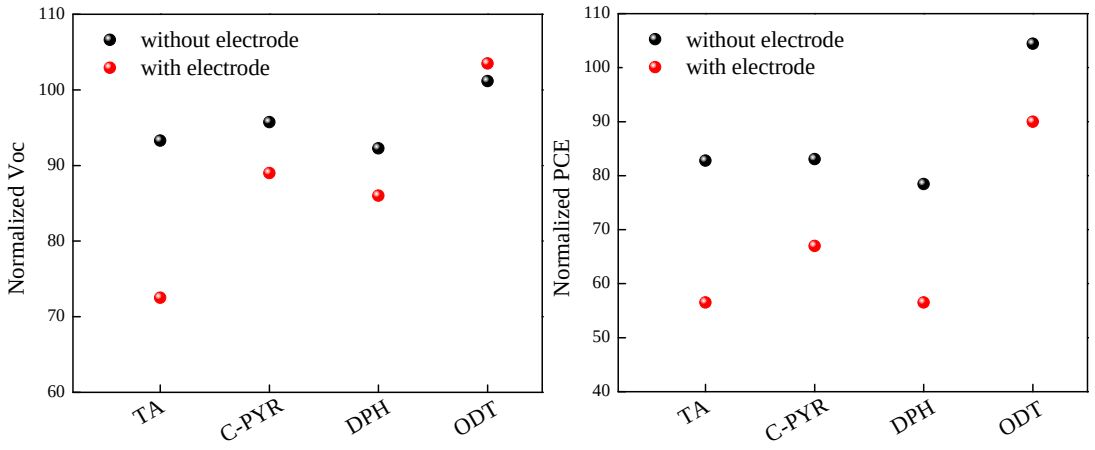

Figure 7.16: Comparison of the normalized (a) V_{oc} and (b) PCE after 40 hours of light irradiation on OSCs without top electrode or with top electrode.

1. The higher photo-stability of incomplete OSCs versus complete OSCs suggests that the presence of a top electrode plays a role in the photo-degradation.

2. The fact that the photo-stability of incomplete OSCs is less dependent on the processing conditions than in the case of complete OSCs suggests that the processing conditions affect the photo-stability at the top interface.

Therefore, further investigations are performed on the photo-stability of the top interface.

7.6.2 Effects of light irradiation on the adhesion of the top electrode

Wang et al. demonstrated that light irradiation of an organic/metal stack caused deterioration at the interface by decreasing metal-organic bond density in organic light emitting diodes [220]. This photochemical deterioration at the interface caused a decrease in interfacial adhesion between the metal and the organic layer. In order to investigate the degradation in OSCs at the top electrode, interfacial adhesion measurements are carried out on OSC stacks before and after light irradiation. The adhesion energy at the interface between the active layer and the top contact is measured using a four-point bending test configuration [14, 220]. During the adhesion experiment, a load is applied on the two sides of the sample under study. The load as a function of the displacement is recorded and a typical displacement plot is shown in Figure 7.17. The adhesion is the energy required to cause delamination at the interface between

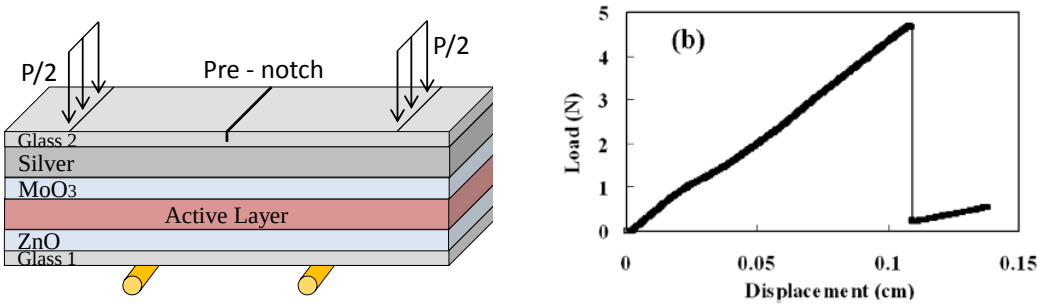

(a) (b)

Figure 7.17: (a) Schematic drawing of a four-point bend adhesion sample stack. A load P/2 is applied on each side of the sample. (b) A typical load versus displacement characteristic. Figure (b) is reproduced from reference [220] with permission of AIL Publishing LLC.

two layers. Generally, the load first increases linearly with the displacement, which is characteristic for an elastic deformation. If a weak interface is present in the stack, a crack initiated by a pre-notch propagates along the interface. Such propagation causes a release of energy which can be related to the interfacial adhesion strength, G_c expressed as:

$$G_c = \frac{21(1-\nu^2)P^2l^2}{16Eb^2h^3} \tag{7.1}$$

With ν the Poisson's ratio of the glass substrate, E is the elastic modulus of the substrate, P the total force exerted onto the sample, b, h and l geometrical characteristics of the sample and the setup.

The OSC stack configuration is prepared on a rectangular glass substrate (1 cm x 5 cm) in order to be suitable for the four point bending test (Figure 7.17). A second glass substrate is glued on top of the stack and a pre-notch is made on it. During the adhesion measurement test, equal loads are applied on both side of the sample. The loads deform the sample at a constant velocity of 0.25 μm.s^{-1} while the load as a function of the sample displacement is recorded. The adhesion measurement tests are performed on the two OSCs that exhibit the most differences in photo-stability: the thermally annealed and ODT-treated OSCs. Figure 7.18 shows the load versus displacement plots obtained.

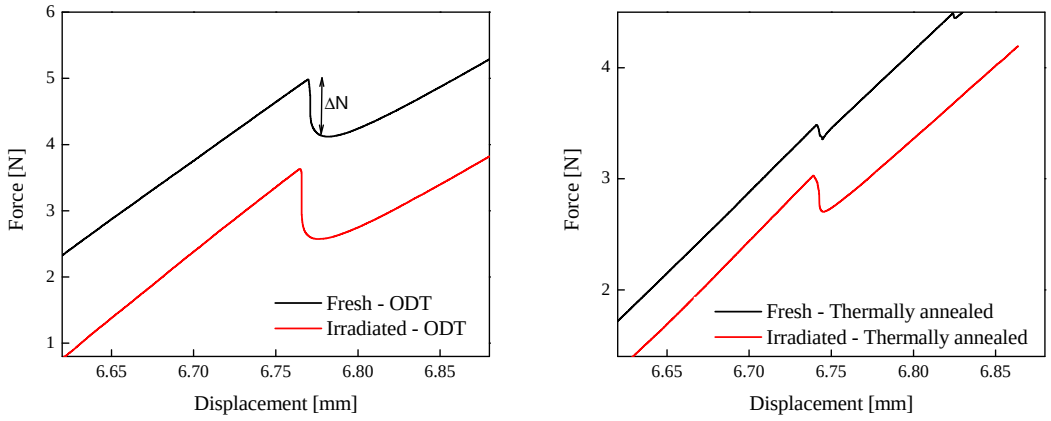

Figure 7.18: Load versus displacement characteristics for fresh and irradiated samples for (a) samples with ODT and (b) thermally annealed samples. On (a) the measured force loss (ΔN) is showed. The plots of the irradiated samples were manually vertically down shifted for the clarity of the Figures.

The two samples demonstrate the same evolution: first, the load increases linearly with the displacement and when the displacement reaches 6 to 7 mm, a slight load drop is observed, followed by a linear increase in the load. Ultimately, for higher displacement values, the samples are broken. In case of complete delamination, a complete load drop would be observed (as depicted in Figure 7.17). In Figure 7.18, the plots show that no total delamination occurs. Instead, a small load drop is observed, suggesting that a crack propagates only slightly in the interface without fully delaminating it. At higher load values, the cracks continue to penetrate vertically throughout the stack and ultimately break the entire sample. As no total delamination occurs, the interface adhesion strength cannot be calculated using Equation 7.1. Instead, the load loss during the partial delamination (ΔN) is determined (ΔN is depicted in Figure 7.18). This load loss is related to the energy released during the partial delamination and therefore describes how far the delamination propagates at the interface. Table 7.6 and Table 7.7 show the load loss values before and after degradation for thermally annealed and ODT-treated OSCs respectively. The values represent the average of two samples (except for the case of irradiated OSCs with ODT).

Table 7.6: Force loss in the adhesion measurement test of thermally annealed samples.

	ΔN [N]		
	Sample 1	Sample 2	Average
Fresh - TA	0.18	0.13	0.16
Irradiated - TA	0.33	0.23	0.28
Percentage increase		76.8 %	

Table 7.7: Force loss in the adhesion measurement test of ODT-treated samples.

	ΔN [N]		
	Sample 1	Sample 2	Average
Fresh - ODT	0.86	0.59	0.73
Irradiated - ODT	1.06	-	1.06[a]
Percentage increase		46.0 %	

[a] The average takes into consideration the result of Sample 1 only.

Several observations and conclusions can be deduced form the results:

1. Regarding only fresh samples, the load loss in ODT-treated samples (0.73 N) is higher than the load loss in thermally annealed samples (0.16 N). This indicates that the interfacial adhesion is dependent on the processing conditions of the active layer. The AFM images of P3HT/$PC_{61}BM$-films treated with ODT and thermal annealed are recorded and depicted in Figure 7.19. The roughness measurement show that film treated with ODT presents a higher roughness than thermally annealed films. The difference in surface topography are likely the cause of the differences observed in the adhesion tests.

2. The load loss in photo-degraded OSCs is larger than that observed in fresh OSCs indicating that the interfacial delamination is more severe in photo-degraded OSCs. This, in turn, strongly suggests that the light irradiation affects the OSCs at the top interface by weakening the interfacial adhesion.

3. The percentage of load loss increase in thermally annealed samples is calculated to be 76.8%, whereas in ODT-samples, the increase is only 46.0%. This suggests that the interfacial adhesion is more severely deteriorated in the case of thermally annealed samples.

Table 7.8: Roughness of active layers with different processing additives.

	Thermally annealed	1.6 vol% of ODT
Roughness [nm]	1.4	7.9

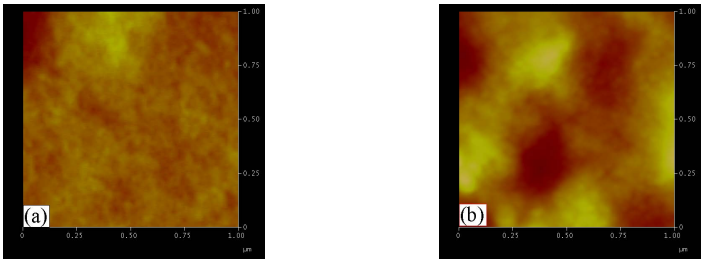

Figure 7.19: AFM topography (1 μm x 1 μm) images of active layers films: (a) thermally annealed and (b) ODT-treated.

7.7 Conclusions

In this chapter, the effects of thermal annealing and the use of additive on the stability of OSCs are investigated. The main finding of this chapter is the OSC photo-stability dependence on the active layer processing conditions, a result which is valid for photo-degradation in both inert atmosphere as well as in air. The best photo-stability is obtained with ODT-treated OSCs, followed by C-PYR and DPH-treated OSCs as intermediates, and thermally annealed OSCs as the least stable devices.

The photo-degradation is shown to be unrelated to the remaining traces of additive in the active layer and to chemical degradation in the active layer. Instead, the photo-stability tests presented in Sections 7.5 and 7.6.1 suggest that the photo-degradation occurs primarily at the top interface. By means of adhesion measurements it is confirmed that light irradiation causes interfacial degradation which results in a weaker adhesion of the top electrode upon light irradiation. These results suggest that the increased in R_s observed in the photo-stability tests (in Sections 7.3.2 and 7.3.1) is due to increased contact resistance at the top electrode, which in turn decrease the V_{oc} by affecting the built-in voltage in the device. Additionally, adhesion measurements show that ODT-treated OSCs are in a lower extend subjected to interfacial photo-degradation than thermally annealed OSCs. This is consistent with the fact that the photo-stability of ODT-treated OSCs is better than thermally annealed OSCs.

Overall, processing additives are not detrimental for the photo-stability of OSCs compared to thermally annealed OSCs. In the specific case of ODT, the photo-stability is

even improved. This shows that next to improving the efficiency, additives can also be employed to improve the photo-stability.

Chapter 8

Studies on new generation donor polymers

As suggested in Chapter 2, the selection and the effects of processing additives depend on the type of D/A systems. In order to broaden the scope of the study on processing additive, other types of D semiconductors are investigated. P3HT can be classified as a low mobility semi-crystallline polymer. In this chapter, two other families of D are studied: a high mobility semi-crystalline polymer (a 1,4-diketopyrrolo[3,4-c]pyrrole derivative with a quaterthiophene substituent (PDQT)) and an amorphous polymer (poly[N-9'-heptadecanyl-2,7-carbazole-alt-5,5-(4',7'-di-2-thienyl-2',1',3'-benzothiadiazole (PCDTBT)).

8.1 Studies on PDQT

8.1.1 Introduction to DPP based copolymers

In the past few years, 1,4-diketopyrrolo[3,4-c]pyrrole (DPP) has attracted considerable attention as an electron acceptor building block in conjugated copolymers for applications in OTFTs [118] and OSCs [79–81, 119–121]. The general chemical structure of DPP-based copolymers, depicted in Figure 8.1, contains an alternation of electron donating and DPP building blocks.

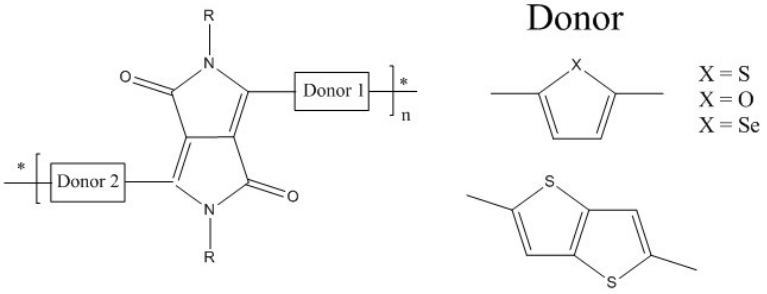

Figure 8.1: On the left: DPP-based conjugated polymers where R is a substituent, Donor 1 and Donor 2 are electron donating building blocks. On the right, examples of electron donating building blocks are depicted. Adapted from reference [121] with permission of the Royal Society of Chemistry .

The DPP-based copolymer investigated in this work contains a quaterthiophene group as the electron donor to form the PDQT copolymer depicted in Figure 8.2. This copolymer was shown to form films with a high degree of crystallinity due to strong intermolecular π-π stacking. As a result, PDQT was shown to exhibit high hole mobility in OTFT configuration with mobilities up to 0.97 $cm^2.V^{-1}.s^{-1}$ [122, 123]. Another interesting feature of PDQT is its large absorption spectrum which is extended to the

near IR ($\sim$ 950 nm), as depicted in the UV-Vis absorption spectrum of PDQT/$PC_{61}BM$ film in Figure 8.3.

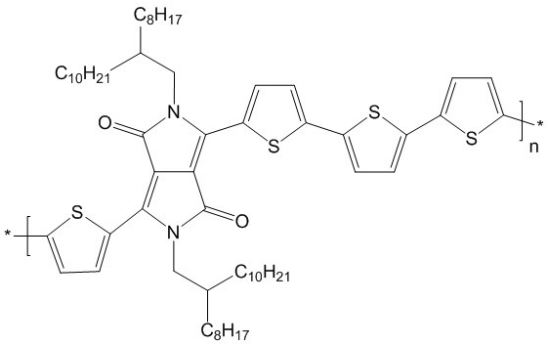

Figure 8.2: Chemical structure of PDQT.

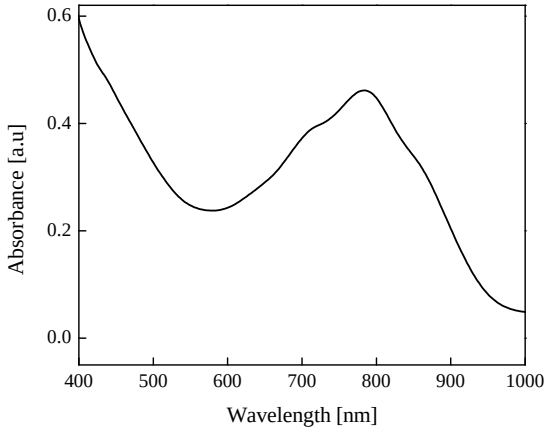

Figure 8.3: Solid-state UV-Vis spectrum of PDQT/$PC_{61}BM$ in a 1/3 ratio.

The HOMO LUMO energy levels of PDQT are estimated to be respectively and 5.3 eV and 4.0 eV respectively [152]. Such a LUMO energy level leads to an energy difference of 0.3 eV with the LUMO of $PC_{61}BM$ and is therefore suitable for efficient charge transfer. The energy diagram of PDQT/$PC_{61}BM$-based OSC is depicted in Figure 8.4.

8.1.2 Performance of OSCs based on PDQT/$PC_{61}BM$

Prior to the fabrication of OSCs, the HSPs of PDQT are determined in order to verify its solubility in conventional solvents such as CB or ODCB.

The HSPs of PDQT have been determined experimentally by performing solubility tests. The HSPs resulting from the fitting are presented in Table 8.1 and the graphical representation of the PDQT solubility sphere is depicted in Figure 8.5.

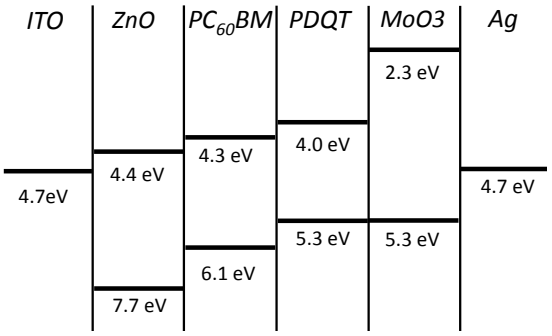

Figure 8.4: Energy levels of PDQT/$PC_{61}BM$ - OSC in an inverted architecture.

Table 8.1: HSPs of PDQT.

	δD [$MPa^{1/2}$]	δP [$MPa^{1/2}$]	δH [$MPa^{1/2}$]	R_O [$MPa^{1/2}$]	FIT
PDQT	18.28	4.11	3.07	3.2	0.860

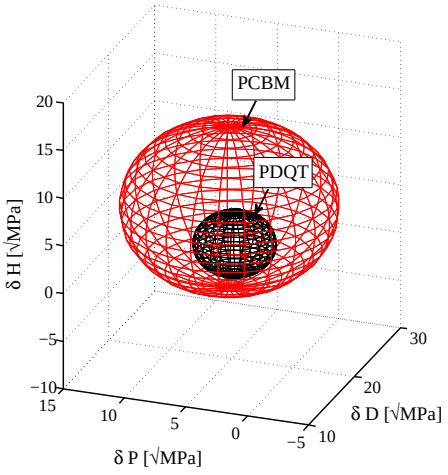

Figure 8.5: Solubility spheres of $PC_{61}BM$ and PDQT.

Using these HSPs, the RED values between PDQT - CB and PDQT - ODCB are calculated and found to be respectively 0.56 and 0.90. These numbers suggest that PDQT is soluble in both solvents. It was shown in the literature, that PDQT-based OSCs can be fabricated with thick active layers (up to $\sim$ 800 nm) [151]. As such active layers are usually obtained from low boiling point solvents, CB is chosen as the host solvent due to its low boiling point (51 °C below that of ODCB) in order to fabricate thick active layer OSC.

PDQT and $PC_{61}BM$ formulations are prepared with a total solid content of 30 $mg.mL^{-1}$

in CB with various D/A ratio (from 1/1 to 1/4) and spin-cast at a spin speed of 800 rpm to form the active layer. Table 8.2 shows the photovoltaic performance of inverted OSCs prepared from various D/A ratios.

Table 8.2: Photovoltaic parameters of OSCs with various ratios of PDQT/$PC_{61}BM$.

D/A ratio	J_{sc} [mA.cm^{-2}]	V_{oc} [V]	FF	PCE [%]	R_s [Ohm.cm^2]	R_{sh} [Ohm.cm^2]
1/4	2.6 ±0.1	0.58 ±0.01	0.51 ±0.01	0.8 ±0.0	14.5 ±1.9	1607 ±263
1/3	3.3 ±0.1	0.60 ±0.00	0.57 ±0.03	1.1 ±0.1	10.1 ±1.7	1698 ±369
1/2	2.8 ±0.1	0.59 ±0.01	0.51 ±0.03	0.8 ±0.0	14.3 ±2.5	1245 ±99
1/1	4.8 ±1.4	0.60 ±0.00	0.42 ±0.07	1.2 ±0.2	13.6 ±0.4	501 ±419
3/1	0.8 ±0.1	0.59 ±0.02	0.50 ±0.07	0.2 ±0.0	78.8 ±33.7	2412 ±624

OSCs with a D/A ratio of 3/1 exhibit a low PCE of 0.24%, mostly due to low J_{sc}. This low J_{sc} is likely to be due to charge transport issues also evident from the high R_s. Overall, the PCEs of OSCs are similar for each D/A ratio, with the exception of the 3/1 one.

XRD measurements are conducted on PDQT/$PC_{61}BM$ - films. The XRD patterns are presented in Figure 8.6. Pure PDQT exhibits a diffraction peak at 4.47° which corresponds to the interlayer spacing $d_{(100)}$ between PDQT chains, suggesting a predominant edge-on orientation of the chains. Table 8.3 presents the angles of the maximum diffraction peak and the crystallite domain sizes estimated with Scherrer's equation for each of the films. For each film, the crystallite domain size is 13 - 14 nm. This result suggests that there is no impact of the proportion of A on the crystallization of PDQT during film formation.

Table 8.3: Diffraction peaks and domain sizes of PDQT/$PC_{61}BM$ with various D/A ratios.

D/A system	2θ [°]	Domain sizes [nm]
Pure PDQT	4.47	14
Ratio 1/1	4.45	13
Ratio 1/2	4.45	14
Ratio 1/3	4.53	13
Ratio 1/4	4.39	14

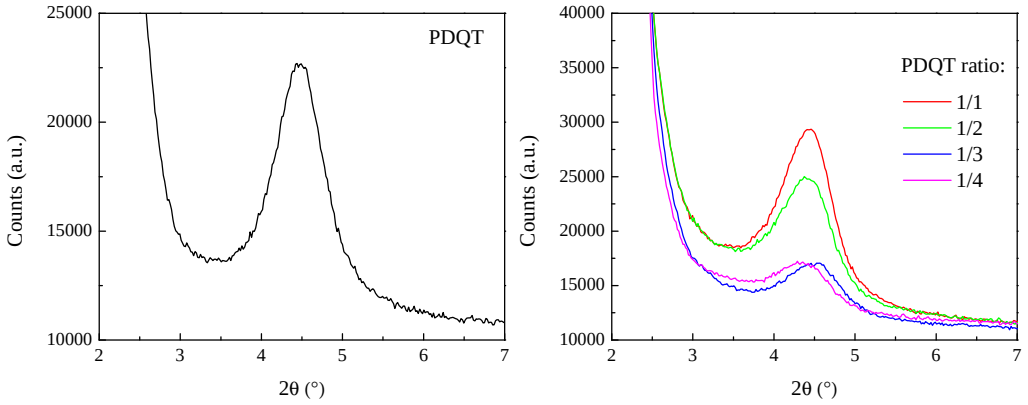

Figure 8.6: XRD patterns of: (a) pure PDQT and (b) PDQT/$PC_{61}BM$ blends in various D/A ratios.

The crystalline structure of PDQT can be observed in the AFM images depicted in Figure 8.7. The phase image of pure PDQT exhibits well defined crystallites that appear to be homogeneous in size and fairly flat as suggested by its low roughness of 1.8 nm. In PDQT/$PC_{61}BM$-films, the phase images show large features, heterogeneous in size, suggesting the coexistence of PDQT crystallites and $PC_{61}BM$ crystallites. The increase in $PC_{61}BM$ proportion also leads to a gradual increase in roughness: the roughness increases from 1.8 nm for pure PDQT to 4.0 nm in blends of PDQT/$PC_{61}BM$ prepared in a 1/4 ratio. The fact that the films present such a heterogeneous distribution of crystallite sizes suggests that PDQT and $PC_{61}BM$ aggregate independently, explaining the non dependence of PDQT crystallite sizes on the proportion of A.

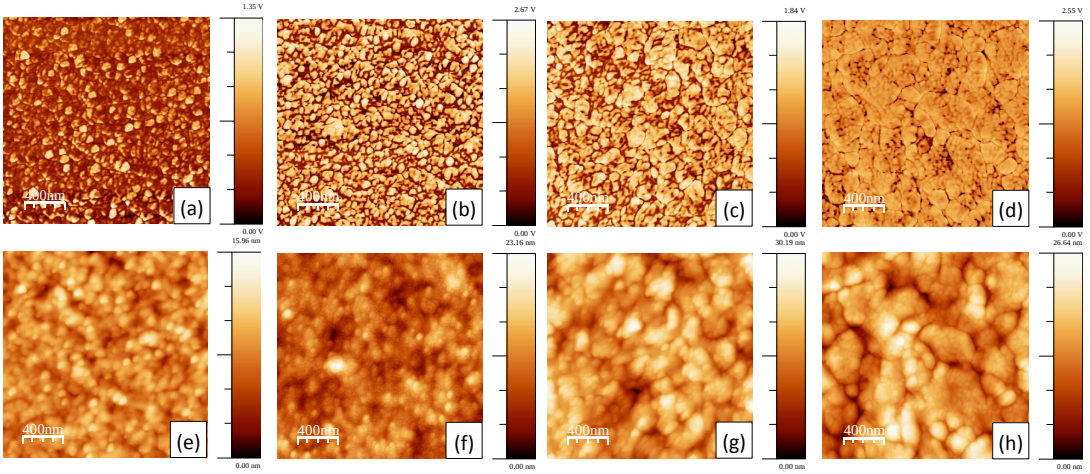

Figure 8.7: AFM images of PDQT/ $PC_{61}BM$ in various D/A ratios: (a-d) phase images, (e-h) topography images: (a) and (e) ratio pure PDQT, (b) and (f) ratio 2/1, (c) and (g) ratio 1/2, (d) and (h) ratio 1/4.

8.1.3 Effects of processing additives

Following the same approach as the one applied to the P3HT/$PC_{61}BM$ system, processing additives are selected under the conditions that they are good solvents for $PC_{61}BM$ and poor solvents for PDQT. Using the HSPs as a numerical tool to determine such solvents, ODT was found to have RED values with PDQT and $PC_{61}BM$ of respectively 1.32 and 0.68. Therefore, ODT is investigated as a processing additive in PDQT/$PC_{61}BM$ - OSCs. DIO is also studied as a processing additive because several studies reported on its success in increasing the efficiency of DPP-based copolymer OSCs [120, 195]. The solubility properties of DIO are similar to the ones of ODT in the sense that PDQT has a lower solubility in DIO than in halogenated solvents [195].

OSCs are fabricated utilizing formulations that contain various concentrations of ODT or DIO. The formulations are prepared from a D/A ratio of 1/3 and a total solid content of 30 mg.mL^{-1}. Figure 8.8 shows the photovoltaic parameters (V_{oc}, J_{sc}, FF and PCE) of the OSCs with the different processing additives and their corresponding concentrations. The best values for each system are recorded in Table 8.4.

Table 8.4: Electrical performance of PDQT/$PC_{61}BM$-OSCs with and without additive.

Type of additive	J_{sc} [mA.cm^{-2}]	V_{oc} [V]	FF	PCE [%]	R_s [Ohm.cm^2]	R_{sh} [Ohm.cm^2]
No additive	4.2 ± 0.3	0.58 ± 0.00	0.62 ± 0.00	1.5 ± 0.1	12.2 ± 0.3	905 ± 43
ODT - 5 vol%	5.8 ± 0.1	0.62 ± 0.00	0.52 ± 0.01	1.9 ± 0.1	10.1 ± 0.5	604 ± 49
DIO - 5 vol%	6.2 ± 0.2	0.58 ± 0.00	0.60 ± 0.02	2.1 ± 0.0	11.7 ± 0.3	1040 ± 241

5 vol% of ODT and DIO increase the PCE by respectively 26% and 46% in comparison to control devices devoid of processing additives, resulting in a PCE of 1.85% in case of ODT and 2.14% in the case of DIO. The main parameter responsible for the increase in PCE is the J_{sc}, similarly to the case of P3HT/$PC_{61}BM$ - OSCs. The J_{sc} increases with additive concentrations up to 5 vol% but decreases at higher concentrations. In contrast to the case of P3HT/$PC_{61}BM$, no significant change in V_{oc} is observed (except for OSCs fabricated with 11 vol% of ODT). This suggests that processing additives do not lead to significant change in the overall crystallinity, certainly because PDQT is already highly crystalline in PDQT/$PC_{61}BM$-films devoid of processing additives.

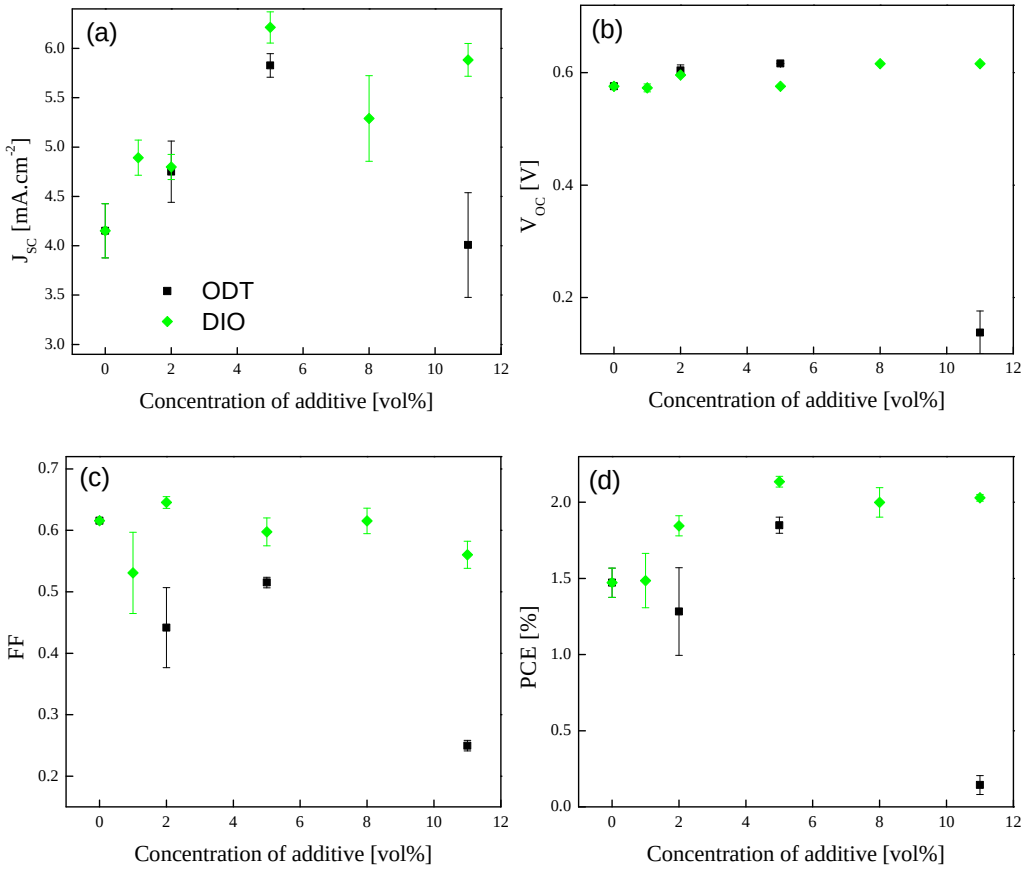

Figure 8.8: Electrical performance of PDQT/PC_{61}BM-OSCs as a function of additive concentration: (a) J_{sc}, (b) V_{oc}, (c) FF and (d) PCE.

XRD measurements are conducted on PDQT/PC_{61}BM-films that contain various concentrations of DIO. The measurement of the crystallite sizes using the Scherrer equation shows that the sizes of PDQT crystallites increase upon the introduction of DIO. Films prepared from 5 vol% and 11 vol% of DIO exhibit crystallite sizes of 19 and 21 nm respectively while PDQT/PC_{61}BM-films devoid of processing additive exhibit a crystallite size of 14 nm. The appearance of large crystallite sizes are in agreement with the features observed in the AFM images of PDQT/PC_{61}BM films depicted in Figure 8.9. Films prepared from 11 vol% of DIO reveal large features which can be attributed to large PDQT crystallites.

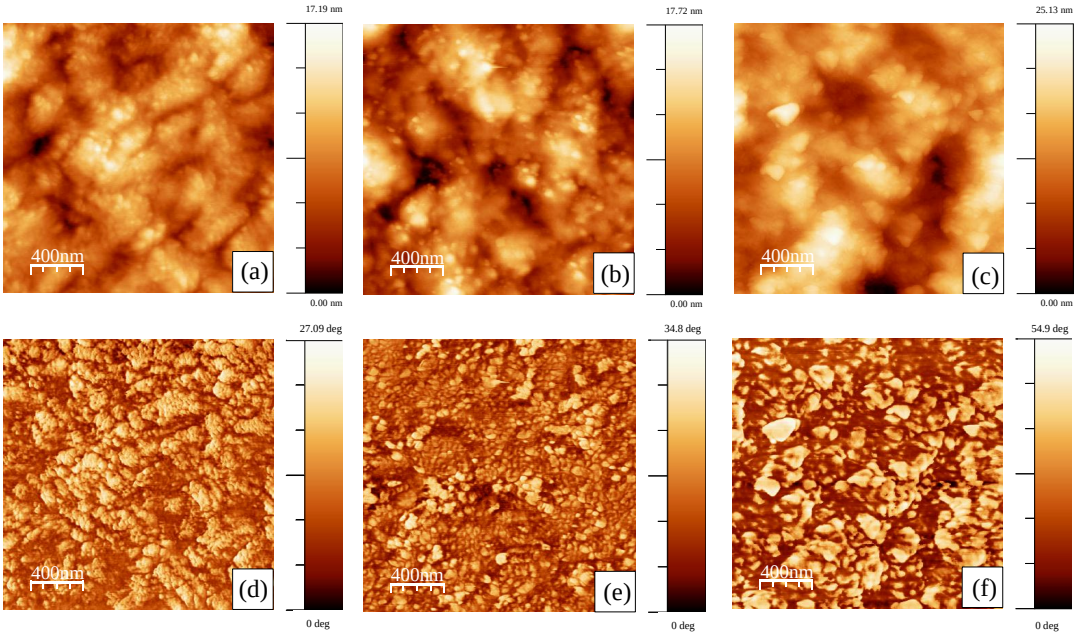

Figure 8.9: AFM images of PDQT/$PC_{61}BM$ in a 1/3 ratio prepared with various concentrations of additive: (a-c) topography images, (d-f) phase images: (a) and (d) no additive (b) and (e) 5 vol%, (c) and (f) 11 vol%.

8.1.4 Discussions and conclusion

The introduction of ODT and DIO successfully increases the PCE of PDQT/$PC_{61}BM$ - based OSCs. In this system, the selection rules identified previously for P3HT/$PC_{61}BM$ OSCs apply. The additive is a poor solvent for the D and a better solvent for the A. However, the role of the additive in the BHJ morphology depends on the type of D used. In the case of P3HT/$PC_{61}BM$, processing additives decrease the average crystallite domain size whereas they increase it in the case of PDQT/$PC_{61}BM$. The origins of the morphological differences between PDQT and P3HT are discussed here.

The AFM images and the XRD measurements show that the molecular arrangement of PDQT chains are significantly different from that of P3HT. When blended with $PC_{61}BM$, PDQT forms large domains while untreated P3HT is known for intermixing with $PC_{61}BM$ [86]. Clearly, PDQT has a stronger tendency to crystallize than P3HT. The morphological differences can naturally be attributed to the different interactions caused by the difference in polymer backbone. However, the morphology is not dependent solely on the polymer backbone, more general parameters also need consideration. Regarding the molecular weight, several studies in the literature revealed that this parameter significantly affects the aggregation of polymer chains and

thus the photovoltaic performance [75, 79, 99]. For example, Kline et al. showed that low molecular weight P3HT chains are more ordered than high molecular ones which substantially affects the hole mobility [99]. He et al. showed that the photovoltaic performance and the film morphology of a series of PTB7-based polymers significantly vary with the molecular weight. In their study, high molecular weight (above 150 kg/-mol) appears to be necessary for attaining high efficiency [75]. It is noteworthy to point out that the molecular weight of the PDQT used here is much lower than that of P3HT: 21,200 Da for PDQT and 53,000 Da for P3HT. Such large difference in molecular weight can be expected to contribute in explaining the difference in morphological behaviour.

Next, the chemical structure of the polymer side chains also needs consideration. Generally, long side chains are desirable for increasing the solubility of polymers but besides their effects on the solubility, the side chains were also shown to affect the domain sizes of polymer in films. A study from Li et al. on DPP-based polymers showed that increasing side chains length increases the diameter of the D fibrils which was detrimental for the performance. The efficiency of OSCs was best for polymer with small side chain lengths [120]. PDQT possesses large substituents (Figure 8.2) wich are consequently also expected to contribute in its aggregation behavior.

Further investigation is required to identify and to understand the influence of the polymer backbone and the more general polymer properties such as the molecular weight and the side chain length on the morphology. The effects of additives on the morphology of diverse D/A system needs to consider the above parameters.

8.2 Studies on PCDTBT

8.2.1 Introduction to carbazole based copolymers

Poly(2,7-carbazole) derivatives represent an efficient family of copolymers for BHJ-OSCs [18, 19]. The carbazole is an electron rich moiety that consists of two six-membered benzene rings fused on either side of a five-membered nitrogen-containing ring (See Figure 8.10a).

Among all the derivatives, PCDTBT represents a good candidate as a D material in OSCs [19, 46, 166, 201, 215]. Its chemical structure is presented in Figure 8.10b.

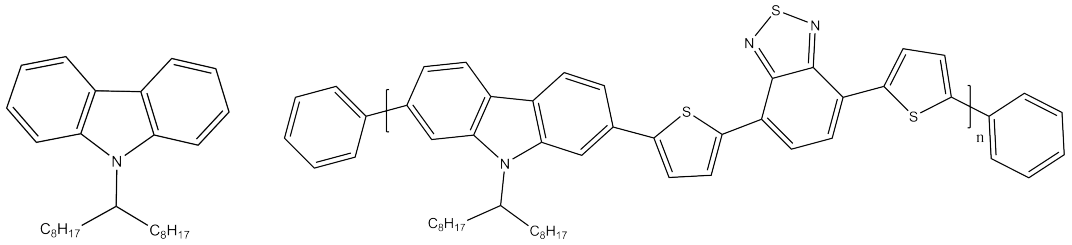

(a) (b)

Figure 8.10: Chemical structures of: (a) a carbazole unit and (B) PCDTBT.

One of the interesting features of PCDTBT is the low lying HOMO level (5.5 eV) which is suitable to obtain OSCs with high V_{oc} [166, 213]. Using Scharber's equation for the estimation of V_{oc} (Equation 1.5) [185], a V_{oc} of 0.9 V is expected. The energy diagram of PCDTBT/$PC_{61}BM$-based OSC is depicted in Figure 8.11.

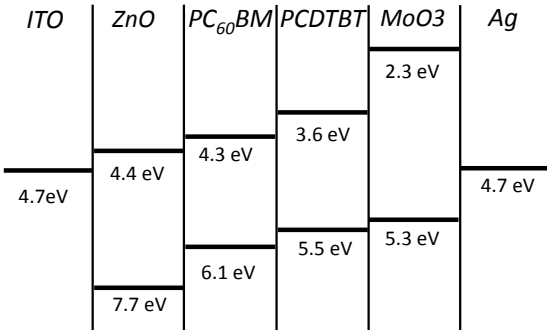

Figure 8.11: Energy levels of PCDTBT/$PC_{61}BM$-OSCs in an inverted architecture.

Unlike P3HT and PDQT, PCDTBT is an amorphous polymer which was reported to highly mix with $PC_{61}BM$ resulting in poor D/A phase separation [36, 221]. Such morphology prevents $PC_{61}BM$ to form A domains with sizes that are efficient for charge transport to the electrode. As a result, the efficiency of OSCs is limited by the charge transport. In order to overcome these issues, the active layer generally needs to fulfill two requirements. First, PCDTBT/$PC_{61}BM$ active layers are required to be prepared with a high proportion of A in order to exhibit larger A domains. In the literature, efficiencies of 6% to 7% were obtained from formulations containing a D/A ratio between 1/2 and 1/4 [129, 146, 201]. The other requirement for high efficiency PCDTBT based OSCs is a thin active layer, generally $\sim$ 70 - 100 nm [16]. Thicker films exhibit inefficient charge collection and therefore low FF and J_{sc} [146]. However, the D semiconductor is the main absorbing material. Therefore, such active layers (thin and with a high proportion of A) optimize charge collection at the expense of light absorption.

Optimization of the morphology can help improving charge collection without sacrificing light absorption. To this end, an investigation on formulation strategies is carried out.

8.2.2 Solubility properties of PCDTBT

The HSPs of PCDTBT are determined experimentally by performing solubility tests. The HSP values resulting from the fitting are presented in Table 8.5 and the graphical representation of the PCDTBT solubility sphere is depicted in Figure 8.12.

Table 8.5: HSPs of PCDTBT.

	δD [MPa$^{1/2}$]	δP [MPa$^{1/2}$]	δH [MPa$^{1/2}$]	R_O [MPa$^{1/2}$]	FIT	RED (with $PC_{61}BM$)
PCDTBT	19.10	3.50	5.19	5.90	0.98	0.30

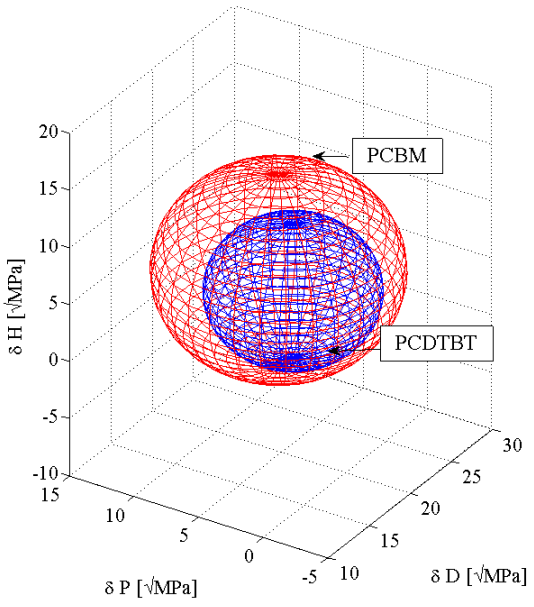

Figure 8.12: Solubility spheres of PCDTBT (in blue) and $PC_{61}BM$ (in red) in the Hansen solubility space.

In Figure 8.12, the solubility sphere of PCDTBT visually appears to be relatively close to the one of $PC_{61}BM$ suggesting a certain affinity between them. The RED between PCDTBT and $PC_{61}BM$ can be calculated in order to estimate their affinity.

Graham et al. used this method to predict the extent of phase separation between small molecules [63]. Here, the RED between PCDTBT and $PC_{61}BM$ is calculated to be 0.30 $MPa^{1/2}$. For comparison, $PC_{61}BM$ has a RED of 0.50 $MPa^{1/2}$ with P3HT and a RED of 0.55 $MPa^{1/2}$ with PDQT. These results suggest that $PC_{61}BM$ has a higher affinity with PCDTBT than with P3HT or PDQT, which is in line with the highly mixed interpenetrated network formed between PCDTBT and $PC_{61}BM$.

8.2.3 Performance of OSCs based on PCDTBT/$PC_{61}BM$.

Preliminary optimizations on PCDTBT/$PC_{61}BM$ - based OSCs are carried out to define the optimum D/A ratios and film thicknesses. Table 8.6 lists the D/A ratios, the solid contents and the resulting thicknesses investigated.

Table 8.6: Properties of PCDTBT/$PC_{61}BM$ active layers investigated.

D/A ratio	**Solid content**	**Spin-casting speed**	**Thickness**
1/1	15 $mg.mL^{-1}$	1500 rpm	159 nm
1/2	25 $mg.mL^{-1}$	1000 rpm	322 nm
		1500 rpm	232 nm
		2000 rpm	170 nm
	20 $mg.mL^{-1}$	1600rpm	108 nm
1/3	25 $mg.mL^{-1}$	800 rpm	266 nm
		1000 rpm	230 nm
		1500 rpm	177 nm
		2000 rpm	137 nm
	20 $mg.mL^{-1}$	700 rpm	113 nm
		1300 rpm	91 nm
		1900 rpm	69 nm
1/4	20 $mg.mL^{-1}$	700 rpm	83 nm
		1300 rpm	51 nm
		1900 rpm	44 nm

Figure 8.13 shows the electrical performance (V_{oc}, FF, J_{sc} and PCE) of OSCs prepared with the parameters listed in Table 8.6. Overall, the results suggest that the electrical parameters are primarily dependent on the thickness. PCEs over 3% can be obtained for active layer thicknesses between 90 nm and 130 nm. The highest PCE of 4.44% is obtained for OSCs with a D/A ratio of 1/2 in an active layer of 108 nm.

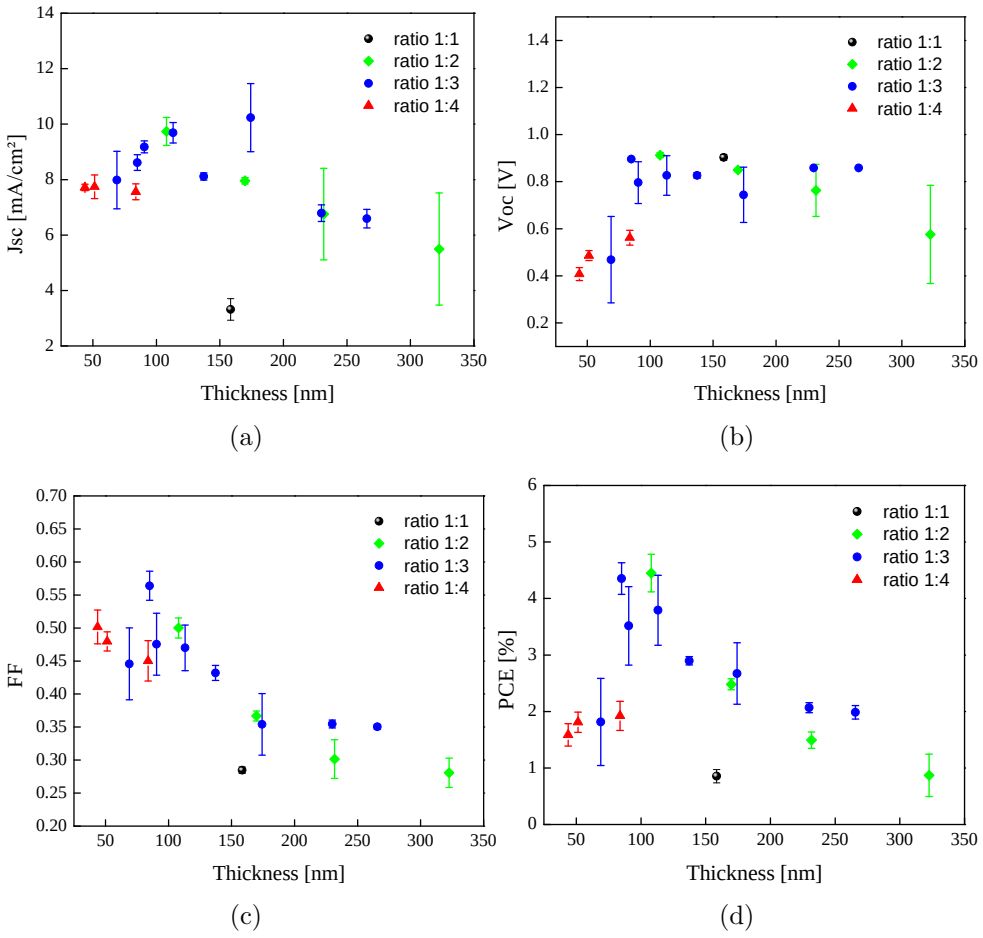

Figure 8.13: Photovoltaic parameters of OSCs as a function of the thickness for various D/A ratios: (a) J_{sc}, (b) V_{oc}, (c) FF and (d) PCE.

DIO and ODT are investigated as processing additives for the PCDTBT/$PC_{61}BM$ system. In contrast to PDQT and P3HT, the HSPs show that DIO and ODT are located inside the solubility spheres of PCDTBT and $PC_{61}BM$ as depicted in Figure 8.14.

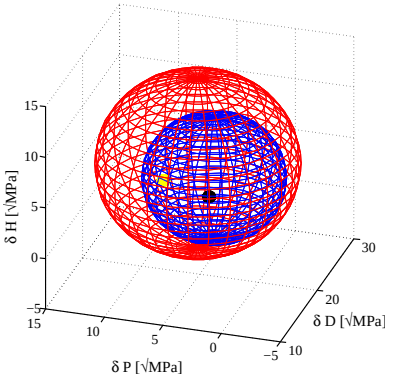

Figure 8.14: Hansen solubility spheres of PCDTBT and $PC_{61}BM$ and the following solvents: DIO (black), ODT (yellow).

In Figure 8.15, the UV-visible absorption spectra of films prepared with and without DIO show that the introduction of DIO leads to a red-shift of PCDTBT absorption peak. The wavelength of PCDTBT absorption maximum is 568 nm in films without DIO and increases to 582 nm in films prepared with 5 vol% of DIO. Similarly, ODT causes a red-shift of the absorption peak (Table 8.7).

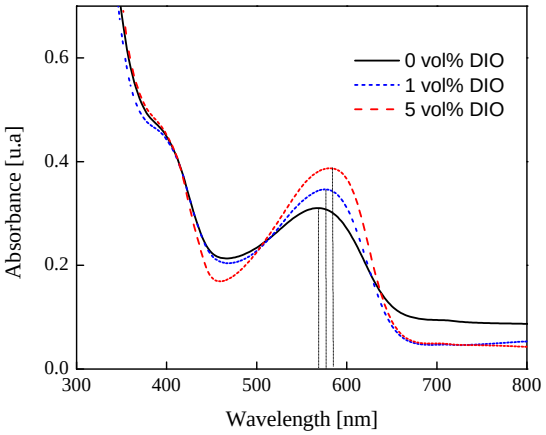

Figure 8.15: Solid-state UV-Vis absorption spectra of PCDTBT/$PC_{61}BM$ films (ratio 1/3) prepared without or with DIO.

Table 8.7: Absorption maximum of PCDTBT/$PC_{61}BM$ films with or without processing additive.

	Control	DIO		ODT	
	0	1 vol%	5 vol%	1 vol%	5 vol%
Absorption maximum [nm]	568	576	582	572	578

This red-shift is similar to the effects of DIO or ODT on other D polymers and is attributed to an increased degree of π-conjugation [5, 66, 89]. The UV-Vis absorption spectra therefore suggest that DIO and ODT are effective in increasing the degree of ordering within PCDTBT chains.

The effects of DIO and ODT on the photovoltaic performance of OSCs are investigated by preparing OSCs from solutions containing DIO or ODT in various concentrations (from 0.5 vol% to 2 vol%). The results show that the introduction of these solvents decreases the performance of OSCs. This suggests that increased order within the polymer chains does not improve the photovoltaic performance of PCDTBT/$PC_{61}BM$ - based OSCs.

Next to formulations with DIO and ODT, several other solvent formulations are tested. OSCs are fabricated using the widely used 1-chloronaphthalene as a processing additive,

xylene as a good solvent for both semiconductors, NMP as a good solvent for $PC_{61}BM$ and poor solvent for PCDTBT. None of these formulations were successful in improving the photovoltaic performance of PCDTBT/$PC_{61}BM$ - OSCs. It is now noteworthy to point out that all these approaches are generally used to enhance the aggregation or the crystallinity of D polymers. The fact that all of these approaches are unsuccessful suggests that increasing the ordering of PCDTBT chains is inefficient in increasing the PCE of PCDTBT/$PC_{61}BM$ - OSCs. Next, studies on the aggregation of $PC_{61}BM$ are carried out.

8.2.4 PCDTBT/$PC_{61}BM$/C_{60} ternary blend.

This next study focuses on the effect of C_{60} as a nucleating agent for $PC_{61}BM$ in the PCDTBT/$PC_{61}BM$ system. Because of the low solubility of C_{60} in ODCB [90, 189], C_{60} is expected to undergo the transition from the liquid state to the solid state at an earlier stage than $PC_{61}BM$ during the process of film formation. The introduction of C_{60} is therefore expected to alter the aggregation of $PC_{61}BM$. Systems based on a ternary blend of $PC_{61}BM$ and C_{60} as the acceptor components, and PCDTBT as the donor are studied. The resulting active layers are of the type: PCDTBT/$PC_{61}BM_{(1-x)}$/$C_{60(x)}$ with x the fraction of C_{60} varying from 0 to 1.

The UV-Vis spectra of ternary blends with C_{60} fractions of 0, 0.4 and 0.7 are depicted in Figure 8.16. The UV-Vis spectra show that the introduction of C_{60} causes a blue-shift in the absorption peak of PCDTBT. The wavelength of PCDTBT absorption maximum is 564 nm in films without C_{60} and decreases to 558 nm in PCDTBT/$PC_{61}BM_{(0.3)}$/$C_{60(0.7)}$ films. In contrast to the red-shift caused by increased ordering within polymer chains, the blue-shift can be interpreted as a reduction of polymer chain ordering.

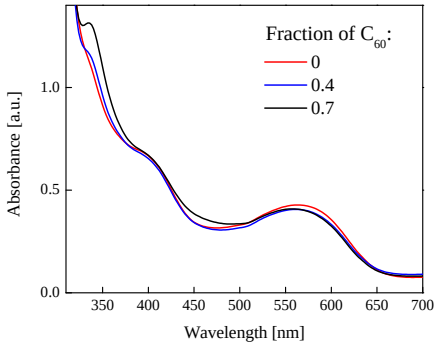

Figure 8.16: Solid state UV-Vis spectra of PCDTBT/$PC_{61}BM_{(1-x)}$/$C_{60(x)}$ films with various fraction of C_{60}.

Next, the electron mobility in a ternary blend is measured and compared to the electron mobilities of PCDTBT/$PC_{61}BM$ in various D/A ratios. The electron mobilities are measured in OTFT configurations for PCDTBT/$PC_{61}BM$ systems with D/A ratios of 1/4, 1/3 and 1/2 and for the ternary blend PCDTBT/$PC_{61}BM_{(0.6)}/C_{60(0.4)}$ at a D/A ratio of 1/2. Figure 8.17a depicts the transfer characteristics of the resulting n-type OTFTs. The OTFT mobilities are calculated at different values of gate voltage and Figure 8.17b depicts the mobility as a function of V_{GS}-V_{th}. Table 8.8 displays the average electron mobility measured from 2 to 4 OTFTs at V_{GS}-V_{th} = 4 V.

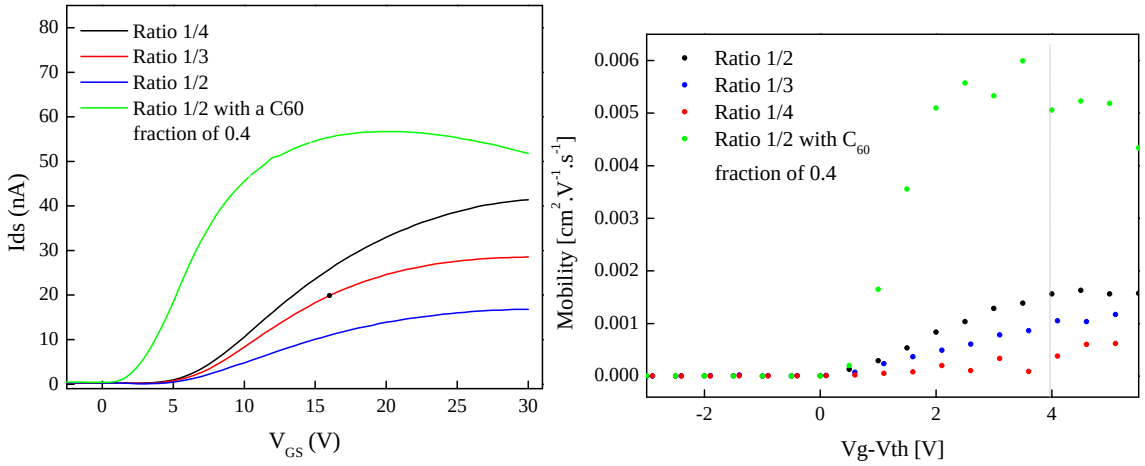

(a) (b)

Figure 8.17: (a) Transfer characteristics and (b) Mobility as a function of V_{GS}-V_{th} for various D/A ratios and for PCDTBT/$PC_{61}BM_{(0.6)}/C_{60(0.4)}$.

Table 8.8: Average electron mobility measured in a saturation regime at V_{GS}-V_{th} = 4 V.

Formulations	Electron mobility x10^{-3} [$cm^2.V^{-1}.s^{-1}$]
Ratio 1/4	1.56 ± 0.29
Ratio 1/3	1.13 ±0.09
Ratio 1/2	0.48 ±0.08
Ratio 1/2 in the ternary blend	4.96 ±0.45

Regarding the effects of processing additives on the electron mobility, the results show that increasing proportion of A in the D/A blend increases the mobility. This result is expected since a high proportion of A leads to an increased amount of A pathways. For a D/A ratio of 1/2, the electron mobility increases significantly with the introduction

of C_{60}: the ternary blend exhibits an electron mobility six times higher than that of a blend without C_{60} (Table 8.8). Such an increase in electron mobility shows that the introduction of C_{60} has an effect on the aggregation of $PC_{61}BM$. Interestingly, the mobility of the ternary blend in a 1/2 ratio is also much higher than that of PCDTBT/$PC_{61}BM$ in a 1/4 ratio (which contains more $PC_{61}BM$). This suggests that the introduction of C_{60} results in a particular electron mobility that cannot be obtained in binary blend, even when fabricated with a high proportion of A.

Series of OSCs are prepared from ternary blends: PCDTBT/$PC_{61}BM_{(1-x)}$/$C_{60(x)}$, with a D/A ratio kept constant and x the fraction of C_{60} varied from 0 to 1. The energy levels of such ternary-blend OSCs are displayed in Figure 8.18. Two D/A ratios are studied: 1/3 and 1/2.

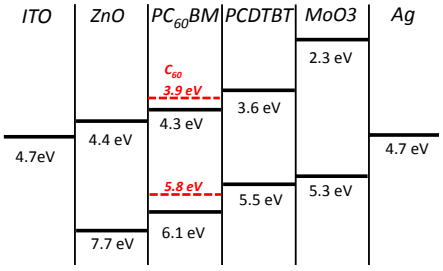

Figure 8.18: Energy levels of PCDTBT/$PC_{61}BM$/C_{60}- OSCs in an inverted architecture.

Figure 8.19 shows the photovoltaic parameters (V_{oc}, J_{sc}, FF and PCE) of ternary OSCs as a function of the fraction of C_{60}.

The J_{sc} and the FF are not severely impacted by the introduction of C_{60}, with the exception of the OSC prepared from only C_{60} at a 1/2 ratio. The PCE remains relatively unchanged for a C_{60} fraction ≤ 0.7 and drops significantly when C_{60} is the only A component. The poor photovoltaic performance obtained in the case of PCDTBT/C_{60}-OSCs can be due to the low solubility of C_{60} in ODCB (23 to 27 mg.mL^{-1} [90, 189]) which is likely to cause coarse aggregates. The V_{oc} is highest in OSCs with only $PC_{61}BM$ as the A component (0.90 V for the 1/2 ratio and 0.91 V for the 1/3 ratio) and decreases with increasing fraction of C_{60}. At a fraction x of 1, the V_{oc} values drop to 0.62 V and 0.79 V for OSCs with D/A ratios of 1/2 and 1/3 respectively. The variation in V_{oc} with the composition of the ternary blends has been the subject of investigation in the literature and remains under debate. Street et al. argued that a ternary blend can be described with an alloy model of D and A with a V_{oc} depending

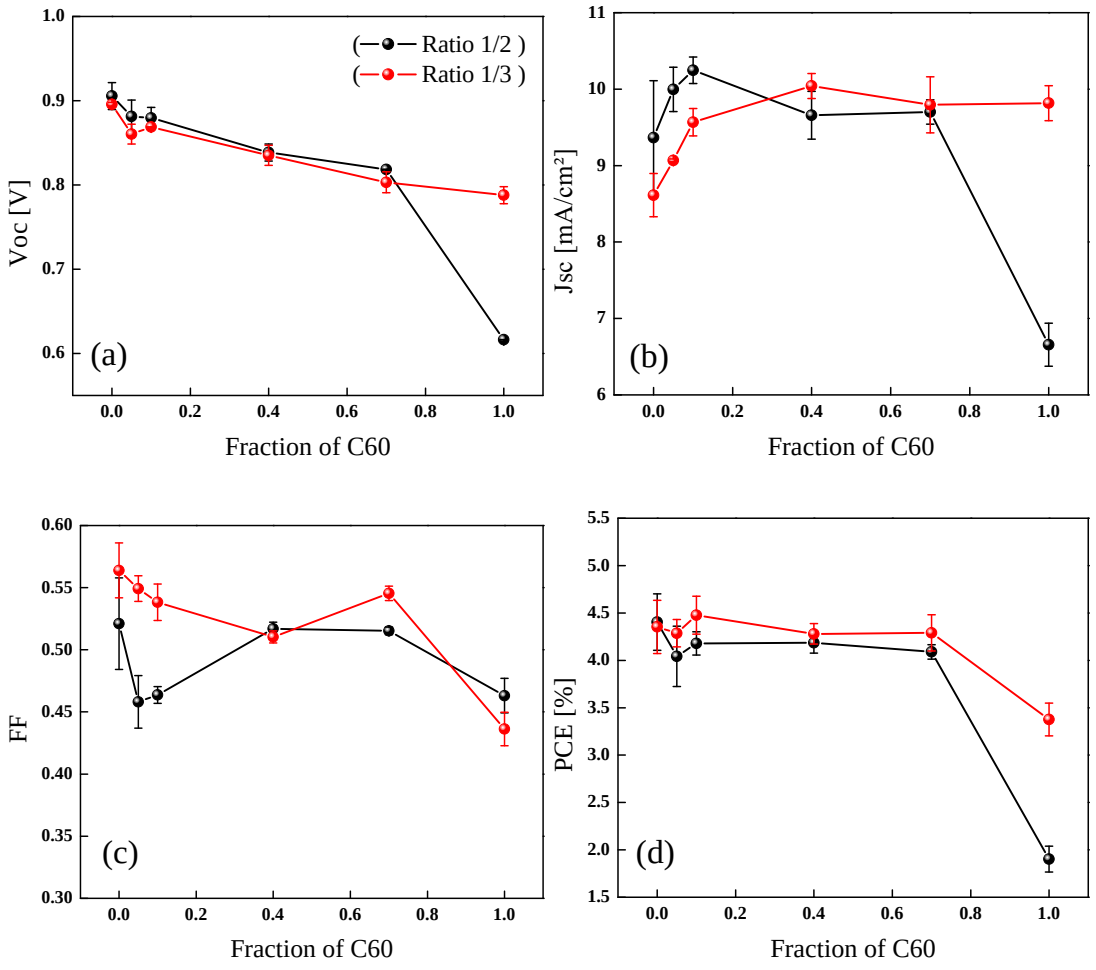

Figure 8.19: Electrical parameters of OSCs with various fraction of C_{60}: (a) V_{oc}, (b) J_{sc}, (c) FF and (d) PCE.

on the average HOMO LUMO energy levels [198]. Such model fails to describe the present ternary blend because it predicts an increase in V_{oc} with the introduction of C_{60} due to its higher lying LUMO level. As previously introduced in Section 1.4.4 (General factors influencing BHJ-OSC efficiency), presence of fullerene nanocrystals can shift the energy of the charge transfer state. Such shift is reported to decrease the V_{oc} of OSCs [175]. Therefore, the decrease in V_{oc} observed in this experiment suggest that the introduction of C_{60} increases the amount of fullerene nanocrystals ($PC_{61}BM$ or C_{60} or a mixture of both). The increase in fullerene aggregation caused by the introduction of C_{60} is consistent with the trend in electron mobility observed from the OTFT mobility measurements, along with the disruption of polymer chain ordering suggested by the blue-shift in the UV-Vis absorption spectra. Such morphological changes caused by C_{60} do not affect the PCE.

The effects of C_{60} introduction on OSC-stability is then studied. As presented in the literature section on OSC stability in chapter 7-section 7.1, $PC_{61}BM$ is subject to severe thermal degradation. Upon prolonged thermal annealing, $PC_{61}BM$ molecules can form micrometer size aggregates which are profoundly detrimental for the performance of OSCs. In PCDTBT/$PC_{61}BM$ films, Derue et al. showed that thermal annealing above 160 °C causes the formation of micrometer sizes $PC_{61}BM$ [56]. In the literature, several studies were carried out to improve the thermal stability of $PC_{61}BM$ [222]. Among these, few studies reported on the beneficial effect of the introduction of C_{60} on the thermal stability of D/A blends based on P3HT/$PC_{61}BM$ [178], or poly[2,3-bis-(3-octyloxyphenyl)quinoxaline-5,8-diyl-alt thiophene-2,5diyl](TQ1)/$PC_{61}BM$ [126].

For the study on OSC thermal stability, three types of ternary blend OSCs are fabricated with a D/A ratio kept constant at 1/2 and with a C_{60} fraction, x, of 0, 0.4 and 0.7. The ZnO layer and the active layer are deposited following the procedure used for the fabrication of inverted OSCs. After the deposition of the active layer, the samples are thermally annealed on a hot plate set at 160 °C for two or four hours. The top electrodes (MoO_3/Ag) are evaporated on top of the thermally annealed samples. The J-V characteristics of these OSCs are measured and the photovoltaic performances are normalized with respect to the parameters of fresh OSCs. Figure 8.20 shows the evolution of normalized PCE as a function of the annealing time. The normalized photovoltaic performances of the OSCs after two hours of thermal treatment are listed in Table 8.9.

Table 8.9: Normalized photovoltaic parameters of ternary blend OSCs after two hours of thermal treatment at 160 °C.

C_{60} fraction	**Normalized parameters [%]**			
	J_{sc}	V_{oc}	**FF**	**PCE**
0	76.9	89.3	74.5	51.2
0.4	101.1	92.3	88.9	83.0
0.7	112.9	94.7	88.1	94.2

After two hours of thermal treatment, the PCE of the binary blend PCDTBT/$PC_{61}BM$ drops to 51.2% of the initial value. Ternary blend OSCs demonstrate a superior thermal stability with PCEs maintained at 83.0% and 94.2% of the initial PCEs for C_{60} fractions of 0.4 and 0.7 respectively. The thermal treatment decreases primarily the FF and J_{sc} of binary OSCs likely caused by the aggregation of $PC_{61}BM$. The ternary blends exhibit a

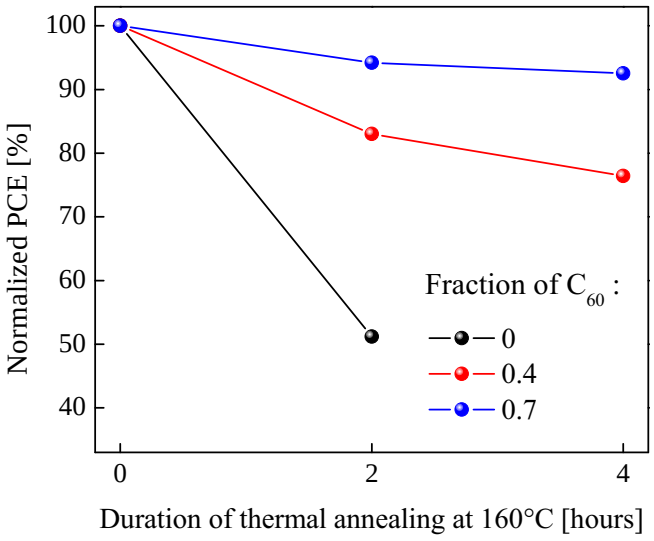

Figure 8.20: Normalized PCE as a function of the time of annealing treatment at 160°C.

different trend characterized by less decrease in FF and an increase in J_{sc}. This increase in J_{sc} is unlikely caused by morphological changes but can be attributed to other phenomenon such as the removal of residual solvent in the active layer upon thermal annealing. Overall, ternary blends demonstrate high thermal stability compared to the binary blend. This suggests that thermal annealing does not deteriorate the active layer morphology as severely as in the binary system. Interestingly, the thermal stability is dependent on the fraction of C_{60}: superior thermal stability is obtained for the ternary blend with a C_{60} fraction of 0.7 compared to 0.4.

Microscopic images of PCDTBT/PC_{61}BM and ternary blend films are analyzed before and after thermal treatment of 2, 4 and 8 hours at 160 °C. The images are depicted in Figure 8.21. Figure 8.22 displays images with higher magnifications of blends with C_{60} fraction of 0 and 0.4. As shown in Figure 8.21, thermally treated PCDTBT/PC_{61}BMfilms demonstrate PC_{61}BM crystallites throughout the active layer. On the other hand, films prepared from ternary blends exhibit a surface without the presence of aggregates even after 8 hours of thermal treatment. The introduction of C_{60} in PCDTBT/PC_{61}BM blend is here shown to decrease significantly the aggregation of PC_{61}BM by thermal treatment. This explains the enhanced thermal stability of OSCs.

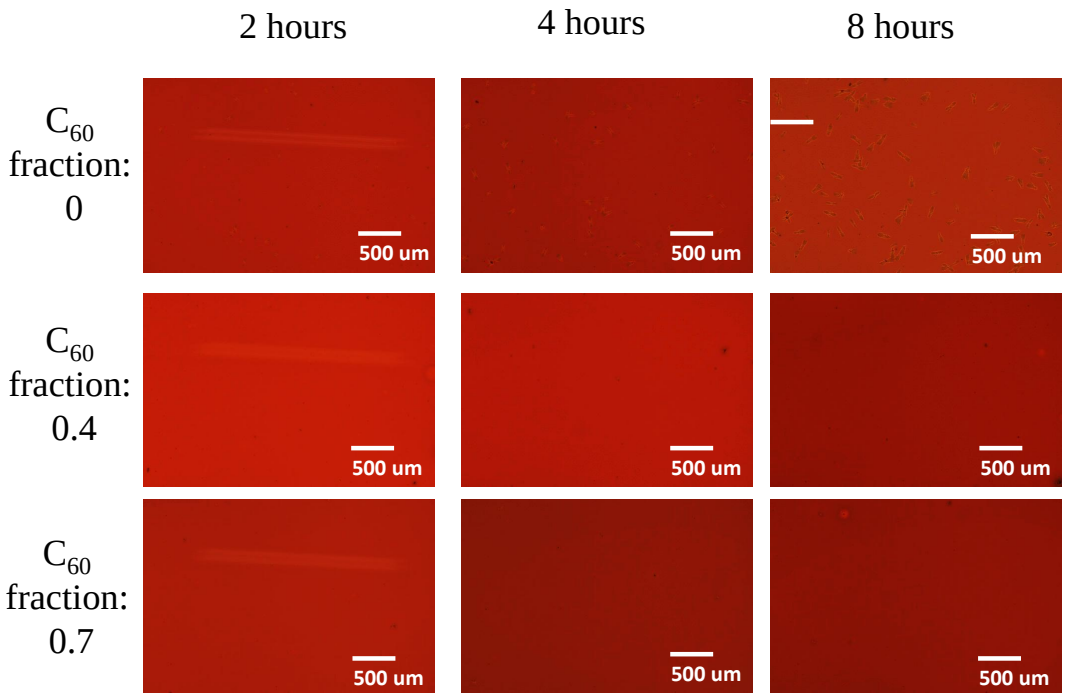

Figure 8.21: Microscopic images of PCDTBT/$PC_{61}BM_{(1-x)}$/$C_{60(x)}$ films thermally treated at 160 °C for 2 hours, 4 hours and 8 hours (magnification 20).

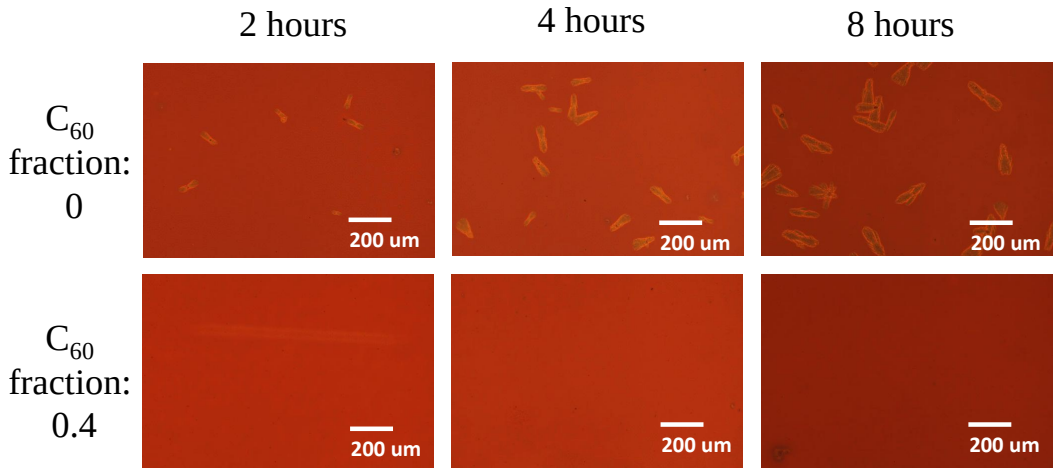

Figure 8.22: Microscopic images of PCDTBT/$PC_{61}BM_{(1-x)}$/$C_{60(x)}$ films thermally treated at 160 °C for 2 hours, 4 hours and 8 hours (magnification 50).

8.2.5 Conclusions

Polymer chain ordering was controlled using processing additives such as DIO and ODT. However, the introduction of these processing additives is inefficient in increasing the performance of PCDTBT/$PC_{61}BM$ - OSCs and even decreases it. The use of a ternary blend based on PCDTBT/$PC_{61}BM_{(1-x)}/C_{60(x)}$ appears to alter the aggregation of $PC_{61}BM$ and to cause a disruption of PCDTBT polymer chains. Measurements of photovoltaic parameters of ternary blend-OSCs show that the PCE is relatively independent on the C_{60} fraction as long as the fraction is ≤ 0.7. This result is relevant for the prospect of low cost OSCs because $PC_{61}BM$ is a relatively expensive material ($\sim$ 10 times more expensive than C_{60} [2]). Around 10 to 30% of the total fabrication costs of organic solar modules is attributed to the organic semiconductors [13, 150], therefore the replacement of a fraction of $PC_{61}BM$ by C_{60} would reduce module costs. Also, the introduction of C_{60} was shown to prevent the aggregation of $PC_{61}BM$ upon thermal annealing. As a result, the OSCs fabricated from ternary blends demonstrate significant thermal stability compared to the binary blend.

Chapter 9

Conclusions and future work

9.1 Conclusions

This thesis provides a comprehensive study on the introduction of processing additives used to increase the performance of solution-processed BHJ-OSCs.

First, a systematic method for the selection of processing additives was developed. This method uses the Hansen theory to describe the solubility properties of the organic semiconductors under study and to determine numerical figures of merit that can be used for selecting suitable processing additives. This method was successfully applied to the P3HT/PC_{61}BM-system. Three novel processing additives, that result in up to a two-fold increase in the PCE, were identified.

The mechanistic role of processing additives in improving the BHJ morphology was elucidated by correlating structural and optical characterizations. Studies of the trends in V_{oc} and UV-visible absorption spectra showed that processing additives increased the overall crystallinity in P3HT in the BHJ whereas XRD patterns revealed that the increased crystallinity is associated with a decrease in the polymer crystallite sizes. These results suggest that processing additives lead to the formation of a BHJ with more numerous but smaller polymer crystallites.

The photovoltaic performances of additive treated-OSCs were shown to significantly depend on the device architecture. These differences were attributed to variations in hole and electron mobilities induced by the introduction of additives. As the excitons are predominantly generated near the bottom of the active layer, holes and electrons are required to travel different distances before their collection by the respective electrodes. As a result, the photovoltaic performance of OSCs is dependent on the ratio between electron and hole mobilities. Since the mobilities are influenced by the processing additives, the device architecture must be considered when additives are used.

As OSC stability is equally important as the PCE, the effects of processing additives on OSC stability were studied by means of photo-stability measurements. Compared to the commonly used thermal annealing technique, the results show that the use of additives improves the photo-stability of OSCs. The best results are obtained with ODT-treated OSCs. Several photo-stability studies, which include adhesion measurements, show that light irradiation causes interfacial degradation. Interestingly, adhesion measurements show that ODT-treated OSCs suffer less from interfacial photo-degradation than thermally annealed OSCs, which could explain the improved life time.

Besides P3HT, two other polymers were studied: the semi-crystalline PDQT and the amorphous PCDTBT. In the case of PDQT, ODT and DIO are successful in increasing the PCE of OSCs, indicating that the additive selection rules identified for P3HT/PC_{61}BM also apply to this case. On the other hand, the additive approach appeared to be unsuccessful for PCDTBT-based OSCs, most likely due to the amorphous character of PCDTBT, which does not require control of the crystallinity as is required for than semi-crystalline polymers. These results suggest that the selection rules designed for P3HT/PC_{61}BM systems apply for semi-crystalline polymers but not for amorphous polymers.

9.2 Future work

Chapter 8 showed that the use of conventional processing additives failed to improve the performance of PCDTBT-based OSCs. Although additives increased the PCE of PDQT-based OSCs, they appeared to have a different effect on the BHJ morphology than they have on P3HT-based OSCs. Overall, the effectiveness of additives is found to strongly depend on the type of polymer. Therefore, the additive selection method developed in this thesis based on the P3HT/PC_{61}BM system needs to be extended to a more general perspective. Not only the solubility properties, but several other aspects of the D polymers need to be considered, namely the tendency to crystallize, the molecular weight, the nature of the side chains and the miscibility with A materials. A next step would be to identify how processing additives affect the morphology of BHJ-OSCs as a function of the properties of the D polymers. This is an essential step towards a more general applicability of processing additives and a streamlined way to formulate D/A blends for high efficiency OSCs.

The photo-stability tests suggest that additives can be employed to perform a double function: to increase the efficiency and to increase the photo-stability of OSCs. To fully exploit this double function, the specific case of ODT-treated OSCs needs to be understood due to their particularly high photo-stability. Two possible hypotheses about the role of additive in this regard arise: either the increase in interfacial adhesion is due to morphological changes in the active layer or it is due to the presence of additive. Although the PM-IRRAS spectra gave no trace of ODT in the BHJ, remaining traces of ODT may be present in quantities that are below the detection limit of this technique. ODT contains two thiol groups which are known for acting as scavengers for free radicals [202], which can be generated during photo-degradation. Therefore,

the presence of these scavenger groups may prevent free radical reactions that cause degradation. One idea to test the radical scavenging function of ODT would be to introduce another thiol containing molecule in the active layer instead of ODT and to test the OSC photo-stability.

Another stability-related subject raised by this thesis concerns the introduction of C_{60} in the active layer. The ternary blend based on PCDTBT/$PC_{61}BM_{(x)}$/$C_{60(1-x)}$ was shown to exhibit a higher thermal stability compared with the binary system based on PCDTBT/PC_{61}BM. Replacing a fraction of PC_{61}BM by C_{60} is attractive as a method to increase thermal stability in addition to economic benefits. To fully exploit the beneficial properties of C_{60} as an acceptor, a binary system based on PCDTBT/C_{60} would be of great interest. However, when a pure PCDTBT/C_{60} system was made, it exhibited a low PCE, likely due to morphological issues in the BHJ. Processing additives that can help to improve the morphology of the acceptor in the BHJ should be therefore investigated. To date, processing additives are generally investigated for their effects on the donor polymer. Further work should consider the effects on the acceptor in order to optimize systems such as PCDTBT/C_{60}.

Appendix A

Scientific communications

Scientific publications

U. Vongsaysy, B. Pavageau, G. Wantz, D.M. Bassani, L. Servant, H. Aziz *Guiding the selection of processing additives for increasing the efficiency of bulk heterojunction polymeric solar cells.* Advanced Energy Materials, 4 (3) 2014 (2013).

U. Vongsaysy, D.M. Bassani, L. Servant, B. Pavageau, G. Wantz, H. Aziz *Formulation strategies for optimizing the morphology of polymeric bulk heterojunction organic solar cells: a brief review.* Journal of Photonics for Energy, 4 (1) (2014).

Oral presentations

U. Vongsaysy, B. Pavageau, G. Wantz, D.M. Bassani, L. Servant, H. Aziz. *Processing Additives for Polymeric Bulk Heterojunction Organic Solar Cells.* **Young Scientists Symposium Nanorgasol**, Mèze, France, 2013.

U. Vongsaysy, B. Pavageau, G. Wantz, D.M. Bassani, L. Servant, H. Aziz. *Active layer concepts for increased feasibility.* **IDS-FunMat Training School 2011**, Sesimbra, Portugal, 2011.

Poster presentations

U. Vongsaysy, B. Pavageau, G. Wantz, D.M. Bassani, L. Servant, H. Aziz. *Selection of processing additives for polymeric organic solar cells.* **SPIE Optics + Photonics**, San Diego, United States of America, 2014.

U. Vongsaysy, B. Pavageau, G. Wantz, D.M. Bassani, L. Servant, H. Aziz. *Processing additives for polymeric organic photovoltaics* **IDS-FunMat Training School 2013**, Annecy, France, 2013.

U. Vongsaysy, B. Pavageau, G. Wantz, D.M. Bassani, L. Servant, H. Aziz. *Selection of processing additives for polymeric organic photovoltaics* **Workshop Soochow-University of Waterloo**, Waterloo, Canada, 2013.

U. Vongsaysy, B. Pavageau, G. Wantz, D.M. Bassani, L. Servant, H. Aziz. *Guiding the selection of solvent additives for improving the efficiency of bulk heterojunction polymer solar cells* **11^{th} International Symposium on Functional π-electron systems**, Arcachon, France, 2013.

U. Vongsaysy, B. Pavageau, G. Wantz, D.M. Bassani, L. Servant, H. Aziz.{Guiding the selection of solvent additives for improving the efficiency of bulk heterojunction polymer solar cells **The 7ht annual Solvay-Cope symposium on organic electronics**, Bordeaux, France, 2013.

U. Vongsaysy, B. Pavageau, G. Wantz, D.M. Bassani, L. Servant, H. Aziz. *Organic Photovoltaics: New concepts for increased feasibility* **IDS-FunMat Training School 2012**, Anglet, France, 2012.

U. Vongsaysy, B. Pavageau, G. Wantz, D.M. Bassani, L. Servant, H. Aziz. *Organic Photovoltaics: New concepts for increased feasibility* **15 ème Journée de l'École doctorale des sciences chimiques**, Bordeaux, France, 2012.

U. Vongsaysy, B. Pavageau, G. Wantz, D.M. Bassani, L. Servant, H. Aziz. *Organic Photovoltaics: New concepts for increased feasibility* **Rhodia internal presentation**, Pessac, France, 2011.

Bibliography

[1] National Centre for Photovoltaics, http://www.nrel.gov/ncpv/ , Date accessed: 1st of July 2014.

[2] Solaris Chem, http://www.solarischem.com/Fullerenes.html, Date accessed: 15th of September 2014.

[3] Abbas, M., and Tekin, N. Balanced charge carrier mobilities in bulk heterojunction organic solar cells. *Applied Physics Letters 101*, 7 (2012), 073302.

[4] Abdou, M. S. a., and Holdcroft, S. Mechanisms of photodegradation of poly(3-alkylthiophenes) in solution. *Macromolecules 26*, 11 (May 1993), 2954–2962.

[5] Agostinelli, T., Ferenczi, T. a. M., Pires, E., Foster, S., Maurano, A., Müller, C., Ballantyne, A., Hampton, M., Lilliu, S., Campoy-Quiles, M., Azimi, H., Morana, M., Bradley, D. D. C., Durrant, J., Macdonald, J. E., Stingelin, N., and Nelson, J. The role of alkane dithiols in controlling polymer crystallization in small band gap polymer:Fullerene solar cells. *Journal of Polymer Science Part B: Polymer Physics 49*, 10 (May 2011), 717–724.

[6] Aïch, B. R., Beaupré, S., Leclerc, M., and Tao, Y. Highly efficient thieno[3,4-c]pyrrole-4,6-dione-based solar cells processed from non-chlorinated solvent. *Organic Electronics 15*, 2 (Dec. 2013), 543–548.

[7] Aïch, B. R., Lu, J., Beaupré, S., Leclerc, M., and Tao, Y. Control of the active layer nanomorphology by using co-additives towards high-performance bulk heterojunction solar cells. *Organic Electronics 13*, 9 (2012), 1736–1741.

[8] Albrecht, S., Schindler, W., Kurpiers, J., Kniepert, J., Blakesley, J. C., Dumsch, I., Allard, S., Fostiropoulos, K., Scherf, U., and Neher, D. On the field dependence of free Charge carrier generation and recombination in blends of PCPDTBT/PC70BM: Influence of Solvent Additives. *The Journal of Physical Chemistry Letters 3* (2012), 640–645.

[9] Alstrup, J., Jø rgensen, M., Medford, A. J., and Krebs, F. C. Ultra fast and parsimonious materials screening for polymer solar cells using differentially pumped slot-die coating. *ACS applied materials & interfaces 2*, 10 (Oct. 2010), 2819–27.

[10] Alvarado, S., Seidler, P., Lidzey, D., and Bradley, D. Direct Determination of the Exciton Binding Energy of Conjugated Polymers Using a Scanning Tunneling Microscope. *Physical Review Letters 81*, 5 (Aug. 1998), 1082–1085.

[11] An, T. K., Kang, I., Yun, H.-J., Cha, H., Hwang, J., Park, S., Kim, J., Kim, Y. J., Chung, D. S., Kwon, S.-K., Kim, Y.-H., and Park, C. E. Solvent Additive to Achieve Highly Ordered Nanostructural Semicrystalline DPP Copolymers: Toward a High Charge Carrier Mobility. *Advanced materials (Deerfield Beach, Fla.) 25*, 48 (Dec. 2013), 7003–9.

[12] Antoniadis, H., Hsieh, B., Abkowitz, M., Jenekhe, S., and Stolka, M. Photovoltaic and photoconductive properties of aluminum/poly(p-phenylene vinylene) interfaces. *Synthetic Metals 62*, 3 (Feb. 1994), 265–271.

[13] Azzopardi, B., Emmott, C. J. M., Urbina, A., Krebs, F. C., Mutale, J., and Nelson, J. Economic assessment of solar electricity production from organic-based photovoltaic modules in a domestic environment. *Energy & Environmental Science 4*, 10 (2011), 3741.

[14] Barakat, S., Lee-Sullivan, P., Vitale, S. a., and Tsui, T. Y. The effects of low temperature and pressure on the fracture behaviors of organosilicate thin films. *Journal of Materials Research 26*, 19 (Aug. 2011), 2524–2532.

[15] Bartelt, J. a., Beiley, Z. M., Hoke, E. T., Mateker, W. R., Douglas, J. D., Collins, B. a., Tumbleston, J. R., Graham, K. R., Amassian, A., Ade, H., Fréchet, J. M. J., Toney, M. F., and McGehee, M. D. The Importance of Fullerene Percolation in the Mixed Regions of

Polymer-Fullerene Bulk Heterojunction Solar Cells. *Advanced Energy Materials 3*, 3 (Mar. 2013), 364–374.

[16] Beaupré, S., and Leclerc, M. PCDTBT: en route for low cost plastic solar cells. *Journal of Materials Chemistry A 1*, 37 (2013), 11097.

[17] Blom, P. W. M., de Jong, M. J. M., and Vleggaar, J. J. M. Electron and hole transport in poly(p-phenylene vinylene) devices. *Applied Physics Letters 68*, 23 (1996), 3308.

[18] Blouin, N., Michaud, A., Gendron, D., Wakim, S., Blair, E., Neagu-Plesu, R., Belletête, M., Durocher, G., Tao, Y., and Leclerc, M. Toward a rational design of poly(2,7-carbazole) derivatives for solar cells. *Journal of the American Chemical Society 130*, 2 (Jan. 2008), 732–42.

[19] Blouin, N., Michaud, a., and Leclerc, M. A Low-Bandgap Poly(2,7-Carbazole) Derivative for Use in High-Performance Solar Cells. *Advanced Materials 19*, 17 (Sept. 2007), 2295–2300.

[20] Böttiger, A. P. L., Jø rgensen, M., Menzel, A., Krebs, F. C., and Andreasen, J. W. High-throughput roll-to-roll X-ray characterization of polymer solar cell active layers. *Journal of Materials Chemistry 22*, 42 (2012), 22501.

[21] Brabec, C., Dyakonov, V., Parisi, J., and Sariciftci, N. *Organic Photovoltaics Concepts and Realization*, springer ed. 2003.

[22] Brabec, C. J., Cravino, a., Meissner, D., Sariciftci, N. S., Fromherz, T., Rispens, M. T., Sanchez, L., and Hummelen, J. C. Origin of the Open Circuit Voltage of Plastic Solar Cells. *Advanced Functional Materials 11*, 5 (Oct. 2001), 374–380.

[23] Brabec, C. J., Gowrisanker, S., Halls, J. J. M., Laird, D., Jia, S., and Williams, S. P. Polymer-fullerene bulk-heterojunction solar cells. *Advanced materials (Deerfield Beach, Fla.) 22*, 34 (Sept. 2010), 3839–56.

[24] Brabec, C. J., Heeney, M., McCulloch, I., and Nelson, J. Influence of blend microstructure on bulk heterojunction organic photovoltaic performance. *Chemical Society reviews 40*, 3 (Mar. 2011), 1185–99.

[25] Buffeteau, T., Desbat, B., and Turlet, J. Polarization Modulation FT-IR Spectroscopy of Surfaces and Ultra-thin Films : Experimental Procedure and Quantitative Analysis. *Applied Spectroscopy 45*, 3 (1991), 380 – 389.

[26] Byun, W.-B., Lee, S. K., Lee, J.-C., Moon, S.-J., and Shin, W. S. Bladed organic photovoltaic cells. *Current Applied Physics 11*, 1 (Jan. 2011), S179–S184.

[27] Campoy-Quiles, M., Ferenczi, T., Agostinelli, T., Etchegoin, P. G., Kim, Y., Anthopoulos, T. D., Stavrinou, P. N., Bradley, D. D. C., and Nelson, J. Morphology evolution via self-organization and lateral and vertical diffusion in polymer:fullerene solar cell blends. *Nature materials 7*, 2 (Feb. 2008), 158–64.

[28] Chamberlain, G., Cooney, P., and Dennison, S. Photovoltaic properties of merocyanine solid-state photocells. *Nature 289*, 1/8 (1981), 45.

[29] Chambon, S., Derue, L., Lahaye, M., Pavageau, B., Hirsch, L., and Wantz, G. MoO3 Thickness, Thermal Annealing and Solvent Annealing Effects on Inverted and Direct Polymer Photovoltaic Solar Cells. *Materials 5*, 12 (Nov. 2012), 2521–2536.

[30] Chambon, S., Rivaton, A., Gardette, J.-L., and Firon, M. Durability of MDMO-PPV and MDMO-PPV: PCBM blends under illumination in the absence of oxygen. *Solar Energy Materials and Solar Cells 92*, 7 (July 2008), 785–792.

[31] Chang, L., Lademann, H. W. a., Bonekamp, J.-B., Meerholz, K., and Moulé, A. J. Effect of Trace Solvent on the Morphology of P3HT:PCBM Bulk Heterojunction Solar Cells. *Advanced Functional Materials* (Mar. 2011), n/a–n/a.

[32] Chang, M., Choi, D., Fu, B., and Reichmanis, E. Solvent Based Hydrogen Bonding : Impact on Poly (3-hexylthiophene) Nanoscale Morphology and Charge. *ACS nano 7*, 6 (2013), 5402–5413.

[33] Chang, Y.-H., Tseng, S.-R., Chen, C.-Y., Meng, H.-F., Chen, E.-C., Horng, S.-F., and Hsu, C.-S. Polymer solar cell by blade coating. *Organic Electronics 10*, 5 (Aug. 2009), 741–746.

[34] Chen, C.-c., Dou, L., Zhu, R., Chung, C.-h., Song, T.-b., Zheng, Y. B., Hawks, S., Li, G., Weiss, P. S., and Yang, Y. Visibly transparent polymer solar cells produced by solution processing. *acs NANO 6*, 8 (2012), 7185.

[35] Chen, D., Nakahara, A., Wei, D., Nordlund, D., and Russell, T. P. P3HT/PCBM bulk heterojunction organic photovoltaics: correlating efficiency and morphology. *Nano letters 11*, 2 (Feb. 2011), 561–7.

[36] Chen, H., Peet, J., Hu, S., Azoulay, J., Bazan, G., and Dadmun, M. The Role of Fullerene Mixing Behavior in the Performance of Organic Photovoltaics: PCBM in Low-Bandgap Polymers. *Advanced Functional Materials 24*, 1 (Jan. 2014), 140–150.

[37] Chen, H.-Y., Yang, H., Yang, G., Sista, S., Zadoyan, R., Li, G., and Yang, Y. Fast-Grown Interpenetrating Network in Poly(3-hexylthiophene): Methanofullerenes Solar Cells Processed with Additive. *The Journal of Physical Chemistry C 113*, 18 (May 2009), 7946–7953.

[38] Chen, M.-C., Liaw, D.-J., Chen, W.-H., Huang, Y.-C., Sharma, J., and Tai, Y. Improving the efficiency of an organic solar cell by a polymer additive to optimize the charge carriers mobility. *Applied Physics Letters 99*, 22 (2011), 223305.

[39] Chen, T.-a., Wu, X., and Rieke, R. D. Regiocontrolled Synthesis of poly(3-alkylthiophenes) mediated by Rieke zinc: their characterization and solid-state properties. *Journal of the American Chemical Society 117* (1995), 233–244.

[40] Chen, W., Xu, T., He, F., Wang, W., Wang, C., Strzalka, J., Liu, Y., Wen, J., Miller, D. J., Chen, J., Hong, O. K., Yu, O. L., and Darling, S. B. Hierarchical Nanomorphologies Promote Exciton Dissociation in polymer/fullerene bulk heterojunction solar cells. *Nano letters 11* (2011), 3707–3713.

[41] Cheng, Y.-J., Yang, S.-H., and Hsu, C.-S. Synthesis of conjugated polymers for organic solar cell applications. *Chemical reviews 109*, 11 (Dec. 2009), 5868–923.

[42] Cheun, H., Fuentes-hernandez, C., Zhou, Y., Potscavage, W. J., Kim, S.-j., Shim, J., Dindar, A., and Kippelen, B. Electrical and Optical

Properties of ZnO Processed by Atomic Layer Deposition in Inverted Polymer Solar Cells †. *Journal of physical chemistry C 114* (2010), 20713–20718.

[43] Chirvase, D., Parisi, J., Hummelen, J. C., and Dyakonov, V. Influence of nanomorphology on the photovoltaic action of polymer–fullerene composites. *Nanotechnology 15*, 9 (Sept. 2004), 1317–1323.

[44] Chu, T.-Y., Alem, S., Tsang, S.-W., Tse, S.-C., Wakim, S., Lu, J., Dennler, G., Waller, D., Gaudiana, R., and Tao, Y. Morphology control in polycarbazole based bulk heterojunction solar cells and its impact on device performance. *Applied Physics Letters 98*, 25 (2011), 253301.

[45] Chu, T.-y., Alem, S., Verly, P. G., Wakim, S., Lu, J., Tao, Y., Beaupré, S., Leclerc, M., Bélanger, F., Désilets, D., Rodman, S., Waller, D., and Gaudiana, R. Highly efficient polycarbazole-based organic photovoltaic devices Highly efficient polycarbazole-based organic photovoltaic devices. *Applied Physics Letters 95* (2009), 063304.

[46] Chu, T.-y., Lu, J., Beaupre, S., Zhang, Y., Pouliot, J. R., Wakim, S., Zhou, J., Leclerc, M., Li, Z., Ding, J., and Tao, Y. Bulk Heterojunction Solar Cells Using Thieno[3,4-c]pyrrole-4,6-dione and Dithieno[3,2-b:20,30-d]silole Copolymer with a Power Conversion Efficiency of 7.3%. *Journal of the American Chemical Society 133* (2011), 4250–4253.

[47] Chu, T.-Y., Tsang, S.-W., Zhou, J., Verly, P. G., Lu, J., Beaupre, S., Leclerc, M., and Tao, Y. High-efficiency inverted solar cells based on a low bandgap polymer with excellent air stability. *Solar Energy Materials and Solar Cells 96* (Oct. 2012), 155–159.

[48] Coakley, K. M., and Mcgehee, M. D. Conjugated Polymer Photovoltaic Cells. *Chemistry of Materials 16*, 23 (2004), 4533–4542.

[49] Cros, S., de Bettignies, R., Berson, S., Bailly, S., Maisse, P., Lemaitre, N., and Guillerez, S. Definition of encapsulation barrier requirements: A method applied to organic solar cells. *Solar Energy Materials and Solar Cells 95* (May 2011), S65–S69.

[50] Dang, M. T., Hirsch, L., and Wantz, G. P3HT:PCBM, Best Seller in Polymer Photovoltaic Research. *Advanced Materials 23*, 31 (Aug. 2011), 3597–3602.

[51] Dang, M. T., Hirsch, L., Wantz, G., and Wuest, J. D. Controlling the Morphology and Performance of Bulk Heterojunctions in Solar Cells . Lessons Learned from the Benchmark System. *Chemical reviews 113*, 5 (2012), 3734–3765.

[52] Dang, M. T., Wantz, G., Bejbouji, H., Urien, M., Dautel, O. J., Vignau, L., and Hirsch, L. Polymeric solar cells based on P3HT:PCBM: Role of the casting solvent. *Solar Energy Materials and Solar Cells 95*, 12 (Dec. 2011), 3408–3418.

[53] Dante, M., Garcia, A., and Nguyen, T.-q. Three-Dimensional Nanoscale Organization of Highly Efficient Low Band-Gap Conjugated Polymer Bulk Heterojunction Solar Cells. *J. Phys. Chem C 113* (2009), 1596–1600.

[54] Darling, S. B., and You, F. The case for organic photovoltaics. *RSC Advances 3*, 39 (2013), 17633.

[55] Deibel, C., Dyakonov, V., and Brabec, C. J. Organic Bulk-Heterojunction Solar Cells. *IEEE Journal of Selected Topics in Quantum Electronics 16*, 6 (Nov. 2010), 1517–1527.

[56] Derue, L. *Thesis: Stabilisation thermique de la couche photo-active d'une cellule solaire organique par réticulation.* University of Bordeaux I, 2013.

[57] Duong, D. T., Walker, B., Lin, J., Kim, C., Love, J., Purushothaman, B., Anthony, J. E., and Nguyen, T.-Q. Molecular solubility and hansen solubility parameters for the analysis of phase separation in bulk heterojunctions. *Journal of Polymer Science Part B: Polymer Physics 50*, 20 (Oct. 2012), 1405–1413.

[58] Eom, S. H., Park, H., Mujawar, S., Yoon, S. C., Kim, S.-S., Na, S.-I., Kang, S.-J., Khim, D., Kim, D.-Y., and Lee, S.-H. High efficiency polymer solar cells via sequential inkjet-printing of PEDOT:PSS and P3HT:PCBM inks with additives. *Organic Electronics 11*, 9 (Sept. 2010), 1516–1522.

[59] Fischer, F., Tremel, K., Saur, A.-K., Link, S., Kayunkid, N., Brinkmann, M., Herrero-Carvajal, D., Lopez Navarrete, J., Ruiz Delgado, M., and Ludwigs, S. Influence of Processing Solvents on Optical Properties and Morphology of a Semicrystalline Low Bandgap Polymer in the Neutral and Charged States. *Macromolecules 46* (2013), 4924–4931.

[60] Forrest, S. R. The path to ubiquitous and low-cost organic electronic appliances on plastic. *Nature 428* (2004), 911–918.

[61] Gärtner, S., Christmann, Marco Sankaran, S., Röhm, H., Prinz, E.-M., Penth, F., Pütz, A., Türeli, A. E., Penth, B., and Baumstümmler, Bernd Colsmann, A. Eco-Friendly Fabrication of 4% Efficient Organic Solar Cells from Surfactant-Free P3HT:ICBA Nanoparticle Dispersions. *Advanced Materials 26*, 38 (2014), 6653–6657.

[62] Germack, D. S., Chan, C. K., Kline, R. J., Fischer, D. a., Gundlach, D. J., Toney, M. F., Richter, L. J., and DeLongchamp, D. M. Interfacial Segregation in Polymer/Fullerene Blend Films for Photovoltaic Devices. *Macromolecules 43*, 8 (Apr. 2010), 3828–3836.

[63] Graham, K. R., Wieruszewski, P. M., Stalder, R., Hartel, M. J., Mei, J., So, F., and Reynolds, J. R. Improved Performance of Molecular Bulk-Heterojunction Photovoltaic Cells through Predictable Selection of Solvent Additives. *Advanced Functional Materials 22*, 22 (July 2012), 4801–4813.

[64] Green, M. A., Emery, K., Hishikawa, Y., Warta, W., and Dunlop, E. D. Solar cell ef fi ciency tables (version 43). *Progress in Photovoltaics: Research and Applications2 22*, version 43 (2014), 1–9.

[65] Grossiord, N., Kroon, J. M., Andriessen, R., and Blom, P. W. Degradation mechanisms in organic photovoltaic devices. *Organic Electronics 13*, 3 (Mar. 2012), 432–456.

[66] Gu, Y., Wang, C., and Russell, T. P. Multi-Length-Scale Morphologies in PCPDTBT/PCBM Bulk-Heterojunction Solar Cells. *Advanced Energy Materials 2*, 6 (June 2012), 683–690.

[67] Guldi, D. M. Fullerenes: three dimensional electron acceptor materials. *Chemical Communications*, 5 (2000), 321–327.

[68] Günes, S., Neugebauer, H., and Sariciftci, N. S. Conjugated polymer-based organic solar cells. *Chemical reviews 107*, 4 (Apr. 2007), 1324–38.

[69] Guo, S., Herzig, E. M., Naumann, A., Tainter, G., Perlich, J., and Mu, P. Influence of Solvent and Solvent Additive on the Morphology of PTB7

films probed via X-ray scattering. *The Journal of Physical Chemistry B 118* (2014), 344–350.

[70] Guo, X., Cui, C., Zhang, M., Huo, L., Huang, Y., Hou, J., and Li, Y. High efficiency polymer solar cells based on poly(3-hexylthiophene)/indene-C70 bisadduct with solvent additive. *Energy & Environmental Science 5*, 7 (2012), 7943.

[71] Guo, X., Zhou, N., Lou, S. J., Smith, J., Tice, D. B., Hennek, J. W., Ortiz, R. P., Navarrete, J. T. L., Li, S., Strzalka, J., Chen, L. X., Chang, R. P. H., Facchetti, A., and Marks, T. J. Polymer solar cells with enhanced fill factors. *Nature Photonics 7*, 10 (Aug. 2013), 825–833.

[72] Halls, J. J. M., Pichler, K., Friend, R. H., Moratti, S. C., and Holmes, a. B. Exciton diffusion and dissociation in a poly(p-phenylenevinylene)/C60 heterojunction photovoltaic cell. *Applied Physics Letters 68*, 22 (1996), 3120.

[73] Hansen, C. *Hansen Solubility Parameters: A User's Handbook, Second Edition*, taylor and ed. CRC Press, Boca Raton FL, 2007.

[74] Hauch, J. a., Schilinsky, P., Choulis, S. a., Childers, R., Biele, M., and Brabec, C. J. Flexible organic P3HT:PCBM bulk-heterojunction modules with more than 1 year outdoor lifetime. *Solar Energy Materials and Solar Cells 92*, 7 (July 2008), 727–731.

[75] He, X., Mukherjee, S., Watkins, S., Chen, M., Qin, T., Thomsen, L., Ade, H., and Mcneill, C. R. Influence of Fluorination and Molecular Weight on the Morphology and Performance of PTB7:PC 71 BM Solar Cells. *The journal of Physical Chemistry C 119* (2014), 9918–9929.

[76] He, Z., Zhong, C., Su, S., Xu, M., Wu, H., and Cao, Y. Enhanced power-conversion efficiency in polymer solar cells using an inverted device structure. *Nature photonics 6* (2012), 591–595.

[77] Heeger, A., Shirakawa, H., and MacDiarmid, A. G. Nobel Prize, http://www.nobelprize.org/nobel_prizes/chemistry/laureates/2000/, Date accessed: 1st of July 2014, 2000.

[78] Hegde, R., Henry, N., Whittle, B., Zang, H., Hu, B., Chen, J., Xiao, K., and Dadmun, M. The impact of controlled solvent exposure on the

morphology, structure and function of bulk heterojunction solar cells. *Solar Energy Materials and Solar Cells 107* (Dec. 2012), 112–124.

[79] Hendriks, K. H., Heintges, G. H. L., Gevaerts, V. S., Wienk, M. M., and Janssen, R. a. J. High-molecular-weight regular alternating diketopyrrolopyrrole-based terpolymers for efficient organic solar cells. *Angewandte Chemie (International ed. in English) 52*, 32 (Aug. 2013), 8341–4.

[80] Hendriks, K. H., Li, W., Heintges, G. H. L., van Pruissen, G. W. P., Wienk, M. M., and Janssen, R. a. J. Homocoupling defects in diketopyrrolopyrrole-based copolymers and their effect on photovoltaic performance. *Journal of the American Chemical Society 136*, 31 (Aug. 2014), 11128–33.

[81] Hendriks, K. H., Li, W., Wienk, M. M., and Janssen, R. a. J. Band Gap Control in Diketopyrrolopyrrole-Based Polymer Solar Cells Using Electron Donating Side Chains. *Advanced Energy Materials 3*, 5 (May 2013), 674–679.

[82] Hill, I. G., Kahn, A., Soos, Z., and Pascal Jr, R. Charge-separation energy in films of p -conjugated organic molecules. *Chemical Physics Letters 327* (2000), 181–188.

[83] Hintz, H., Egelhaaf, H.-J., Luer, L., Hauch, J., Peisert, H., and Chasse, T. Photodegradation of P3HT A Systematic Study of Environmental Factors. *Chemistry of Materials 23*, 2 (Jan. 2011), 145–154.

[84] Hoppe, H., Glatzel, T., Niggemann, M., Schwinger, W., Schaeffler, F., Hinsch, a., Luxsteiner, M., and Sariciftci, N. Efficiency limiting morphological factors of MDMO-PPV:PCBM plastic solar cells. *Thin Solid Films 511-512* (July 2006), 587–592.

[85] Hoppe, H., Niggemann, M., Winder, C., Kraut, J., Hiesgen, R., Hinsch, a., Meissner, D., and Sariciftci, N. S. Nanoscale Morphology of Conjugated Polymer/Fullerene-Based Bulk- Heterojunction Solar Cells. *Advanced Functional Materials 14*, 10 (Oct. 2004), 1005–1011.

[86] Hoppe, H., and Sariciftci, N. S. Morphology of polymer/fullerene bulk heterojunction solar cells. *Journal of Materials Chemistry 16*, 1 (2006), 45.

[87] Hübler, A., Trnovec, B., Zillger, T., Ali, M., Wetzold, N., Mingebach, M., Wagenpfahl, A., Deibel, C., and Dyakonov, V.

Printed Paper Photovoltaic Cells. *Advanced Energy Materials 1*, 6 (Nov. 2011), 1018–1022.

[88] Imahori, H., and Sakata, Y. Fullerenes as Novel Acceptors in Photosynthetic Electron Transfer. *Microreview* (1999), 2445–2457.

[89] Imamura, S., Palanisamy, K., Kannappan, S., and Ochiai, S. Effect of additives on the structure, nanomorphology and efficiency of PCPDTBT: PC71BM solar cells. *Journal of the Korean Physical Society 61*, 3 (Aug. 2012), 464–469.

[90] Islamova, N. I., Kinchin, A. N., Kozlov, A. V., and Kolker, A. M. Solubility of C60 fullerene in o-dichlorobenzene–tetrachloromethane mixtures. *Mendeleev Communications 15*, 2 (Jan. 2005), 86–87.

[91] Jin, H., Olkkonen, J., Tuomikoski, M., Kopola, P., Maaninen, A., and Hast, J. Thickness dependence and solution-degradation effect in poly(3-hexylthiophene):phenyl-C61-butyric acid methyl ester based solar cells. *Solar Energy Materials and Solar Cells 94*, 3 (Mar. 2010), 465–470.

[92] Jo, J., Gendron, D., Najari, A., Moon, J. S., Cho, S., Leclerc, M., and Heeger, A. J. Bulk heterojunction solar cells based on a low-bandgap carbazole-diketopyrrolopyrrole copolymer. *Applied Physics Letters 97*, 20 (2010), 203303.

[93] Kersting, R., Lemmer, U., Deussen, M., Bakker, H., Mahrt, R., Kurz, H., Arkhipov, V., Bässler, H., and Göbel, E. Ultrafast Field-Induced Dissociation of Excitons in Conjugated Polymers. *Physical Review Letters 73*, 10 (1994), 1440–1443.

[94] Keshtov, M. L., Marochkin, D. V., Kochurov, V. S., Khokhlov, a. R., Koukaras, E. N., and Sharma, G. D. New conjugated alternating benzodithiophene-containing copolymers with different acceptor units: synthesis and photovoltaic application. *Journal of Materials Chemistry A 2*, 1 (2014), 155.

[95] Keum, J. K., Xiao, K., Ivanov, I. N., Hong, K., Browning, J. F., Smith, G. S., Shao, M., Littrell, K. C., Rondinone, A. J., Andrew Payzant, E., Chen, J., and Hensley, D. K. Solvent quality-induced nucleation and growth of parallelepiped nanorods in dilute

poly(3-hexylthiophene) (P3HT) solution and the impact on the crystalline morphology of solution-cast thin film. *CrystEngComm 15*, 6 (2013), 1114.

[96] Kim, M., Kim, J.-H., Choi, H. H., Park, J. H., Jo, S. B., Sim, M., Kim, J. S., Jinnai, H., Park, Y. D., and Cho, K. Electrical Performance of Organic Solar Cells with Additive-Assisted Vertical Phase Separation in the Photoactive Layer. *Advanced Energy Materials 4*, 2 (Jan. 2014), n/a–n/a.

[97] Kim, M.-S., Kim, B.-G., and Kim, J. Effective variables to control the fill factor of organic photovoltaic cells. *ACS applied materials & interfaces 1*, 6 (June 2009), 1264–9.

[98] Klauk, H. Organic thin-film transistors. *Chemical Society reviews 39*, 7 (July 2010), 2643–66.

[99] Kline, R., McGehee, M., Kadnikova, E., Liu, J., and Fréchet, J. Controlling the Field-Effect Mobility of Regioregular Polythiophene by Changing the Molecular Weight. *Advanced Materials 15*, 18 (Sept. 2003), 1519–1522.

[100] Koster, L. J. a., Mihailetchi, V. D., and Blom, P. W. M. Ultimate efficiency of polymer/fullerene bulk heterojunction solar cells. *Applied Physics Letters 88*, 9 (2006), 093511.

[101] Kotlarski, J. D., Moet, D. J. D., and Blom, P. W. M. Role of Balanced Charge Carrier Transport in Low Band Gap polymer : fullerene Bulk Heterojunction Solar Cells. *Polymer Physics 49* (2011), 708–711.

[102] Kouijzer, S., Michels, J. J., van den Berg, M., Gevaerts, V. S., Turbiez, M., Wienk, M. M., and Janssen, R. a. J. Predicting morphologies of solution processed polymer:fullerene blends. *Journal of the American Chemical Society 135*, 32 (Aug. 2013), 12057–67.

[103] Krauter, S. C. *Solar Electric Power Generation*. Springer, Berlin, Heidelberg, 2006.

[104] Krebs, F., Carle, J., Cruysbagger, N., Andersen, M., Lilliedal, M., Hammond, M., and Hvidt, S. Lifetimes of organic photovoltaics: photochemistry, atmosphere effects and barrier layers in ITO-MEHPPV:PCBM-aluminium devices. *Solar Energy Materials and Solar Cells 86*, 4 (Apr. 2005), 499–516.

[105] Krebs, F. C. Encapsulation of polymer photovoltaic prototypes. *Solar Energy Materials and Solar Cells 90*, 20 (Dec. 2006), 3633–3643.

[106] Krebs, F. C. Fabrication and processing of polymer solar cells: A review of printing and coating techniques. *Solar Energy Materials and Solar Cells 93*, 4 (Apr. 2009), 394–412.

[107] Krebs, F. C., Fyenbo, J., and Mikkel, J. r. Product integration of compact roll-to-roll processed polymer solar cell modules: methods and manufacture using flexographic printing, slot-die coating and rotary screen printing. *Journal of Materials Chemistry 20*, 41 (2010), 8994.

[108] Krebs, F. C., and Norrman, K. Analysis of the Failure Mechanism for a Stable Organic Photovoltaic During 10 000 h of Testing. *Progree in Photovoltaics: Research and Applications 15* (2007), 697–712.

[109] Kroon, R., Lenes, M., Hummelen, J. C., Blom, P. W. M., and de Boer, B. *Small Bandgap Polymers for Organic Solar Cells (Polymer Material Development in the Last 5 Years)*, vol. 48. Aug. 2008.

[110] Kuik, M., Wetzelaer, G.-J. a. H., Nicolai, H. T., Craciun, N. I., De Leeuw, D. M., and Blom, P. W. M. 25Th Anniversary Article: Charge Transport and Recombination in Polymer Light-Emitting Diodes. *Advanced materials (Deerfield Beach, Fla.) 26*, 4 (Jan. 2014), 512–31.

[111] Kumar, P., and Chand, S. Recent progress and future aspects of organic solar cells. *Progress in Photovoltaics: Research and Applications 20* (2012), 377–415.

[112] Langford, J., and Wilson, A. J. C. Seherrer after Sixty Years: A Survey and Some New Results in the Determination of Crystallite Size. *J. Appl. Cryst 11* (1978), 102–113.

[113] Lee, C.-T., and Lee, C.-H. Conversion efficiency improvement mechanisms of polymer solar cells by balance electron–hole mobility using blended P3HT:PCBM:pentacene active layer. *Organic Electronics 14*, 8 (May 2013), 2046–2050.

[114] Lee, J. K., Ma, W. L., Brabec, C. J., Yuen, J., Moon, J. S., Kim, J. Y., Lee, K., Bazan, G. C., and Heeger, A. J. Processing additives for

improved efficiency from bulk heterojunction solar cells. *Journal of the American Chemical Society 130*, 11 (Mar. 2008), 3619–23.

[115] Li, G., Shrotriya, V., Huang, J., Yao, Y., Moriarty, T., Emery, K., and Yang, Y. High-efficiency solution processable polymer photovoltaic cells by self-organization of polymer blends. *Nature Materials 4*, 11 (Oct. 2005), 864–868.

[116] Li, G., Shrotriya, V., Yao, Y., and Yang, Y. Investigation of annealing effects and film thickness dependence of polymer solar cells based on poly(3-hexylthiophene). *Journal of Applied Physics 98*, 4 (2005), 043704.

[117] Li, G., Yao, Y., Yang, H., Shrotriya, V., Yang, G., and Yang, Y. "Solvent Annealing" Effect in Polymer Solar Cells Based on Poly(3-hexylthiophene) and Methanofullerenes. *Advanced Functional Materials 17*, 10 (July 2007), 1636–1644.

[118] Li, J., Zhao, Y., Tan, H. S., Guo, Y., Di, C.-A., Yu, G., Liu, Y., Lin, M., Lim, S. H., Zhou, Y., Su, H., and Ong, B. S. A stable solution-processed polymer semiconductor with record high-mobility for printed transistors. *Scientific reports 2* (Jan. 2012), 754.

[119] Li, W., Furlan, A., Roelofs, W. S. C., Hendriks, K. H., van Pruissen, G. W. P., Wienk, M. M., and Janssen, R. a. J. Wide band gap diketopyrrolopyrrole-based conjugated polymers incorporating biphenyl units applied in polymer solar cells. *Chemical communications (Cambridge, England) 50*, 6 (Jan. 2014), 679–81.

[120] Li, W., Hendriks, K. H., Furlan, A., Roelofs, W. S. C., Meskers, S. C. J., Wienk, M. M., and Janssen, R. a. J. Effect of the fibrillar microstructure on the efficiency of high molecular weight diketopyrrolopyrrole-based polymer solar cells. *Advanced materials (Deerfield Beach, Fla.) 26*, 10 (Mar. 2014), 1565–70.

[121] Li, Y., Sonar, P., Murphy, L., and Hong, W. High mobility diketopyrrolopyrrole (DPP)-based organic semiconductor materials for organic thin film transistors and photovoltaics. *Energy & Environmental Science 6*, 6 (2013), 1684.

[122] Li, Y., Sonar, P., Singh, S. P., Ooi, Z. E., Lek, E. S. H., and Loh, M. Q. Y. Poly(2,5-bis(2-octyldodecyl)-3,6-di(furan-2-yl)-2,5-dihydro-pyrrolo[3,4-c]pyrrole-1,4-dione-co-thieno[3,2-b]thiophene): a high performance polymer semiconductor for both organic thin film transistors and organic photovoltaics. *Physical chemistry chemical physics : PCCP* (Apr. 2012).

[123] Li, Y., Sonar, P., Singh, S. P., Soh, M. S., Meurs, M. V., and Tan, J. Annealing-Free High-Mobility Diketopyrrolopyrrole-Quaterthiophene Copolymer for Solution-Processed Organic Thin Film Transistors. *journal of the americal chemical society 133* (2011), 2198–2204.

[124] Liang, Y., Xu, Z., Xia, J., Tsai, S.-T., Wu, Y., Li, G., Ray, C., and Yu, L. For the bright future - bulk heterojunction polymer solar cells with power conversion efficiency of 7.4%. *Advanced materials 22*, 20 (May 2010), E135–138.

[125] Liao, H.-c., Ho, C.-c., Chang, C.-y., Jao, M.-h., Darling, S. B., and Su, W.-f. Additives for morphology control in high-efficiency organic solar cells. *Materials today 16*, 9 (2013), 326–336.

[126] Lindqvist, C., Bergqvist, J., Feng, C.-C., Gustafsson, S., Bäcke, O., Treat, N. D., Bounioux, C., Henriksson, P., Kroon, R., Wang, E., Sanz-Velasco, A., Kristiansen, P. M., Stingelin, N., Olsson, E., Inganäs, O., Andersson, M. R., and Müller, C. Fullerene Nucleating Agents: A Route Towards Thermally Stable Photovoltaic Blends. *Advanced Energy Materials 4*, 9 (June 2014), n/a–n/a.

[127] Liu, F., Wang, C., Baral, J. K., Zhang, L., Watkins, J. J., Briseno, A. L., and Russell, T. P. Relating Chemical Structure to Device Performance via Morphology Control in Diketopyrrolopyrrole-Based Low Band Gap Polymers. *Journal of the American Chemical Society 135*, 51 (Dec. 2013), 19248–59.

[128] Liu, J., and Han, Y. The influence of additive property on performance of organic bulk heterojunction solar cells. *Polymer Bulletin 68*, 8 (Mar. 2012), 2145–2174.

[129] Liu, J., Shao, S., Fang, G., Meng, B., Xie, Z., and Wang, L. High-efficiency inverted polymer solar cells with transparent and work-function tunable MoO(3)-Al composite film as cathode buffer layer. *Advanced materials (Deerfield Beach, Fla.) 24*, 20 (May 2012), 2774–9.

[130] Liu, X., Huettner, S., Rong, Z., Sommer, M., and Friend, R. H. Solvent Additive Control of Morphology and Crystallization in Semiconducting Polymer Blends. *Advanced Materials 24*, 5 (Nov. 2012), 669–674.

[131] Liu, Z., Ju, H., and Lee, E.-C. Improvement of polycarbazole-based organic bulk-heterojunction solar cells using 1,8-diiodooctane. *Applied Physics Letters 103*, 13 (2013), 133308.

[132] Lloyd, M. T., Olson, D. C., Lu, P., Fang, E., Moore, D. L., White, M. S., Reese, M. O., Ginley, D. S., and Hsu, J. W. P. Impact of contact evolution on the shelf life of organic solar cells. *Journal of Materials Chemistry 19*, 41 (2009), 7638.

[133] Loi, M. a., Toffanin, S., Muccini, M., Forster, M., Scherf, U., and Scharber, M. Charge Transfer Excitons in Bulk Heterojunctions of a Polyfluorene Copolymer and a Fullerene Derivative. *Advanced Functional Materials 17*, 13 (Sept. 2007), 2111–2116.

[134] Ma, W., Yang, C., Gong, X., Lee, K., and Heeger, A. J. Thermally Stable, Efficient Polymer Solar Cells with Nanoscale Control of the Interpenetrating Network Morphology. *Advanced Functional Materials 15*, 10 (Oct. 2005), 1617–1622.

[135] Machui, F., Abbott, S., Waller, D., Koppe, M., and Brabec, C. J. Determination of Solubility Parameters for Organic Semiconductor Formulations. *Macromolecular Chemistry and Physics 212*, 19 (Oct. 2011), 2159–2165.

[136] Machui, F., Langner, S., Zhu, X., Abbott, S., and Brabec, C. J. Determination of the P3HT:PCBM solubility parameters via a binary solvent gradient method: Impact of solubility on the photovoltaic performance. *Solar Energy Materials and Solar Cells 100* (May 2012), 138–146.

[137] Malliaras, G., Salem, J., Brock, P., and Scott, C. Electrical characteristics and efficiency of single-layer organic light-emitting diodes. *Physical Review B 58*, 20 (Nov. 1998), R13411–R13414.

[138] Manceau, M., Chambon, S., Rivaton, A., Gardette, J.-L., Guillerez, S., and Lemaître, N. Effects of long-term UV–visible light irradiation in the absence of oxygen on P3HT and P3HT:PCBM blend. *Solar Energy Materials and Solar Cells 94*, 10 (Oct. 2010), 1572–1577.

[139] Manceau, M., Rivaton, A., and Gardette, J.-L. Involvement of Singlet Oxygen in the Solid-State Photochemistry of P3HT. *Macromolecular Rapid Communications 29*, 22 (Nov. 2008), 1823–1827.

[140] Manceau, M., Rivaton, A., Gardette, J.-L., Guillerez, S., and Lemaître, N. The mechanism of photo- and thermooxidation of poly(3-hexylthiophene) (P3HT) reconsidered. *Polymer Degradation and Stability 94*, 6 (June 2009), 898–907.

[141] Markov, D., Hummelen, J., Blom, P., and Sieval, A. Dynamics of exciton diffusion in poly(p-phenylene vinylene)/fullerene heterostructures. *Physical Review B 72*, 4 (July 2005), 045217.

[142] Martens, H. C. F. Comparative study of hole transport in poly(p-phenylene vinylene)derivatives. *Physical review B 61*, 11 (2000), 7489–7493.

[143] Melzer, B. C., Koop, E. J., Mihailetchi, V. D., and Blom, P. W. M. Hole Transport in Poly (phenylene vinylene)/ Methanofullerene Bulk-Heterojunction Solar Cells. 865–870.

[144] Mens, R., Demir, F., Van Assche, G., Van Mele, B., Vanderzande, D., and Adriaensens, P. Influence of the processing solvent on the photoactive layer nanomorphology of P3HT/PC60BM solar cells. *Journal of Polymer Science Part A: Polymer Chemistry 50*, 5 (Mar. 2012), 1037–1041.

[145] Mihailetchi, V., van Duren, J., Blom, P., Hummelen, J., Janssen, R., Kroon, J., Rispens, M., Verhees, W., and Wienk, M. Electron Transport in a Methanofullerene. *Advanced Functional Materials 13*, 1 (Jan. 2003), 43–46.

[146] Moon, J. S., Jo, J., and Heeger, A. J. Nanomorphology of PCDTBT:PC70BM Bulk Heterojunction Solar Cells. *Advanced Energy Materials 2*, 3 (Mar. 2012), 304–308.

[147] Moon, J. S., Takacs, C. J., Cho, S., Coffin, R. C., Kim, H., Bazan, G. C., and Heeger, A. J. Effect of processing additive on the nanomorphology of a bulk heterojunction material. *Nano letters 10*, 10 (Oct. 2010), 4005–8.

[148] Motaung, D. E., Malgas, G. F., Nkosi, S. S., Mhlongo, G. H., Mwakikunga, B. W., Malwela, T., Arendse, C. J., Muller, T. F. G., and Cummings, F. R. Comparative study: the effect of annealing conditions

on the properties of P3HT:PCBM blends. *Journal of Materials Science 48*, 4 (Oct. 2012), 1763–1778.

[149] Moule, A. J., and Meerholz, K. Controlling Morphology in Polymer–Fullerene Mixtures. *Advanced Materials 20*, 2 (Jan. 2008), 240–245.

[150] Mulligan, C. J., Wilson, M., Bryant, G., Vaughan, B., Zhou, X., Belcher, W. J., and Dastoor, P. C. A projection of commercial-scale organic photovoltaic module costs. *Solar Energy Materials and Solar Cells 120* (Jan. 2014), 9–17.

[151] Murphy, L., Hong, W., Aziz, H., and Li, Y. Organic photovoltaics with thick active layers (- 800nm) using a high mobility polymer donor. *Solar Energy Materials and Solar Cells 114* (July 2013), 71–81.

[152] Murphy, L. D. *Master thesis: Influence of High Mobility Polymer Semiconductors in Organic Photovoltaics*. University of Waterloo, 2013.

[153] Mutolo, K. L., Mayo, E. I., Rand, B. P., Forrest, S. R., and Thompson, M. E. Enhanced open-circuit voltage in subphthalocyanine/C60 organic photovoltaic cells. *Journal of the American Chemical Society 128*, 25 (June 2006), 8108–9.

[154] Myers, J. D., and Xue, J. Organic Semiconductors and their Applications in Photovoltaic Devices. *Polymer Reviews 52*, 1 (Jan. 2012), 1–37.

[155] Neugebauer, H., Brabec, C., Hummelen, J., and Sariciftci, N. Stability and photodegradation mechanisms of conjugated polymer/fullerene plastic solar cells. *Solar Energy Materials and Solar Cells 61*, 1 (Feb. 2000), 35–42.

[156] Nguyen, T. L., Choi, H., Ko, S.-J., Uddin, M. a., Walker, B., Yum, S., Jeong, J.-E., Yun, M. H., Shin, T. J., Hwang, S., Kim, J. Y., and Woo, H. Y. Semi-crystalline photovoltaic polymers with efficiency exceeding 9% in a 300 nm thick conventional single-cell device. *Energy & Environmental Science* (July 2014), 3040–3051.

[157] Nilsson, S., Bernasik, A., Budkowski, A., and Moons, E. Morphology and Phase Segregation of Spin-Casted Films of Polyfluorene / PCBM Blends. *Macromolecules 40* (2007), 8291–8301.

[158] Oklobia, O., and Shafai, T. Correlation between charge carriers mobility and nanomorphology in a blend of P3HT/PCBM bulk heterojunction solar cell: Impact on recombination mechanisms. *Solar Energy Materials and Solar Cells 122* (Mar. 2014), 158–163.

[159] Ouyang, J., and Xia, Y. High-performance polymer photovoltaic cells with thick P3HT:PCBM films prepared by a quick drying process. *Solar Energy Materials and Solar Cells 93*, 9 (Sept. 2009), 1592–1597.

[160] Padinger, F., Rittberger, R., and Sariciftci, N. Effects of Postproduction Treatment on Plastic Solar Cells. *Advanced Functional Materials 13*, 1 (Jan. 2003), 85–88.

[161] Park, C.-D., Fleetham, T. a., Li, J., and Vogt, B. D. High performance bulk-heterojunction organic solar cells fabricated with non-halogenated solvent processing. *Organic Electronics 12*, 9 (Sept. 2011), 1465–1470.

[162] Park, H., Lee, K. Y., Kim, W., Shin, H.-W., Wang, D. H., Ahn, T. K., and Park, J. H. Discrepancy of optimum ratio in bulk heterojunction photovoltaic devices: initial cell efficiency vs long-term stability. *ACS applied materials & interfaces 5*, 5 (Mar. 2013), 1612–8.

[163] Park, H. J., Kim, H., Lee, J. Y., Lee, T., and Guo, L. J. Optimization of polymer photovoltaic cells with bulk heterojunction layers hundreds of nanometers thick: modifying the morphology and cathode interface. *Energy & Environmental Science 6*, 7 (2013), 2203.

[164] Park, J. H., Kim, J. S., Lee, J. H., Lee, W. H., and Cho, K. Effect of Annealing Solvent Solubility on the Performance of Poly(3-hexylthiophene)/Methanofullerene Solar Cells. *The Journal of Physical Chemistry C 113*, 40 (Oct. 2009), 17579–17584.

[165] Park, J. H., Park, J.-I., Kim, D. H., Kim, J.-H., Kim, J. S., Lee, J. H., Sim, M., Lee, S. Y., and Cho, K. Enhanced device performance of organic solar cells via reduction of the crystallinity in the donor polymer. *Journal of Materials Chemistry 20*, 28 (2010), 5860.

[166] Park, S. H., Roy, A., Beaupre, S., Shinuk, C., Coates, N., Moon, J. S., Moses, D., Leclerc, M., Lee, K., and Heeger, A. J. Bulk heterojunction solar cells with internal quantum efficiency approaching 100 %. *Nature photonics 3*, April (2009).

[167] Parnell, A. J., Dunbar, A. D. F., Pearson, A. J., Staniec, P. a., Dennison, A. J. C., Hamamatsu, H., Skoda, M. W. a., Lidzey, D. G., and Jones, R. a. L. Depletion of PCBM at the cathode interface in P3HT/PCBM thin films as quantified via neutron reflectivity measurements. *Advanced materials (Deerfield Beach, Fla.) 22*, 22 (June 2010), 2444–7.

[168] Pavlopoulou, E., Fleury, G., Deribew, D., Cousin, F., Geoghegan, M., and Hadziioannou, G. Phase separation-driven stratification in conventional and inverted P3HT:PCBM organic solar cells. *Organic Electronics 14*, 5 (May 2013), 1249–1254.

[169] Peet, J., Kim, J. Y., Coates, N. E., Ma, W. L., Moses, D., Heeger, a. J., and Bazan, G. C. Efficiency enhancement in low-bandgap polymer solar cells by processing with alkane dithiols. *Nature materials 6*, 7 (July 2007), 497–500.

[170] Peet, J., Soci, C., Coffin, R. C., Nguyen, T. Q., Mikhailovsky, A., Moses, D., and Bazan, G. C. Method for increasing the photoconductive response in conjugated polymer/fullerene composites. *Applied Physics Letters 89*, 25 (2006), 252105.

[171] Perez, L. a., Chou, K. W., Love, J. a., van der Poll, T. S., Smilgies, D.-M., Nguyen, T.-Q., Kramer, E. J., Amassian, A., and Bazan, G. C. Solvent additive effects on small molecule crystallization in bulk heterojunction solar cells probed during spin casting. *Advanced materials (Deerfield Beach, Fla.) 25*, 44 (Nov. 2013), 6380–4.

[172] Perez, M. D., Borek, C., Forrest, S. R., and Thompson, M. E. Molecular and Morphological Influences on the Open Circuit. *Journal of the American Chemical Society 131* (2009), 9281–9286.

[173] Pfuetzner, S., Meiss, J., Petrich, A., Riede, M., and Leo, K. Improved bulk heterojunction organic solar cells employing C[sub 70] fullerenes. *Applied Physics Letters 94*, 22 (2009), 223307.

[174] Pho, T. V., Toma, F. M., Tremolet de Villers, B. J., Wang, S., Treat, N. D., Eisenmenger, N. D., Su, G. M., Coffin, R. C., Douglas, J. D., Fréchet, J. M. J., Bazan, G. C., Wudl, F., and Chabinyc, M. L. Decacyclene Triimides: Paving the Road to Universal Non-Fullerene Acceptors for Organic Photovoltaics. *Advanced Energy Materials 4*, 5 (Apr. 2014), 1–7.

[175] Piersimoni, F., Chambon, S., Vandewal, K., Mens, R., Boonen, T., Gadisa, A., Izquierdo, M., Filippone, S., Ruttens, B., D'Haen, J., Martin, N., Lutsen, L., Vanderzande, D., Adriaensens, P., and Manca, J. V. Influence of Fullerene Ordering on the Energy of the Charge-Transfer State and Open-Circuit Voltage in Polymer Fullerene Solar Cells, June 2011.

[176] Qi, B., and Wang, J. Fill factor in organic solar cells. *Physical chemistry chemical physics : PCCP 15*, 23 (June 2013), 8972–82.

[177] Ren, G., Ahmed, E., and Jenekhe, S. a. Non-Fullerene Acceptor-Based Bulk Heterojunction Polymer Solar Cells: Engineering the Nanomorphology via Processing Additives. *Advanced Energy Materials 1*, 5 (Oct. 2011), 946–953.

[178] Richards, J. J., Rice, A. H., Nelson, R. D., Kim, F. S., Jenekhe, S. a., Luscombe, C. K., and Pozzo, D. C. Modification of PCBM Crystallization via Incorporation of C 60 in Polymer/Fullerene Solar Cells. *Advanced Functional Materials 23*, 4 (Jan. 2013), 514–522.

[179] Rispens, M. T., Meetsma, A., Rittberger, R., Brabec, C. J., Sariciftci, N. S., and Hummelen, J. C. Influence of the solvent on the crystal structure of PCBM and the efficiency of MDMO-PPV:PCBM 'plastic' solar cells. *Chemical communications (Cambridge, England)*, 17 (Sept. 2003), 2116–8.

[180] Rivaton, A., Chambon, S., Manceau, M., Gardette, J.-L., Lemaître, N., and Guillerez, S. Light-induced degradation of the active layer of polymer-based solar cells. *Polymer Degradation and Stability 95*, 3 (Mar. 2010), 278–284.

[181] Ruderer, M. a., Guo, S., Meier, R., Chiang, H.-Y., Körstgens, V., Wiedersich, J., Perlich, J., Roth, S. V., and Müller-Buschbaum, P. Solvent-Induced Morphology in Polymer-Based Systems for Organic Photovoltaics. *Advanced Functional Materials 21*, 17 (Sept. 2011), 3382–3391.

[182] Salim, T., Wong, L. H., Bräuer, B., Kukreja, R., Foo, Y. L., Bao, Z., and Lam, Y. M. Solvent additives and their effects on blend morphologies of bulk heterojunctions. *Journal of Materials Chemistry 21*, 1 (2011), 242.

[183] Sariciftci, N. S., Smilowitz, L., Heeger, a. J., and Wudl, F. Photoinduced electron transfer from a conducting polymer to buckminsterfullerene. *Science (New York, N.Y.) 258*, 5087 (Nov. 1992), 1474–6.

[184] Sarkas, H. W., Kwan, W., Flom, S. R., Merritt, C. D., and Kafafi, Z. H. Enhanced Photooxidative Stability of Conjugated Polymers via C 60 Doping. *J. Phys. Chem C 100* (1996), 5169–5171.

[185] Scharber, M. C., Mühlbacher, D., Koppe, M., Denk, P., Waldauf, C., Heeger, A. J., and Brabec, C. J. Design Rules for Donors in Bulk-Heterojunction Solar Cells—Towards 10 % Energy-Conversion Efficiency. *Advanced Materials 18*, 6 (Mar. 2006), 789–794.

[186] Scharsich, C., Lohwasser, R. H., Sommer, M., Asawapirom, U., Scherf, U., Thelakkat, M., Neher, D., and Köhler, A. Control of aggregate formation in poly(3-hexylthiophene) by solvent, molecular weight, and synthetic method. *Journal of Polymer Science Part B: Polymer Physics 50*, 6 (Mar. 2012), 442–453.

[187] Schmidt-Hansberg, B., Sanyal, M., Klein, M. F. G., Pfaff, M., Schnabel, N., Jaiser, S., Vorobiev, A., Müller, E., Colsmann, A., Scharfer, P., Gerthsen, D., Lemmer, U., Barrena, E., and Schabel, W. Moving through the phase diagram: morphology formation in solution cast polymer-fullerene blend films for organic solar cells. *ACS nano 5*, 11 (Nov. 2011), 8579–90.

[188] Seemann, A., Egelhaaf, H.-J., Brabec, C. J., and Hauch, J. a. Influence of oxygen on semi-transparent organic solar cells with gas permeable electrodes. *Organic Electronics 10*, 8 (Dec. 2009), 1424–1428.

[189] Semenov, K. N., Charykov, N. a., Keskinov, V. a., Piartman, A. K., Blokhin, A. a., and Kopyrin, A. a. Solubility of Light Fullerenes in Organic Solvents. *Journal of Chemical & Engineering Data 55*, 1 (Jan. 2010), 13–36.

[190] Servaites, J. D., Ratner, M. a., and Marks, T. J. Organic solar cells: A new look at traditional models. *Energy & Environmental Science 4*, 11 (2011), 4410.

[191] Shaheen, S. E., Brabec, C. J., Sariciftci, N. S., Padinger, F., Fromherz, T., and Hummelen, J. C. 2.5% Efficient Organic Plastic Solar Cells. *Applied Physics Letters 78*, 6 (2001), 841.

[192] Shin, P.-k., Kumar, P., Kumar, A., Kannappan, S., and Ochiai, S. Effects of Organic Solvents for Composite Active Layer of PCDTBT / PC 71 BM on Characteristics of Organic Solar Cell Devices. *International journal of photoenergy 2014* (2013), 1–8.

[193] Shoaee, S., Subramaniyan, S., Xin, H., Keiderling, C., Tuladhar, P. S., Jamieson, F., Jenekhe, S. a., and Durrant, J. R. Charge Photogeneration for a Series of Thiazolo-Thiazole Donor Polymers Blended with the Fullerene Electron Acceptors PCBM and ICBA. *Advanced Functional Materials 23*, 26 (July 2013), 3286–3298.

[194] Sø ndergaard, R. R., Hösel, M., and Krebs, F. C. Roll-to-Roll fabrication of large area functional organic materials. *Journal of Polymer Science Part B: Polymer Physics 51*, 1 (Jan. 2013), 16–34.

[195] Son, S. K., Lee, H.-S., Ha, J. S., Kim, K. H., Son, H. J., Ko, M. J., Kim, H., Lee, D.-K., Kim, J. Y., Lee, W., Park, S., Choi, D. H., and Kim, B. Effect of asymmetric solubility of diketopyrrolopyrrole-based polymers and PC71BMs in a binary solvent system on the performance of bulk heterojunction solar cells. *Solar Energy Materials and Solar Cells 124* (May 2014), 232–240.

[196] Spanggaard, H., and Krebs, F. C. A brief history of the development of organic and polymeric photovoltaics. *Solar Energy Materials and Solar Cells 83*, 2-3 (June 2004), 125–146.

[197] Stallinga, P. *Electrical Characterization of Organic Electronic Materials and Devices*, wiley ed. 2009.

[198] Street, R. a., Davies, D., Khlyabich, P. P., Burkhart, B., and Thompson, B. C. Origin of the tunable open-circuit voltage in ternary blend bulk heterojunction organic solar cells. *Journal of the American Chemical Society 135*, 3 (Jan. 2013), 986–9.

[199] Stubinger, T., and Brutting, W. Exciton diffusion and optical interference in organic donor–acceptor photovoltaic cells. *Journal of Applied Physics 90*, 7 (2001), 3632.

[200] Sun, B., Hong, W., Yan, Z., Aziz, H., and Li, Y. Record high electron mobility of 6.3 cm2 V-1 s-1 achieved for polymer semiconductors using a new building block. *Advanced materials (Deerfield Beach, Fla.) 26*, 17 (May 2014), 2636–42, 2613.

[201] Sun, Y., Takacs, C. J., Cowan, S. R., Seo, J. H., Gong, X., Roy, A., and Heeger, A. J. Efficient, air-stable bulk heterojunction polymer solar cells using MoO(x) as the anode interfacial layer. *Advanced materials (Deerfield Beach, Fla.) 23*, 19 (May 2011), 2226–30.

[202] Takashima, M., Shichiri, M., Hagihara, Y., Yoshida, Y., and Niki, E. Reactivity toward oxygen radicals and antioxidant action of thiol compounds. *BioFactors (Oxford, England) 38*, 3 (2012), 240–8.

[203] Tanase, C., Meijer, E. J., Blom, P. W. M., and de Leeuw, D. M. Unification of the Hole Transport in Polymeric Field-Effect Transistors and Light-Emitting Diodes. *Physical Review Letters 91*, 21 (Nov. 2003), 216601.

[204] Tang, C. W. Two-layer organic photovoltaic cell. *Applied Physics Letters 48*, 2 (1986), 183.

[205] Treat, N. D., Varotto, A., Takacs, C. J., Batara, N., Al-Hashimi, M., Heeney, M. J., Heeger, A. J., Wudl, F., Hawker, C. J., and Chabinyc, M. L. Polymer-fullerene miscibility: a metric for screening new materials for high-performance organic solar cells. *Journal of the American Chemical Society 134*, 38 (Sept. 2012), 15869–79.

[206] Troshin, P. a., Hoppe, H., Renz, J., Egginger, M., Mayorova, J. Y., Goryachev, A. E., Peregudov, A. S., Lyubovskaya, R. N., Gobsch, G., Sariciftci, N. S., and Razumov, V. F. Material Solubility-Photovoltaic Performance Relationship in the Design of Novel Fullerene Derivatives for Bulk Heterojunction Solar Cells. *Advanced Functional Materials 19*, 5 (Mar. 2009), 779–788.

[207] Uhrich, C., Wynands, D., Olthof, S., Riede, M. K., Leo, K., Sonntag, S., Maennig, B., and Pfeiffer, M. Origin of open circuit voltage in planar and bulk heterojunction organic thin-film photovoltaics depending on doped transport layers. *Journal of Applied Physics 104*, 4 (2008), 043107.

[208] Van-Bavel, S. S., Sourty, E., de With, G., and Loos, J. Three-dimensional nanoscale organization of bulk heterojunction polymer solar cells. *Nano letters 9*, 2 (Mar. 2009), 507–13.

[209] Vandewal, K., Tvingstedt, K., Gadisa, A., Inganäs, O., and Manca, J. V. On the origin of the open-circuit voltage of polymer-fullerene solar cells. *Nature materials 8*, 11 (Nov. 2009), 904–9.

[210] Veldman, D., Meskers, S. C. J., and Janssen, R. a. J. The Energy of Charge-Transfer States in Electron Donor-Acceptor Blends: Insight into the Energy Losses in Organic Solar Cells. *Advanced Functional Materials 19*, 12 (June 2009), 1939–1948.

[211] Verploegen, E., Miller, C. E., Schmidt, K., Bao, Z., and Toney, M. F. Manipulating the Morphology of P3HT–PCBM Bulk Heterojunction Blends with Solvent Vapor Annealing. *Chemistry of Materials* (Oct. 2012), 121003154924005.

[212] Voroshazi, E., Verreet, B., Aernouts, T., and Heremans, P. Long-term operational lifetime and degradation analysis of P3HT:PCBM photovoltaic cells. *Solar Energy Materials and Solar Cells 95*, 5 (May 2011), 1303–1307.

[213] Wakim, S., Beaupré, S., Blouin, N., Aich, B.-R., Rodman, S., Gaudiana, R., Tao, Y., and Leclerc, M. Highly efficient organic solar cells based on a poly(2,7-carbazole) derivative. *Journal of Materials Chemistry 19*, 30 (2009), 5351.

[214] Walker, B., Tamayo, A., Duong, D. T., Dang, X.-D., Kim, C., Granstrom, J., and Nguyen, T.-Q. A Systematic Approach to Solvent Selection Based on Cohesive Energy Densities in a Molecular Bulk Heterojunction System. *Advanced Energy Materials 1*, 2 (Mar. 2011), 221–229.

[215] Wang, D. H., Park, K. H., Seo, J. H., Seifter, J., Jeon, J. H., Kim, J. K., Park, J. H., Park, O. O., and Heeger, A. J. Enhanced Power Conversion Efficiency in PCDTBT/PC70BM Bulk Heterojunction Photovoltaic Devices with Embedded Silver Nanoparticle Clusters. *Advanced Energy Materials 1*, 5 (Oct. 2011), 766–770.

[216] Wang, G., Jiu, T., Li, P., Li, J., Sun, C., Lu, F., and Fang, J. Preparation and characterization of MoO3 hole-injection layer for organic solar

cell fabrication and optimization. *Solar Energy Materials and Solar Cells 120* (Jan. 2014), 603–609.

[217] Wang, H., Liu, F., Bu, L., Gao, J., Wang, C., Wei, W., and Russell, T. P. The role of additive in diketopyrrolopyrrole-based small molecular bulk heterojunction solar cells. *Advanced materials (Deerfield Beach, Fla.) 25*, 45 (Dec. 2013), 6519–25.

[218] Wang, J., Ren, X., Shi, S., Leung, C., and Chan, P. K. Charge accumulation induced S-shape J–V curves in bilayer heterojunction organic solar cells. *Organic Electronics 12*, 6 (June 2011), 880–885.

[219] Wang, M., Xie, F., Du, J., Tang, Q., Zheng, S., Miao, Q., Chen, J., Zhao, N., and Xu, J. Degradation mechanism of organic solar cells with aluminum cathode. *Solar Energy Materials and Solar Cells 95*, 12 (Dec. 2011), 3303–3310.

[220] Wang, Q., Williams, G., Tsui, T., and Aziz, H. Photochemical deterioration of the organic/metal contacts in organic optoelectronic devices. *Journal of Applied Physics 112*, 6 (2012), 064502.

[221] Wang, T., Pearson, A. J., Dunbar, A. D. F., Staniec, P. a., Watters, D. C., Yi, H., Ryan, A. J., Jones, R. a. L., Iraqi, A., and Lidzey, D. G. Correlating Structure with Function in Thermally Annealed PCDTBT:PC70BM Photovoltaic Blends. *Advanced Functional Materials 22*, 7 (Apr. 2012), 1399–1408.

[222] Wantz, G., Derue, L., Dautel, O., Rivaton, A., Hudhomme, P., and Dagron-Lartigau, C. Stabilizing polymer-based bulk heterojunction solar cells via crosslinking. *Polymer International 63*, 8 (Aug. 2014), 1346–1361.

[223] Westacott, P., Tumbleston, J. R., Shoaee, S., Fearn, S., Bannock, J. H., Gilchrist, J. B., Heutz, S., DeMello, J., Heeney, M., Ade, H., Durrant, J., McPhail, D. S., and Stingelin, N. On the role of intermixed phases in organic photovoltaic blends. *Energy & Environmental Science 6*, 9 (2013), 2756.

[224] Widmer, J., Tietze, M., Leo, K., and Riede, M. Open-Circuit Voltage and Effective Gap of Organic Solar Cells. *Advanced Functional Materials 23*, 46 (Dec. 2013), 5814–5821.

[225] Williams, G., Wang, Q., and Aziz, H. The Photo-Stability of Polymer Solar Cells: Contact Photo-Degradation and the Benefits of Interfacial Layers. *Advanced Functional Materials 23*, 18 (May 2013), 2239–2247.

[226] Wong, W. S., and Salleo, A. *Flexible Electronics : Materials and Applications Electronic Materials : Science and Technology*. Springer, New York, 2009.

[227] Wu, L., Zang, H., Hsiao, Y.-C., Zhang, X., and Hu, B. Origin of the fill factor loss in bulk-heterojunction organic solar cells. *Applied Physics Letters 104*, 15 (Apr. 2014), 153903.

[228] Xin, H., Kim, F. S., and Jenekhe, S. A. Highly Efficient Solar Cells Based on Poly (3-butylthiophene) Nanowires. *journal of the americal chemical society 130* (2008), 5424–5425.

[229] Xin, H., Ren, G., Kim, F. S., and Jenekhe, S. a. Bulk Heterojunction Solar Cells from Poly(3-butylthiophene)/Fullerene Blends: In Situ Self-Assembly of Nanowires, Morphology, Charge Transport, and Photovoltaic Properties. *Chemistry of Materials 20*, 19 (Oct. 2008), 6199–6207.

[230] Xu, X., Zhang, F., Zhang, J., Wang, H., Zhuo, Z., Liu, Y., Wang, J., Wang, Z., and Xu, Z. High efficient inverted polymer solar cells with different annealing treatment. *Materials Science and Engineering C 32*, 4 (May 2012), 685–691.

[231] Xue, B., Vaughan, B., Poh, C.-H., Burke, K. B., Thomsen, L., Stapleton, A., Zhou, X., Bryant, G. W., Belcher, W., and Dastoor, P. C. Vertical Stratification and Interfacial Structure in P3HT:PCBM Organic Solar Cells. *The Journal of Physical Chemistry C 114*, 37 (Sept. 2010), 15797–15805.

[232] Yamanari, T., Taima, T., Sakai, J., and Saito, K. Origin of the open-circuit voltage of organic thin-film solar cells based on conjugated polymers. *Solar Energy Materials and Solar Cells 93*, 6-7 (June 2009), 759–761.

[233] Yang, X., van Duren, J. K. J., Rispens, M. T., Hummelen, J. C., Janssen, R. A. J., Michels, M. A. J., and Loos, J. Crystalline Organization of a Methanofullerene as Used for Plastic Solar Cell Applications. *Advanced Materials 16*, 910 (May 2004), 802–806.

[234] Yao, Y., Hou, J., Xu, Z., Li, G., and Yang, Y. Effects of Solvent Mixtures on the Nanoscale Phase Separation in Polymer Solar Cells. *Advanced Functional Materials 18*, 12 (June 2008), 1783–1789.

[235] Yu, G., Gao, J., Hummelen, J. C., Wudl, F., and Heeger, a. J. Polymer Photovoltaic Cells: Enhanced Efficiencies via a Network of Internal Donor-Acceptor Heterojunctions. *Science 270*, 5243 (Dec. 1995), 1789–1791.

[236] Zhang, L., Xing, X., Zheng, L., Chen, Z., Xiao, L., Qu, B., and Gong, Q. Vertical phase separation in bulk heterojunction solar cells formed by in situ polymerization of fulleride. *Scientific reports 4* (Jan. 2014), 5071.

[237] Zhokhavets, U., Erb, T., Gobsch, G., Al-Ibrahim, M., and Ambacher, O. Relation between absorption and crystallinity of poly(3-hexylthiophene)/fullerene films for plastic solar cells. *Chemical Physics Letters 418*, 4-6 (Feb. 2006), 347–350.

[238] Zhokhavets, U., Erb, T., Hoppe, H., Gobsch, G., and Serdar Sariciftci, N. Effect of annealing of poly(3-hexylthiophene)/fullerene bulk heterojunction composites on structural and optical properties. *Thin Solid Films 496*, 2 (Feb. 2006), 679–682.